Measuring the electron electric dipole moment using supersonic YbF

Paul Constantine Condylis

Thesis submitted in partial fulfilment of the requirements for the degree of Doctor of Philosophy of the University of London and the Diploma of Membership of Imperial College.

Imperial College London

University of London

February 2006

Abstract

Measuring the electron electric dipole moment using supersonic YbF

Paul Constantine Condylis

In this thesis I describe the design and construction of a molecular interferometer which measure extremely small shifts to the energy of YbF molecules. This interferometer has been significantly improved with a new supersonic source of YbF. I also describe the measurement of the electron electric dipole moment using the interferometer with unprecedented statistical sensitivity compared to previous experiments using molecules. Furthermore the results indicate that this experiment could soon make the most sensitive measurement in the region of 3×10^{-28} e.cm.

Acknowledgments

Without the help of many people this thesis would not be. Here I would like to thank those people.

Ed Hinds was my supervisor and principle investigator for this work. His patience and help, both in and out of the lab, are very much appreciated. I would also like to thank him for painstakingly examining every page of this thesis.

Jony Hudson has worked on this experiment over many years both as a PhD student and a post-doctoral researcher. His expertise in the lab, at the computer, and at the white board have made me a better physicist both through helping me with "all things experimental" and by expanding my knowledge through many discussions. I am also indebted to Jony for teaching me the phrase "*Righty tighty, lefty loosy.*" and for reminding me, on many occasions, of the right-hand rule of electromagnetism which I have subsequently not forgotten. I would also like to thank Jony for his patience in answering my many stupid questions and all his help towards this thesis which would be of a lesser quality without his eye for precision and many comments.

Ben Sauer has also worked on this experiment for many years. He has also greatly contributed to this thesis and the experiment. I thank him for his help in answering questions, and clarifying many physics problems. He is also very skilled at electronics which have made the experiment work, and plumbing which have, by use of occasional and slight flooding, stopped the lab from becoming a swimming pool.

Mike Tarbutt, and Henry Ashworth have also worked on the experiment, making it run and take data for long periods. I would like to thank them for their help both with the experiment and through many discussions.

These people mentioned above are the principle members of the CCM group at Imperial College who have worked on this experiment. However, there are many other people, in the CCM group and in the old SCOAP group in Brighton, who I wish to thank. I would like to thank all of them for making the lab and university a nice place to work. Particular thanks to Anne, Chris, Daniel, Emmanuel, Eva,

Fernando, Hans, Isabel, Jonathan, Mariano, Michael, Oliva, Richard, Robert, and Stefan.

For the last two years I have lived with “Chris 1” and “Chris 2”, they can fight it out between them to find out who is 1 and who is 2! Thanks to them for making London a nice place to live.

Finally I would like to thank all of my family for many things, particularly making and raising me. *Ευχαριστώ πολύ το Μπαμπά μου και τη Γιαγιά μου.*

Contents

Abstract **1**

Acknowledgments **2**

1 Introduction **9**

1.1 Symmetry in Physics 9

1.2 Time Reversal Symmetry 10

1.2.1 The Electric Dipole Moment of the Electron 12

1.3 EDM Measurements 15

1.3.1 The Enhancement Factor for Molecules 19

1.3.2 Experimental Overview 22

2 The Supersonic Source **25**

2.1 The Vacuum System 25

2.2 Supersonic Expansion 26

2.3 Implementation 31

2.4 Characterisation 36

2.5 Source Stability 41

3 Manipulating the Molecules **43**

3.1 The Structure of YbF 43

3.2 Raman and Rf Excitation 46

3.3 The Laser System 51

3.4 Raman Implementation 54

3.5 Raman Transitions 57

3.6 Rf Implementation 59

3.7 Pulsed Rf Transitions 60

3.8 The Stark Shift Measurement 64

4 The Interferometer **70**
4.1 Theory . . . 70
4.2 Implementation . . . 77
4.2.1 Magnetic Field Hardware . . . 77
4.2.2 Electric Field Hardware . . . 78
4.3 Characterization . . . 82

5 Principles of the EDM Measurement **85**
5.1 Non-Statistical Noise . . . 89
5.1.1 Non-Statistical Noise Suppression . . . 93
5.2 Computer Control and Current Supply . . . 96
5.3 Data Analysis . . . 100

6 Results and Systematics **104**
6.1 Results . . . 104
6.2 Systematic Effects . . . 108
6.2.1 Internal versus External Effects . . . 108
6.2.2 Systematic Amplitude Effects . . . 110
6.2.3 Systematic Magnetic Effects . . . 113
6.2.4 Leakage Currents . . . 118
6.3 Data Analysis . . . 121

7 Conclusion and Future Prospects **128**
7.1 Conclusion . . . 128
7.2 Future Improvements . . . 128

Bibliography **131**

A **138**

List of Figures

1.1 Theoretical Prediction of the electron EDM 14
1.2 Experimental Upper Limit on Electron EDM 15
1.3 Effective electric field in YbF 21
1.4 Vacuum System 22

2.1 Vacuum System 26
2.2 Molecular Distribution for different Temperatures 28
2.3 Supersonic Expansion of a Gas 29
2.4 Valve Design 33
2.5 Supersonic Source 34
2.6 Typical Gas Pulse 37
2.7 YAG Profile Picture 37
2.8 Typical YbF Gas Pulse 38
2.9 Comparison of Oven and Supersonic Molecular Sources 39
2.10 Scan of the Flash To Q-Switch Delay 40

3.1 YbF Level Structure 44
3.2 Stark Shift of the Ground State Hyperfine Levels 45
3.3 Simplified Level Scheme for Raman Transitions 46
3.4 Optics on Laser Table 52
3.5 Raman Laser Beam Paths 56
3.6 Typical Raman Transition 58
3.7 Raman Rabi Flopping 59
3.8 Rf Rabi Flopping 60
3.9 Pulsed RF Timing Diagram 61
3.10 Scan of the rf Switch Timing. 62
3.11 Pulse rf TOFs Plotted against rf Power 63
3.12 Stark Shift Measurement 66
3.13 Theoretical Fit to Stark Shift Data 69

4.1 Raman Coupling Scheme . . . 72
4.2 Numerical Solution of Raman Transitions . . . 74
4.3 Numerical Prediction of Molecular Interference . . . 76
4.4 Inner magnetic shield and Coils . . . 79
4.5 Electric Field Plates and Support Frame . . . 81
4.6 Molecular Interference . . . 82
4.7 Molecular Interference TOF Data . . . 84

5.1 Interference Curve Data Collection Points . . . 86
5.2 PMT Amplifier Circuit Diagram . . . 87
5.3 PMT Amplifier Calibration . . . 88
5.4 Gas Pulse Noise Analysis . . . 90
5.5 Magnetic Field Frequency Components . . . 92
5.6 Magnetic Field Frequency Components . . . 92
5.7 Example Waveforms . . . 94
5.8 Example Pattern from the Pattern Generator . . . 97
5.9 EDM Current Supply Circuit Diagram . . . 99
5.10 Analysis Channels . . . 100

6.1 Typical analysis channel results . . . 105
6.2 Raw EDM for a Cluster . . . 108
6.3 Noise and BShift Drift . . . 109
6.4 Field Plate supply circuit . . . 109
6.5 ECal-BShift Systematic Effect . . . 111
6.6 ECal-BCal Systematic Effect . . . 112
6.7 Magnetometer Data . . . 115
6.8 Magnetometer EShift results . . . 116
6.9 Magnetometer EShift results for the data-set . . . 119
6.10 Magnetometer EShift hourly variation . . . 120
6.11 Leakage current monitor design . . . 122
6.12 Histogram of EDM results for the data-set . . . 123
6.13 The EDM results for the data-set . . . 124

A.1 Systematic due to detuned Raman or rf . . . 139
A.2 Systematic effect on interference lineshape . . . 140
A.3 Systematic effect on BShift . . . 141
A.4 Systematic effect on the EDM . . . 141

List of Tables

1.1 The E_{int} electric field for various polar molecules 20

2.1 Source Parameter space 36

3.1 The Raman beam parameter space 57
3.2 The rf parameter space 60
3.3 Measured Stark Shifts 68

4.1 The electric field plate separations along the z-axis of the experiment. 78

5.1 Noise sources 90
5.2 Switched parameters and their waveform names 95
5.3 Switching Waveforms 95
5.4 Analysis channel definitions. 100
5.5 Analysis channel physical significance. 101

6.1 EDM metadata 106
6.2 Machine state for Cluster 18May0534. 107
6.3 Corrected EDM for cluster 18May0534. 112
6.4 Data analysis channel results averaged over the data-set. 125

Chapter 1

Introduction

1.1 Symmetry in Physics

In order to gain some insight into the workings of the world, it has been necessary for physicists to divide the observable universe into two distinguishable groups. The complexities of nature are bundled into one group called initial conditions, and the left overs are neatly organized into simple understandable rules, which are called the laws of nature. The power of this method of abstraction is that seemingly unrelated phenomena may be correlated and understood in terms of common underlying principles. This enables humans to unravel the tangled web of the events they find before them. However, the laws of nature do not follow effortlessly after the initial conditions have been isolated. This is where the discovery of symmetries and asymmetries in nature provides an avenue for revealing these hidden laws.

One of the most obvious asymmetries, that we encounter in our everyday lives, is the difference between left and right. Our hearts, for example, are usually on the left-hand side of our bodies; however, when looking through a mirror it would appear that our heart is on the right-hand side. This observation does not necessarily imply that the laws must be asymmetric. The mirror has the effect of reversing our chosen coordinate system. If we were to attribute these asymmetries in our environment to initial conditions, we could postulate a law of nature which looks the same under the influence of the mirror. Until recently the approach to construct theories of nature was to assume that the equations of nature are invariant under reversals of the coordinate system. To understand why symmetry should be regarded so highly we consider the time reversal symmetry of a particle with spin.

1.2 Time Reversal Symmetry

The time reversal operator $\mathcal{T}$ has the effect of reversing the time coordinate $t \rightarrow -t$. The effect of applying the operator $\mathcal{T}$ on a particle with spin is to effectively reverse the direction of the spin. Let us assume that $\mathcal{T}$ is a symmetry operator. Then in the case of the electron, ignoring for now any electric dipole moment (EDM), nature can preserve $\mathcal{T}$ symmetry only if there are two internal states of electron, one "spin up" and the other "spin down". This is found in nature and so in this case the assumption of $\mathcal{T}$ symmetry is confirmed.

There are other important discrete transformation operations, coordinate reversal, parity $\mathcal{P}$, and interchange of particle with their anti-particle, charge conjugation $\mathcal{C}$. Historically these were assumed to be symmetry operations – that the properties of physical systems are invariant under the action of the transformation. These symmetries are all related by the $\mathcal{CPT}$ theorem, which states that the individual symmetries may be violated however the overall symmetry of $\mathcal{CPT}$ must still hold. That is provided that the assumptions of Pauli hold which are that the basis structure of local quantum field theories are valid, that we can use normal-ordered operators, and that the interaction Hamiltonian is Hermitian [58]. Wigner [79] discovered that $\mathcal{P}$ and $\mathcal{T}$ are symmetries of the Schrödinger equation in 1927, and soon afterward $\mathcal{C}$ was found to be a symmetry of quantum electrodynamics [39].

With the introduction of the weak and strong interactions in nuclear physics these symmetries were assumed to hold, since there were no classical analogues of the new interactions. In 1956 Lee and Yang [42] observed that there had been no experimental tests of whether $\mathcal{P}$ invariance held for the weak interaction. This paper examined parity conservation in beta, hyperon, and meson decay, it also proposed some experimental tests of parity conservation in these interactions. This paper was followed a year later with an examination of $\mathcal{C}$ and $\mathcal{T}$ invariance in Kaon decay modes [43]. These two papers led to many experimental tests of the symmetries in weak interactions.

In 1957 a famous experiment of Wu *et al* [84] showed that the weak interaction violates parity symmetry to the greatest extent. They measured the momentum distribution of electrons emitted from β-decay from a sample of spin aligned ^{60}Co atoms in a cryostat. In this experiment a thin layer of ^{60}Co was polarized in cerium magnesium nitrate and the β-decay was detected by scintillation photons in a crystal. These photons were sent through a four feet long light-pipe and detected by a photomultiplier. The apparatus was placed in a demagnetisation cryostat, the field of which defined the polarization axis of the ^{60}Co nuclei.

They observed the correlation between the spin direction σ and the momentum distribution p of the β particles emitted in the decay. To preserve $\mathcal{P}$ symmetry they expected the β particles to decay symmetrically irrespective of the spin direction, with $< \sigma \cdot p >= 0$. However, they found that β particles have a preferred direction in which they decay such that $< \sigma \cdot p >< 0$. This implied that $\mathcal{P}$ invariance was violated in the weak interaction for β-decay.

In a paper in the same issue of Physical Review the results of an experiment observing meson decay were also published [21]. They also found that $\mathcal{P}$ invariance was violated. They measured the angular distribution of positrons from successive decay of pions and muons,

$$\pi^+ \rightarrow \mu^+ + \nu \tag{1.1}$$

$$\mu^+ \rightarrow e^+ + 2\nu. \tag{1.2}$$

In this experiment they stopped a beam of pions in a carbon absorber, these pions then decayed into muons, equation (1.1). These muons formed a beam which was strongly polarized in the direction of the pion beam. This was measured by the muons decay into positrons, equation (1.2), which were detected. In [42] it was determined that if the spin-polarization of the muons emitted in equation (1.1) were along the direction of motion of the pions, parity conservation would be violated. This was the manner in which the $\mathcal{P}$ violation was measured in [21][1].

Earlier in 1957 Landau argued that symmetry could be preserved at a deeper level in the weak interaction [41]. He proposed that the combined action of $\mathcal{CP}$ could be nature's choice of symmetry operation. This means that particles with charge are free to violate $\mathcal{P}$ symmetry as long as their anti-particles do so in the opposite way. However, this supposed symmetry was found to be false when in 1964 Christenson *et al* [8] observed that long-lived neutral Kaons $\mathbf{K_L^0}$ can decay into two pions or, more frequently, three pions. $\mathcal{CP}$ symmetry requires that $\mathbf{K_L^0}$ particles decay into three pions only. The experiment [8] found strong evidence that the $\mathbf{K_L^0}$ meson was not in a pure eigenstate of $\mathcal{CP}$, and therefore violates the symmetry. $\mathcal{CP}$ violation was confirmed in [19] which measured the interference between long and short lived Kaons. Later two of the authors of [8] were awarded the Nobel prize for physics. A history of the discovery of $\mathcal{CP}$ violation and its consequences can be found in [11, 18], reviews in [4, 37, 81], and a collection of important papers in [82].

However, all symmetry is not lost because according to the $\mathcal{CPT}$ theorem the reversal of all three quantities is necessarily a symmetry operation which nature should obey [51]. This means to explain the $\mathcal{CP}$-violating kaons, $\mathcal{T}$ symmetry must

[1] Incidentally, in this paper they also measured the magnetic moment of the free muon.

be broken in a very special manner to conserve overall $\mathcal{CPT}$ invariance. In this way by measuring $\mathcal{CP}$ violation we arrive at indirect evidence for $\mathcal{T}$ violation. There is some dispute over whether an experiment has directly measured $\mathcal{T}$ violation [1, 83, 58]. This is one of the many reasons that searching for direct evidence of $\mathcal{T}$ violation is interesting. In the next section I outline the connection between $\mathcal{T}$ violation and the electron.

1.2.1 The Electric Dipole Moment of the Electron

Two physicists to propose that the universe may not by fully symmetrical were Purcell and Ramsey, who proposed that the neutron might have an electric dipole moment (EDM) [52]. It has also been proposed that the electron has such a property. The standard model of particle physics predicts that the electron is a point-like particle, a natural question to ask is therefore, how can such a particle can have an EDM?

With out delving into the 'mysteries' of the standard model we can conceptualize the effect in relation to the induced electric dipole moments of atoms. If we apply an external electric field to an atom this electric field interacts with the electron cloud surrounding the nucleus. Let us imagine that before the field is turned on the atom is in a state of well defined parity. Assuming that atoms do not violate parity on their own, there can be no net electric dipole moment of the atom. When the field is turned on, states of even and odd parity are mixed by the Stark interaction. This polarises the atom to some extent, depending on its polarisability. This shifted electron cloud is no longer symmetric about the nucleus and therefore there is a net induced electric dipole moment. The effect of the perturbation, of the external electric field, to the normal Hamiltonian of the atom causes the dipole moment to appear.

According to the standard model, the electron is constantly surrounded by a cloud of virtual particle which mediate various forces. In a quantum vacuum there are constantly particles being created and destroyed, this is the environment in which the electron "sits". The interactions between the electron and the vacuum causes a net displacement of the electron's charge from its centre of mass producing an EDM. This is because some of the virtual particles from the vacuum break time reversal symmetry and parity. Because the quantum vacuum is always providing this perturbation the electron can have a permanent EDM.

Now we have seen how the electron could have such a property we also envisage that it must lie parallel or anti-parallel to the spin axis. This is due to the Wigner-

Eckart theorem [15]. Also it is realized that the existence of such an EDM must violate $\mathcal{T}$ and $\mathcal{P}$ symmetry [4]. This is because under time reversal the spin-axis is reversed but the EDM is not. Therefore, time reversal symmetry predicts that the electron should have two states of the EDM. One variety aligned parallel to the spin and another with anti-parallel EDM and spin. Since only two internal states of electrons are found in nature (those with spin up and others with spin down), time reversal symmetry is violated if the electron has an EDM. Parity is also violated because the EDM is reversed under a $\mathcal{P}$ transformation, while the spin is not, giving the four internal states of electrons again. However, as $\mathcal{P}$ violation has been shown on numerous occasions, it is more interesting to search for $\mathcal{T}$ violation effects.

Over the years there have been many experiment to measure the EDM of the electron and of the neutron. I explain later how many of these experiments actually measure the EDM of the electron by its perturbation to the structure of atoms or other systems. First, however, I briefly explain a measurement on the neutron. A large number of neutron EDM experiments have taken place over the past 40 years each experiment decreasing the experimental error and thus placing a smaller upper limit on the size of any $\mathcal{T}$ asymmetry. All results have been consistent with zero, and although there have been a large number of searches in atomic, nuclear, and particle physics, no instance of $\mathcal{T}$ violation has been found in these systems. The current experimental limit on the EDM of the neutron is $(-7.0 < d_n < 5.0) \times 10^{-26}$ $e.cm$ [24] with a 90% confidence interval. To put this result into context, various extensions to the standard model of elementary particles predict values ranging between 10^{-25} to 10^{-27} $e.cm$ [16]. In the measurement [24] they used the Ramsey separated oscillatory magnetic field resonance method [53] to measure the Larmor precession of spin-polarised neutrons. The ultracold neutrons were held in a cell and interacted with highly-uniform electric and magnetic fields. The EDM signal was the difference between the Larmor frequencies with the electric field parallel and anti-parallel to the magnetic field,

$$\begin{aligned} h\nu_{\uparrow\uparrow} &= 2(\mu_n \cdot B + d_n \cdot E) \\ h\nu_{\uparrow\downarrow} &= 2(\mu_n \cdot B - d_n \cdot E). \end{aligned} \tag{1.3}$$

The spin-polarised neutrons first interacted with a oscillating magnetic field the frequency of which was approximately the Larmor frequency. The neutrons then coherently evolved in the electric and magnetic field for approximately 15 seconds and then interacted with a second short interval of oscillating magnetic field. The number of neutrons with spin up were then recorded as were the spin down neutrons. To eliminate troublesome magnetic systematic effects and drifts from the data an

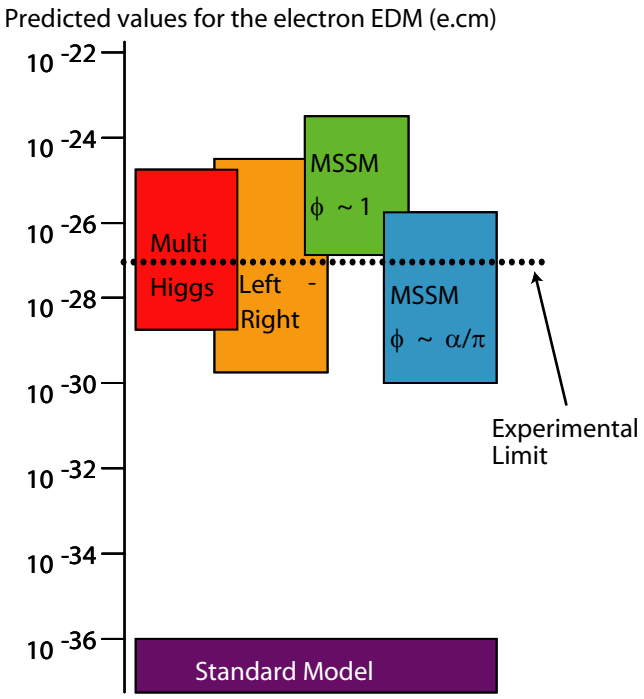

Figure 1.1: The theoretical predictions of the electron EDM for various models.

optical pumping mercury co-magnetometer was used.

This result and others like it imply that nature is highly selective in $\mathcal{T}$ symmetry violation, and this puts very tight constraints on theoretical explanations. The standard model of elementary particle physics attempts to explain $\mathcal{T}$ violation effects in kaons and in doing so also constrains the value of the electron EDM. The standard model has two mechanisms which violate $\mathcal{CP}$ symmetry and therefore $\mathcal{T}$ symmetry [50]. Through these mechanism the standard model predicts a range of values for the neutron EDM between $10^{-32} - 10^{-31}$ $e.cm$ [22, 34] and similarly the electron EDM is predicted to be well below 10^{-36} $e.cm$ [36]. These values are well below the current upper limits, and hence an experimental discovery of the electron or neutron EDM would reveal new physics, unexplained by the standard model. This discovery might not shock the scientific community however, because many physicists believe the standard model to be incomplete. Indeed there are numerous ideas as to the physics beyond the standard model, all providing a range of possible values for the electron and neutron EDMs. Figures (1.1,1.2) show the predicted electron EDM and its experimental upper limit over time, respectively. The blue points of Figure (1.2) show the results of various searches for the electron EDM. They show that the upper limit has steadily decreased over the years. The

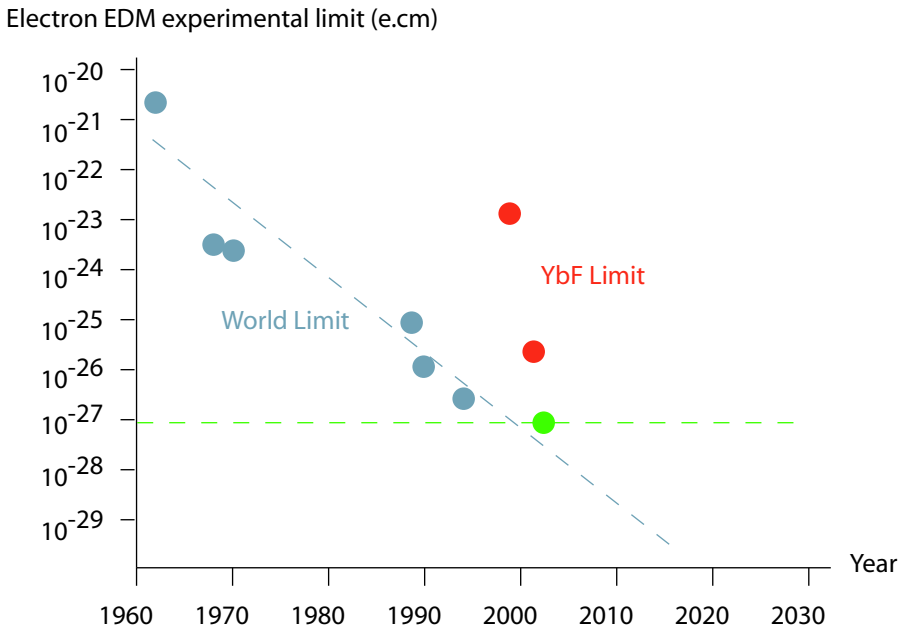

Figure 1.2: The experimental upper limit of the electron EDM against time. The data is from a range of experiments. The horizontal dashed-line indicates the current upper limit on the electron EDM.

green point and dashed line shows the current best upper limit published in 2002 [56]. The red points are the preliminary results from the experiment using YbF molecules. The predicted values from standard model extensions for the EDM of the electrons are between $10^{-25} - 10^{-30}$ $e.cm$ [7, 9, 28], as shown in Figure (1.1). This makes searching for the EDM of the electron an interesting pursuit since the current experimental limit is well inside this range [56].

1.3 EDM Measurements

In this section I give a brief description of some of the important experiments to measure the electron EDM. These are presented in historical order. The first upper limits to constrain the value of the electron EDM were made by reanalysis of data from the Hydrogen Lamb shift [17, 60] and electron spin-precession rates from anomalous magnetic moment [49] experiments. These experiments were not designed with measuring the electron EDM in mind. However they made a limit of 10^{-15} $e.cm$. After this, an experiment was made to measure the electron EDM specifically. This experiment looked for the EDM interaction in electrons elastically scattering from He^4 and provided a small improvement of the EDM upper bound

[23]. The experiment also established, in 1963, that the EDM was $\leq 10^{-15}$ $e.cm$.

In 1963 a famous paper by Schiff [67] showed that, to a first approximation, an atom or molecule has no permanent EDM even if its constituents do. However, he also observed that higher order effects can get around this theorem. He proposed two mechanisms, the effect of taking into account the volume of the particle, and a relativistic effect. The second of these mechanisms is important here because the electron is regarded as a point particle in the standard model, so we must rely on relativity to overcome Schiff's electrostatic shielding of other electrons within the atom or molecule. The relativistic effect not only gives access to the EDM interaction with an external electric field, in heavy atoms and molecules the interaction can even be enhanced. The enhancement factor was first reported in 1965 by Sanders [61]. These theoretical discoveries led to an increased interest in using atoms and molecules as media for particle EDM measurements.

The first notably large increase in sensitivity was made in 1964 in a Cs thermal atomic beam experiment [62]. This was one of the first experiments to search for the electron EDM using an atomic source. In this experiment they used much the same technique as most EDM experiments which is to use a Ramsey separated oscillatory magnetic field technique. In this experiment they drove two radio-frequency (rf) Zeeman transitions, $(4,-4) \rightarrow (4,-3)$, in the Cs atoms separated by a region of electric field. The Cs atoms were detected by recording the ion current from a hot-wire detector.

They measured the change in resonance frequency of the atoms produced by a simultaneously applied dc and ac component electric field. The shift of the resonance frequency of the atoms is of course due to the quadratic Stark interaction and the effect of the electron EDM interaction. The oscillating component of the electric field was used to phase lock the experiment to that oscillation frequency. The experiment found an atomic Cs EDM of $(2.2 \pm 0.1) \times 10^{-19}$ $e.cm$ and deduced an electron EDM 100 times smaller due to the enhancement factor of the Cs atoms. This non-zero EDM was attributed to systematic effects in their experiment. The main one being the interaction of the Cs atoms with the motional magnetic field, $B = (v \times E)/c$, where v is the velocity of the atoms. This systematic effect has been problematic for many atomic EDM experiments, see Section (6.2) in Chapter (6) for more details. They resolved the problem by applying magnetic fields to cancel the problematic field and directly measured the field with different alkali atoms [71]. In their subsequent measurement a year later they improved the upper limit of the electron EDM to $d_e < 3 \times 10^{-24}$ $e.cm$ [78] a factor of ten better than any previous measurement.

Another experiment to use Cs atoms as a sensor for the electron EDM was published in 1989. This experiment used optically pumped ground state Cs atoms contained within a vapour cell which also contained N_2 molecules to minimise the spin-relaxation of the Cs [48]. By optically pumping they spin-polarised the Cs along the x-axis and applied an electric field along the z-axis, they then looked for a small precession of the polarisation into the y-axis due to the EDM interaction with the electric field.

To cancel the effects of stray magnetic fields they used two vapour cells one on-top of the other inside a four layer magnetic shield. The electric field applied to the two vapour cells was orientated in the opposite directions, and by taking the difference between the precession signals the EDM signal was doubled, and the precession due to magnetic fields was cancelled. Notably the electric field used in this experiment was rather small at 4 kV/cm. This was to reduce the effects of leakage current across the cells which would have caused systematic problems. This was not ideal because it also reduced their sensitivity to the EDM.

The leading systematic effect in this measurement was caused by imperfect reversal of the electric field. This is due to the Stark interaction shifting the energy of the magnetic sublevels of interest. However, they were able to determine the contribution to the electron EDM from imperfect reversals of the electric field. Using this as a correction they found an electron EDM of $(-1.5 \pm 5.5 \pm 1.5) \times 10^{-26}\ e.cm$.

The best upper limit on the electron EDM was measured with Tl atomic beams and published in 2002 [56]. This experiment used a total of eight atomic beams to measure the EDM and correct for the motional magnetic field systematic. Again they used the typical method of magnetic resonance with two oscillating rf fields split by a region of electric field, this time using laser optical pumping for state selective pump and probe beams. The eight atomic beams consisted of two sets of two counter-propagating Tl beams and two Na beams. The two sets of four beams were separated by a short distance. The Na beams were used as a co-magnetometer since Na is not sensitive to the EDM. Tl on the other hand has an enhancement factor of -585. The experiment was set up such that each set of four Na and Tl beams would interact with the same magnetic field and electric fields, and the other sets of four beams would interacted with same magnetic field but an electric field in the opposite direction. This enabled common-mode noise rejection and control over systematic effects.

Another of the experimental achievements was to make an electric field of over 100 kV/cm while keeping leakage currents below 2nA. These leakage currents and the charging currents from the electric field were measured using the quadratic

Stark interaction of Tl, and were controlled to avoid systematic problems. Their full data-set was taken at night because the magnetic noise in the day limited their sensitivity. After suitably correcting for the motional magnetic field systematic, they found an electron EDM of $d_e = (6.9 \pm 7.4) \times 10^{-28}$ $e.cm$ with a 90% confidence limit of $|d_e| \leq 1.6 \times 10^{-27}$ $e.cm$ [56]. More details of this experiment can be found in [57]. This concludes the historical review of EDM experiments. However, before I turn to the experiment using YbF molecules it is interesting to look at some up-and-coming experiments using molecules and other materials to measure the electron EDM.

One of the most interesting is the experiment to measure the EDM in a cell of PbO molecules. This experiment is currently underway at the Yale University in the group of DeMille [12]. Although the enhancement factor for PbO is not as large as for YbF, the PbO molecule offers some advantages. The first of which is that unlike YbF, PbO is chemically stable and can be easily vaporised and stored in a vapour cell. This offers the possibility of high densities of PbO for efficient detection. One of the normal disadvantages of performing an EDM experiment on a species in a vapour cell is that large electric fields can not be produced without troublesome leakage currents accompanying them. For PbO, however, the molecule is almost fully polarised in a field of 15 V/cm which enables small electric fields to be used without compromising on sensitivity. The polarisation of the molecules and it significance in relation to the EDM is outline in the next section. Another advantage of PbO is that in the meta-stable state which the EDM measurement would use there are two levels, one with the EDM parallel to the spin and the other with them oppositely directed. This offers the possibility of performing co-magnetometery at the same time as measuring the EDM, within the same molecule. Performing the EDM experiment with this meta-stable state also produces a significant disadvantage which is the lifetime of the molecules in this state is only 80 μs. That gives a broad linewidth making it difficult to measure small energy shifts. Currently this experiment is still in the development stage [33].

Recently renewed interest has appeared about the possibility of measuring the electron EDM in solid state systems [40]. These systems have predicted sensitivities in the range of $10^{-32} - 10^{-35}$ $e.cm$ [40]. The idea here is that the strong electric fields can be applied to solid state systems with unpaired electrons that can spin-polarise the sample. This magnetisation can change the magnetic flux at the surface producing a signal proportional to the EDM. The current generation of experiment uses a material called gadolinium-iron-garnet, GdIG, and recently published a limit on the electron EDM of 5×10^{-24} e.cm which is a factor of 40 improvement over the

previous measurement in a solid state system [26]. However, this result was limited by an imperfectly reversing magnetic field systematic effect of unknown origin.

Now we turn to the YbF experiment which is the subject of the rest of this thesis. The current best published measurement of the EDM using YbF molecules is $(-0.2 \pm 3.2) \times 10^{-26}$ $e.cm$ using a thermal YbF molecular beam [30]. This is the best ever published result using any molecule. For a full description of the technique see [29]. My PhD work has been to significantly increase the sensitivity of the YbF experiment, principally by means of the development and implementation of a supersonic source of YbF. Other improvements include the implementation of laser driven Raman and pulsed rf transitions, steps towards co-magnetometers, a new data acquisition and analysis system. This has lead to a significant increase in sensitivity of the experiment of over forty. Details of the above improvements can be found in the following chapters of this thesis. In the next section I give a brief discussion of the enhancement factor for the YbF molecule and other molecules like it.

1.3.1 The Enhancement Factor for Molecules

As mentioned above, Schiff pointed out that the induced EDM of an atom exactly cancels the EDMs of the constituent particles in the approximation of point particles with Coulomb interactions. However, he showed that relativistic effects in the atoms have the effect of altering the shielding of the EDM. To include the effects of relativity, we must solve the Dirac equation. The energy of the electric dipole interaction can be written in the effective form [27],

$$\langle \mathcal{H}^1 \rangle = \left\langle \psi^0 \left| \begin{array}{cc} 0 & 0 \\ 0 & 2d_e \boldsymbol{\sigma} \cdot \boldsymbol{E} \end{array} \right| \psi^0 \right\rangle \tag{1.4}$$

Where σ is a unit vector along the electron spin and E represents the total electric field at the electron, including the external and internal electric fields. ψ^0 is the wavefunction of the molecule in an electric field. This effect is entirely relativistic and scales rapidly with the mass of the atom or molecule. Indeed it can be shown that interaction scales as the nuclear charge cubed [35], and therefore, heavy atoms or molecules are the natural choice for performing a measurement. We also find that in the absence of an external field the interaction is zero if ψ_0 has a defined parity because of the odd parity of the operator. However, an external electric field polarises the atom or molecule which mixes in other-parity orbitals from other states. This lifts the symmetry of the atom or molecule and the interaction energy becomes non-zero. In atoms this effect is roughly linear in the applied electric field

Molecule: State	E_{int} (GV/cm)
BaF: $X^2\Sigma^+$	7.4
YbF: $X^2\Sigma^+$	26
HgF: $X^2\Sigma^+$	99
PbF: $X^2\Sigma^+$	-29
PbO: $a(1)^3\Sigma^+$	6

Table 1.1: The E_{int} electric field for various polar molecules [29].

leading to a fixed enhancement of the EDM interaction relative to that for a bare electron.

In polar molecules the states are naturally mixed due to large polarisations along the internuclear axis. This leads to large enhancements of the electron EDM, far greater than those found in atoms. If the molecules is rotating in the laboratory reference frame then the effect averages to zero. Fortunately the application of a small electric field aligns the internuclear axis of the molecule to the direction of the applied field. Evaluation of the interaction, equation (1.4), gives an energy shift to the molecular levels of,

$$\Delta E = -d_e \eta E_{int} \tag{1.5}$$

where E_{int} is the internal effective electric field of the molecule at the electron, and η the degree of polarisation of the molecule with respect to the applied electric field direction. To calculate the polarisation or alignment of the molecules to the applied field direction we must evaluate the Stark interaction for the molecules. To do this we diagonalize the Hamiltonian for a rigid rotor with the extra Stark Hamiltonian, $H_s = -\mu \cdot E = \mu E \cos\theta$, and take the derivative with respect to E. Where E is the externally applied electric field and μ the magnetic moment of the ground state, see [64] for YbF. Figure (1.3) plots the effective electric field of the molecules $E_{eff} = \eta E_{int}$ against the applied field in the laboratory for YbF. We find that the enhancement factor for YbF saturates as the molecule becomes aligned to the external field. For YbF $E_{int} = 26\ GV/cm$ and this is the maximum that E_{eff} can reach, occurring when the molecule is fully polarised. This has been calculated with various different techniques, all with good agreement [38, 47, 74]. This enhancement factor made YbF a very attractive choice of molecule for a EDM experiment. In Table (1.1) E_{int} is listed for various molecules. One notes that although YbF does not have the largest of these fields, it does have a high valve. The reasons, therefore, for choosing one molecule over another is the ease of production and other experimental considerations.

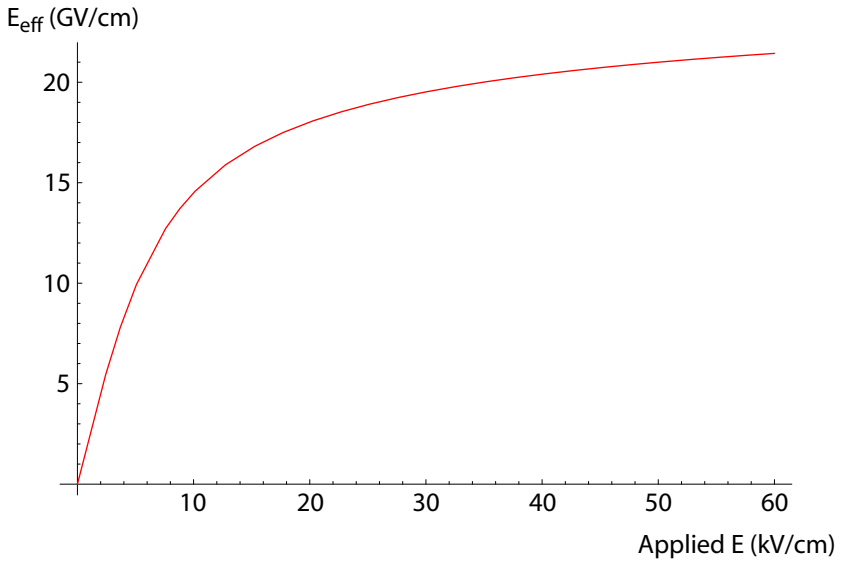

Figure 1.3: A plot of the calculated effective electric field E_{eff} of the molecule which enhances the measurement of the electron EDM. Note that the y-axis is in units of (GV/cm) while the x-axis is in (kV/cm).

Another reason for choosing to use polar molecules in an electron EDM experiment is the relative insensitivity of the molecules to magnetic fields transverse to the electric field. When the molecules are aligned to the applied electric field, they are effectively "pinned" to the electric field direction. This suppresses the interaction with dc magnetic field components perpendicular to the electric field direction by many orders of magnitude. Thus the main systematic effects that have hampered atomic experiments are naturally heavily suppressed in polar molecules, see Chapter (6) for details.

The reader may be wondering at this stage why polar molecules have not been used in the past to set new limits on the electron EDM. One of the reasons for this is that it is relatively difficult to produce a high-density source of polar molecules compared with atoms. In resent years though there has been a great interest in finding techniques to produce high-intensity sources of cold molecules. This has been stimulated by a large number of possible application of cold molecules for experimental science and also from the great success of cooling atoms to very low temperatures. These developing methods, such as buffer gas cooling of molecules [77, 46], photo-association with additional excitation to the ground state [59], using Feshbach resonances with pre-cooled atoms [31], cavity cooling [75], and deceleration and trapping of cold molecules [73], could lead to ultra-sensitive precision

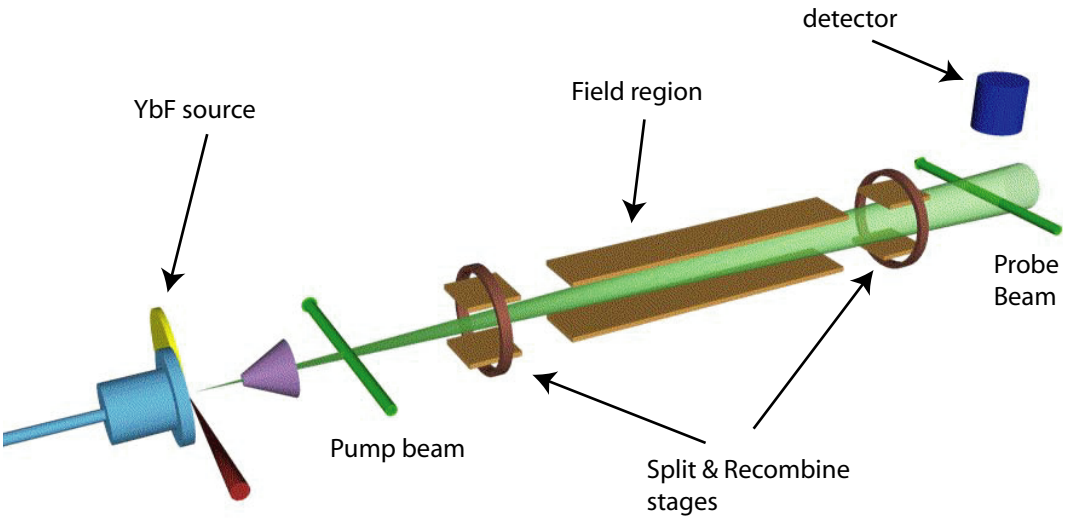

Figure 1.4: Overview of the experimental setup

measurements using molecules in the future[2].

1.3.2 Experimental Overview

Now we have motivated the reasons for attempting to measure the electron EDM in a molecule, I give a brief summary of the experimental method described in the rest of this thesis. In short we use a magnetic resonance technique with two oscillatory rf fields separated by a region of electric and magnetic field [53]. To measure the small effect of the electron EDM on the molecules we employ a very sensitive interferometric technique. Figure (1.4) shows an overview of the experimental setup.

As with all electron EDM experiments we need to produce a superposition state and measure the effect of the EDM on this state. In most cases, to get long lifetimes, the ground state levels are the natural choice, as indeed they are for this experiment. The structure of YbF is described in detail in Chapter (3), for now it is important only to note the hyperfine structure of the ground rotational, vibrational and electronic state. This state is "Hydrogen like" in that it has F=0 and F=1 hyperfine levels. These are split by a frequency of approximately 170 MHz. The only other level of interest here is the first electronically excited state which will be denoted $|A\rangle$. Transitions between the ground state levels $|X\rangle$ and the $|A\rangle$ state are accessible with a dye laser emitting at approximately 552 nm.

To start the experiment we produce a pulse of YbF molecules, which are thermally distributed at a few Kelvin among the molecular states and travelling through

[2]For a review of production methods and applications of cold molecules see [5].

the experiment. The ground state F=0 and F=1 levels are all populated. We now depopulate the F=1 states by applying a pump laser connecting the F=1 to the upper $|\ A\rangle$ state. The molecules are optically pumped out of the F=1 level and are unlikely to repopulate it since they can decay into many other molecular states. The optical pumping can be optimised by adjusting the power in the pump beam and by changing the overlap of the pump beam with the molecular beam. The efficiency of the pumping is estimated to be around 96%, with 23% of these pumped out molecules decaying into the ground F=0 state [72]. Typically the pump laser power is set to around 2 mW with a beam diameter of around 3 mm. This corresponds to an intensity of around 28 $mW.cm^{-2}$ which is enough to saturate the transition.

After the pump stage the wavefunction of the remaining ground state molecules can be written $\Psi = |\ 0,0\rangle$, where $|\ 0,0\rangle$ labels the F=0, $m_F = 0$ ground state level. The quantisation axis is defined by the direction of the applied electric field and these states are labelled in that basis. Now the molecules undergo a transition to the F=1 $m_F = \pm 1$ levels, $|\ 1,\pm 1\rangle$. This stage, called the "split" stage puts the molecules into a coherent superposition of the $|\ 1,\pm 1\rangle$ levels. The action of this transition is to produce the transformation,

$$|\ 0,0\rangle \rightarrow \frac{1}{\sqrt{2}}(|\ 1,1\rangle + |\ 1,-1\rangle). \tag{1.6}$$

In an analogue with an optical interferometer, this stage plays the role of the first beam splitter of the interferometer. The molecules now continue to travel through the experiment and interact with an electric and magnetic field applied along the z-axis. These fields interact with the molecules and cause the $|\ 1,\pm 1\rangle$ components to coherently evolve a phase difference. This phase is proportional to the Zeeman interaction energy and the EDM interaction with the electric field. The wavefunction after this evolution stage is written,

$$\Psi_{EB} = \frac{1}{\sqrt{2}}(e^{i\phi}\ |\ 1,1\rangle + e^{-i\phi}\ |\ 1,-1\rangle) \tag{1.7}$$

where $\phi = -(\mu_B B \mp d_e.E_{eff})\tau/\hbar$ is the phase, and τ is the time spent in the fields. The choice of $\mp$ in ϕ depends on the relative direction of the electric and magnetic fields, which can be parallel or anti-parallel. Continuing the analogue with the optical interferometer the $|\ 1,1\rangle$ and $|\ 1,-1\rangle$ states form the two arms of the interferometer with a phase evolving between them.

Now the molecules are "recombined" with a second transition connecting F=1 to F=0. The second beam splitter of the interferometers. In the recombination the two amplitudes from the $m_F = \pm 1$ states interfere with each other affecting the population transfer to the $|\ 0,0\rangle$ state. This interference depends on the phase

evolved in the previous stage of the interferometer. Thus the population left in F=1 state depends on the phase and therefore on the EDM of the electron. Now all that is left for us to do is to count the number of molecules in the F=1 state. This is done by laser induced fluorescence of the molecules, which undergo the transition from F=1 to the $|\ A\rangle$ state and decay spontaneously. These spontaneously emitted photons are detected by a photomultiplier detector. The signal recorded in an idealized experiment would be $sin^2(\phi)$. In this way the fluorescence rate detected is related to the EDM of the electron.

The rest of this thesis contains a detailed description of the experimental techniques and apparatus used to measure the electron EDM in a supersonic YbF beam. Chapter (2) describes the newly build supersonic source of YbF, which replaces a thermal oven source [54, 29]. Chapter (3) concerns a description of the newly implemented optical Raman transitions used in the split stage of the interferometer. This Raman technique replaces the rf oscillating magnetic fields which were used in [54, 29]. In Chapter (4) I detail the action of the interferometer describing how it can be modelled and how this model compares to the experimental data. Then in Chapter (5) describe how we use to the interferometer to measure the electron EDM, paying particular attention to the noise performance. In the penultimate chapter, Chapter (6), the results obtained by this technique are reported and analysed, with particular attention paid to possible systematic effects that may be present. In the final chapter, Chapter (7), I draw conclusions on the work presented in the preceding chapters and remark on the future prospects for this experiment.

Chapter 2

The Supersonic Source

Within this chapter the molecular source will be described along with the vacuum system required for the production of the YbF molecular beam.

2.1 The Vacuum System

The EDM experiment has a beam of YbF molecules that propagates through the length of the experiment. In order to scatter as few molecules out of the beam as possible the background pressure must be low. The criterion is that the YbF's mean free path in the background gas should be longer than the beamline. The background pressure must therefore be below a few times 10^{-6} mbar.

The vacuum system comprises two chambers, three turbo pumps, and two roughing pumps. Figure (2.1) shows a schematic of the vacuum chamber layout. Starting at the bottom, the first chamber is the source chamber which is a six way cross. Bolted to the bottom flange of the cross is the source valve mount. The four vertical flanges of the cross are occupied with the source turbo pump and other hardware required for the source. A gate valve occupies the top flange of the cross. On top of the gate valve is the interaction and detection chamber which holds the three sets of electric field plates, the detection hardware, and windows for laser access. This section is pumped by the second turbo pump just above the gate valve and a third on the top. The chambers are made from stainless steel with Conflat type connections. They are sealed together with either copper gaskets or Viton rubber o-rings. Typically Viton is used to seal the source chamber connectors. This is because the source chamber is opened frequently.

The source turbo pump and its roughing pump provide high pumping speeds and are capable of running at high pressures. This handles the large gas load in the source chamber when the source valve is pulsed opened. Before the gate valve

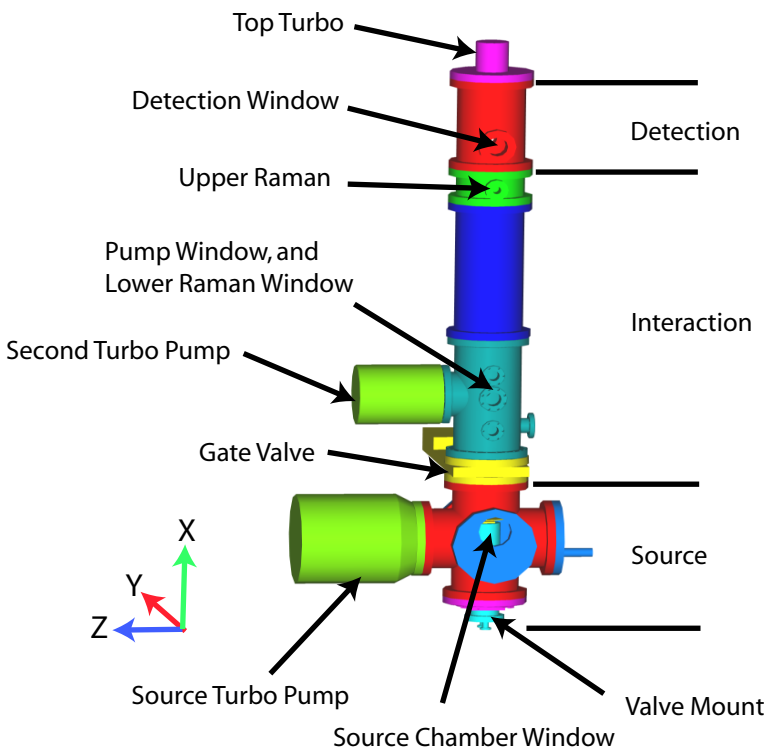

Figure 2.1: This shows a schematic of the vacuum system

is a skimmer with a 2 mm orifice, through which the molecular beam passes to the interaction and detection chamber. With typical operating conditions the source chamber pressure is of the order of 10^{-4} mbar, and the upper chamber is below 5×10^{-7} mbar. The source chamber and the upper chamber pressures are measured with Penning gauges. There are also two thermocouple gauges on the roughing lines to the turbo pumps.

2.2 Supersonic Expansion

Prior to my thesis work, the YbF molecules were produced in an effusive oven source. A major part of my thesis was the installation of a new supersonic source. This makes YbF by ablating Yb into a carrier gas of Ar, and a small amount of SF_6, which expands into the source vacuum chamber through a valve. Throughout this thesis I refer to this source of molecules as "the supersonic source". I now give a brief description of the properties of the supersonic source.

In the characterisation section, Section (2.4), of this chapter I compare the

new source's performance with the oven source. With this in mind, it is useful to understand one of the reasons for choosing to make YbF with a supersonic source as opposed to a thermal source. The old thermal source heated up a crucible of Yb and AlF_3 to around 1500 K [29] to produce an effusive beam of YbF. Due to the high internal temperature of the molecules in the beam the spectrum had many overlapping lines. In the EDM experiment we are interested in a transition from the ground state and would like to detect this transition with as little background as possible. The supersonic source enables this because it is possible to cool the degrees of freedom of the molecules in the beam to around 1 K, this reduces the background signal. The distribution function of vibrational and rotational levels for a thermal gas in thermal equilibrium at temperature T is

$$P(N,\nu) = \frac{(2N+1)Exp[-\frac{h}{kT}(BN(N+1)+\nu_0(\nu+\frac{1}{2}))]}{\sum_{i,j=0}^{\infty}(2i+1)Exp[-\frac{h}{kT}(Bi(i+1)+\nu_0(j+\frac{1}{2}))]} \tag{2.1}$$

where N and ν are the rotational and vibrational quantum numbers. For YbF in the ground state $B = 7.4$ GHz is the rotational constant, and $\nu_0 = 1.4 \times 10^4$ GHz is the vibrational constant. If we make the assumption that the molecules in the supersonic source have fully thermalised, the probability of molecules occupying the vibrational $\nu = 0$ state for 1500 K and 10 K thermal gasses is approximately 35% and 100% respectively. The probability of molecules occupying the rotational $N = 0$ state, within the vibrational ground state, for 1500 K and 10 K is approximately 0.023% and 35% respectively. Producing cold molecules therefore, dramatically increases the molecular population in the ground ro-vibrational state used in the experiment. Figure (2.2) shows the rotational distributions for 1500 K, the red curve, and 10 K, the blue curve. The vibrational state is $\nu = 0$ for each and the 1500 K curve is increased by a factor of ten for visibility. The figure illustrates the large population difference in the lower rotational states between the hot and cold molecular beams as described above. The two reasons for using the supersonic source to produce the YbF beam are that the molecules are cooled to low temperatures, as highlighted above, and that the source is pulsed. This significantly decreases the background measured by the detector, without compromising on the total signal detected.

To illustrate the physics behind the cooling process highlighted above let us consider a simple molecular beam source with a reservoir of carrier gas connected to a vacuum chamber via a valve. When the valve is opened the gas flows through the valve into the vacuum. If the valve diameter was set much smaller than the mean free path of the molecules then once in a while a molecule would drift through the valve undergoing no collisions, and therefore, its velocity would be unaffected

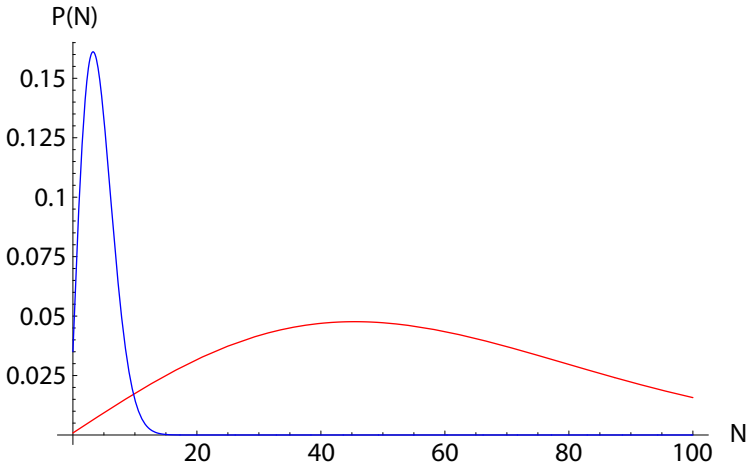

Figure 2.2: The blue curve is the rotational state probability distribution for the a thermal gas at 10 K. The red curve is the same distribution at a temperature of 1500 K, which has been increased by a factor of ten. Both distributions are plotted in the most occupied vibrational state, $\nu = 0$.

upon travelling through the valve. This type of gas beam is called an effusive beam. If on the other hand, the valve hole diameter was set to be larger than the mean free path of the molecules in the reservoir the molecular distribution on the vacuum side would be narrower than on the reservoir side. This is because the molecules near the valve are likely to travel through it creating an area of low pressure near the valve. This pressure difference drives molecules towards the valve by collisions with other molecules. This increases the mean escape velocity of the molecules through the valve. To accommodate this increase in velocity, energy is converted from the thermal energy of the molecules into kinetic energy. Thus the molecules in the molecular beam produced have a higher mean velocity and a narrower velocity distribution than the molecules in the reservoir. The rotational, translational, and vibrational temperatures of the molecules in the beam are reduced.

A comprehensive approach to the thermodynamics of the expansion through the valve is to consider conservation of energy. In this analysis we can neglect the heat conduction to the walls of the valve because the time it takes to get through the valve is short compared to the diffusion time. The diffusion time is the time it takes for a particle to come into contact with the walls of the valve. This means that the gas flowing through the valve is not in thermal contact with the walls of the valve and therefore the temperature of the gas can not change in passing through the valve. Since the carrier gas reservoir before the valve has a high density and

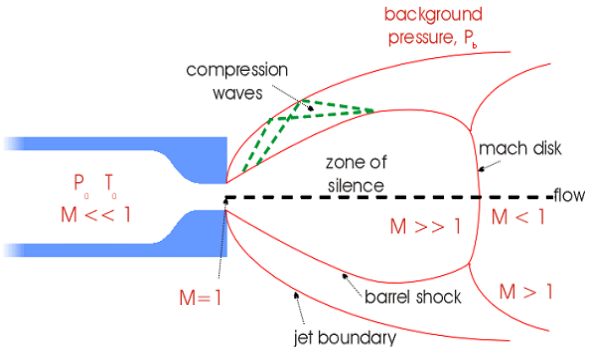

Figure 2.3: This shows the different regions of behaviour of a gas undergoing a free supersonic expansion through a nozzle. This Figure is originally from [68].

collision frequency we may assume continuum flow. If we also assume no viscous effects then there is no change in entropy in the expansion. This type of flow is called an isentropic flow. The gas within the reservoir before the valve has a bulk average velocity taken to be negligibly small. The gas immediately at the exit of the valve is at lower pressure than the stagnation state pressure, the pressure of the gas in the reservoir. This pressure difference accelerates gas through the valve reaching the local speed of sound, Mach number $M = 1$. As the gas expands through the valve the pressure gradient drives an acceleration to $M >> 1$. The background pressure "information" can only be relayed at the local speed of sound. This means that gas in the supersonic expansion is "unaware" of the ambient background pressure, and this area is call the "zone of silence". This leads to the formation of shock waves which reduce the Mach number and allow the gas pressure to adjust to the ambient pressure conditions. Figure (2.3) shows a diagram of the different regions of the supersonic expansion. Within the zone of silence the expansion is isentropic and the jet is free from external boundary conditions set by the ambient background pressure. From this region the particle beam is extracted by placing a skimmer, whose orifice is within the zone of silence. The particle beam extracted is a free supersonic jet which is unaffected by shock waves.

We may now consider energy conservation in the free expansion of the jet. As mentioned above, the process is isentropic and the gas does no work in the expansion. However, there is flow work done on the gas in the reservoir and after the valve. Taking this into account and recalling that the bulk average gas velocity in the reservoir is zero, gives the following energy balance,

$$U_0 + P_0V_0 = U_1 + P_1V_1 + \frac{1}{2}m\nu_1^2 \tag{2.2}$$

where U is the internal energy, P the pressure, V the volume, ν the bulk average

velocity of the gas, and m the mass of gas. The subscripts 0 and 1 indicate the parameters before and after the valve exit respectively. We can also divide through by the mass and substitute the specific enthalpy, $h = \frac{U+PV}{m}$, into the expression, leaving

$$h_0 = h_1 + \frac{1}{2}\nu_1^2. \tag{2.3}$$

Following the treatment in [68], this may be rearranged for the velocity after the expansion, dropping the subscript,

$$\nu^2 = 2(h_0 - h_1) = 2\int_T^{T_0} c_P dT \tag{2.4}$$

where $c_P = \frac{\partial h}{\partial T}$ is the specific heat capacity at constant pressure. This assumes that the inert carrier gas behaves as an ideal gas. In which case the enthalpy is only a function of temperature and does not depend on the pressure or volume, $H = \frac{5}{2}kT$. Also for an ideal gas $c_P = \frac{R}{W}\frac{\gamma}{\gamma-1}$ and can be considered constant with temperature. R is the gas constant, W is the molecular weight and γ is the ratio of specific heats. The velocity now becomes

$$\nu = \sqrt{\frac{2R}{W}\frac{\gamma}{\gamma-1}(T_0 - T)}. \tag{2.5}$$

It is convenient to substitute in the Mach number $M = \frac{\nu}{a}$, where a is the local speed of sound which is $a = \sqrt{\frac{\gamma RT}{W}}$. We can also rearrange for the temperature ratio, leaving

$$\frac{T}{T_0} = (1 + \frac{\gamma-1}{2}M^2)^{-1}. \tag{2.6}$$

This means that once the Mach number is known all thermodynamic variables may be calculated for the free jet. The Mach number can be calculated numerically using the equations of fluid dynamics, see [68] for details.

As mentioned above, we have assumed in this analysis that the gas behaviour is ideal, the flow is isentropic, c_P is constant, and we have continuum flow. The latter two of these assumptions should be looked at more closely. The assumption that c_P is constant in temperature over the cooling range of the expansion can be validated by considering the structure of the carrier gas which is mostly made from Ar. The internal degrees of freedom of Ar stop changing at high temperatures and therefore in the cooling range of the expansion the degrees of freedom are fixed at 3. This means that c_P is constant over the cooling range.

The last assumption of continuum flow breaks down at some distance from the valve. This is because the molecular collision rate drops as the gas expands and at some point the gas can not maintain continuum flow. At this point the

transition to free-molecular flow begins. This region is called the "freezing region" because the thermodynamic properties of the gas stop evolving. In this region the temperature ceases to decrease further, and the velocity of the gas is set. The velocity distribution, far from the valve, is of the form [2],

$$f(\nu)d\nu = N\nu^3 Exp\left[-\frac{m}{2k_BT}(\nu-\nu_0)^2\right]d\nu \tag{2.7}$$

where N is a normalisation factor, k_B is Boltzmann's constant, ν_0 is the mean velocity, m is the mass of the molecule, and T is the translational temperature. If the valve is pulsed for an infinitesimally small time, a detector at distance L downstream from the valve will see a corresponding time of flight (TOF) profile,

$$h(t) = \frac{NL^4}{t_0^5}Exp\left[-\frac{mL^2}{2k_BT}\left(\frac{t-t_0}{t_0^2}\right)^2\right] \tag{2.8}$$

where $t_0 = L/\nu_0$ [72]. This approximates $t \approx t_0$ and results in a Gaussian time of flight profile. We will see that this TOF profile describes the data reasonably well, Figure (2.8).

2.3 Implementation

This section explains our physical realisation of the supersonic source of YbF. A characterisation of the performance of this source is presented in Section (2.4).

The main components required for a supersonic source are a valve with a correctly sized aperture, a gas handling system of some kind, a skimmer, and a vacuum system. We use a commercially available valve with a 1 mm aperture, which can be operated at a range of repetition rates. We have successfully operated the valve between 5 and 100 Hz. The valve is connected to a control computer which triggers it. Figure (2.4) shows the design of the valve. A typical operation of the valve is with a pulse length of 350 μs, at an applied voltage, across the control wires, of 200 Volts, and a repetition rate of 10 Hz. The time average pressure of the source chamber under these conditions is approximately 5×10^{-4} mbar. The valve is designed such that a poppet is translated by a solenoid. In the closed position of the valve the poppet is pushed into the valve aperture. On application of a voltage pulse to the solenoid the poppet is moved such that the valve opens, the poppet then relaxes back to its closed position. At the top of Figure (2.4) we can see the aperture in the valve body and the poppet below it. The valve body and coil assembly are screwed together when the valve is operating. The valve is connected to a high pressure gas line. This line is connected to a gas cylinder containing a mixture of argon and 2%

sulphur hexafluoride gas. Regulators are used to control the gas pressure supplied to the valve. The valve backing pressure is normally 5 Bar, however we have tested the source's performance over a range of 1 to 5 Bar.

There are a number of valve parameter that can be changed to optimise the gas pulses it produces. These include the backing pressure, the pulse length, the applied voltage, and the spring tension applied to the poppet. This can be changed by altering the tension on the coil assembly and valve body screw connection. These parameters can be manipulated "live" so that the gas signal may be optimised quickly. The valve position relative to the skimmer is also adjustable. The valve is located on top of the valve mount. The valve mount can be translated in the (y, z) plane "live" and in the x-axis, although this adjustment can not be performed while the source chamber is under vacuum. The coordinate system is defined such that the vertical axis of the machine is the x-axis, and the horizontal axes are the (y, z), see Figure (2.1). The valve-skimmer distance is adjusted for the maximum YbF signal, and the distance is normally approximately 10 cm. Figure (2.5) shows a close up of the supersonic source design. At the bottom of the figure we find the translation vacuum flange with the valve mount through it. On top of the valve mount and valve sits the Yb target, which is described later in the text. The skimmer which is not should in the diagram is located above the valve on the centreline of the experiment. The skimmer is mounted on a plate on the top flange of the source chamber just below the gate valve and is located on the centreline of the machine. The skimmer aperture was 2 mm in diameter and was chosen because the molecular beam produced had the correct solid angle for our detector.

The system described above produces supersonically cooled pulses of Ar+SF_6 carrier gas which are emitted from the valve, travel through the skimmer and then through the length of the experiment. To measure these carrier gas pulses we use a (Beam Dynamics) fast ionization gauge (FIG) with a 5 μs time resolution. To sensitively align the FIG to the centreline of the experiment we placed an aperture over its active element. We then centre the hole of the aperture over the centreline of the experiment. The square aperture was roughly 5 by 5 mm. To make sure this alignment was correct we shone a Helium-Neon laser beam down the centreline of the machine and adjusted the FIG's placement appropriately[1]. The FIG is mostly used as a diagnostic tool which enables us to align the molecular beam to the centreline of the machine, by finely adjust the valve position so that the gas pulses, measured by the FIG, are maximised. We also record carrier gas time of flight

[1]We occasionally use this technique to check the alignment of the valve aperture to the skimmer and FIG aperture.

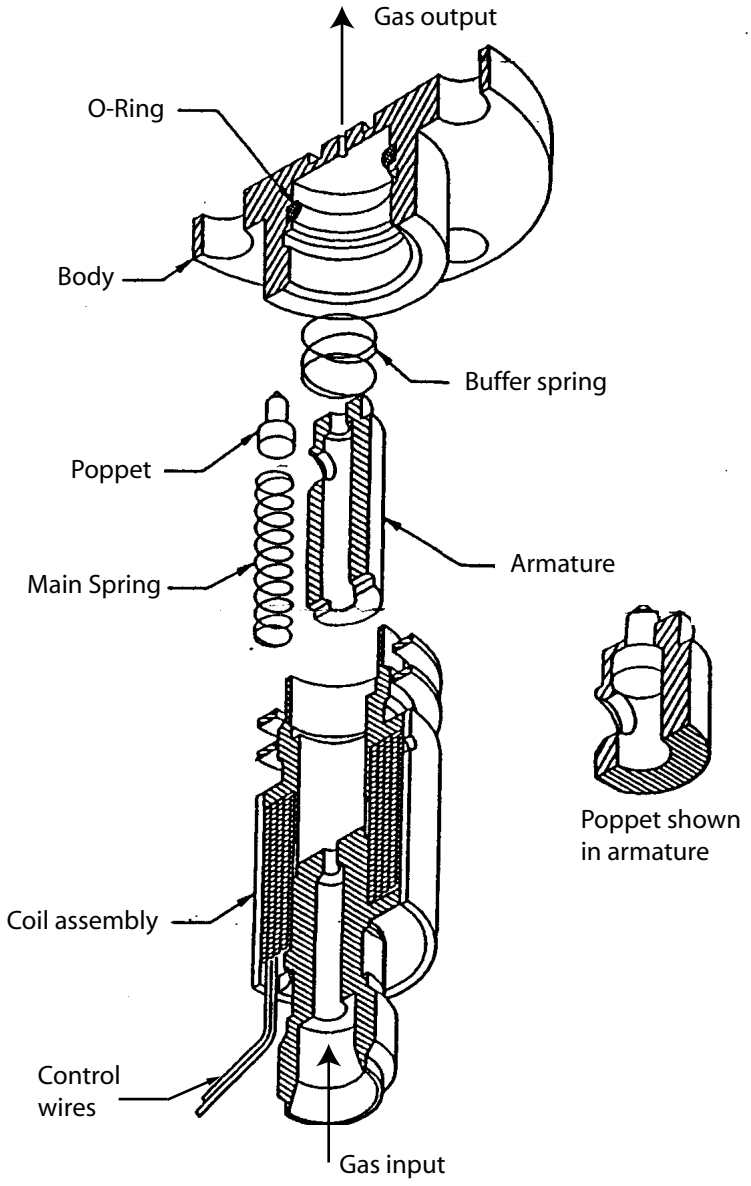

Figure 2.4: This shows the design of the valve we use in the supersonic source. Copyright Parker Hannifin Corporation.

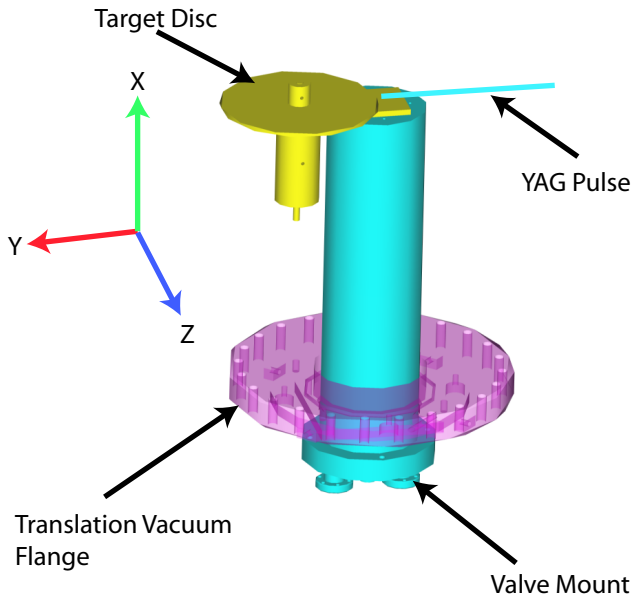

Figure 2.5: A side view close up of the source valve mount and the Yb target disc.

profiles, with the FIG, using the same system that records the YbF time of flight profiles. This allows us to switch between detectors easily.

Once the valve is aligned properly to the machine we are in a position to produce a YbF molecular beam. This is achieved by laser ablation of a Yb metal disc target, shown in Figure (2.5). The Yb target is hit by a high energy pulse of YAG laser light. This YAG pulse, at 1064 nm, is far from resonant with the 552 nm A-X transition in YbF. The effect of the YAG light pulse on the surface of the Yb target is to ablate some Yb into a plasma. The YAG laser pulses are approximately 6 ns in duration, with energies up to 35 mJ. We have used a variety of YAG lasers with repetition rates varying from 10 Hz to 100 Hz[2]. Most of the data was taken at a 20 Hz repetition rate. The peak pulse power of the YAG laser can be adjusted by varying the delay between the flash lamps firing and the Q-switch opening which are both controlled by the control computer.

The target is positioned such that the Yb gas can be entrained into the carrier gas pulse. To produce a YbF molecular beam the valve is pulsed open releasing a pulse of carrier gas. The YAG laser is then fired at the Yb target to produce a Yb plume that is entrained into the carrier gas pulse. A reaction takes place between the Yb and the SF_6 creating YbF. This equilibrates with the carrier gas which is su-

[2]It should be noted that the 100 Hz Quantel Brilliant YAG laser could not provide the shot to shot stability required for the experiment.

personically cooling. A cold beam of YbF molecules travelling at supersonic speeds is produced which travels through the experiment. The YbF beam is measured by laser induced fluorescence (LIF) which is detected by a photomultiplier tube (PMT) connected via an amplifier to the control computer. See Figure (1.4). The PMT is situated at the top of the experiment and is operated in current mode, gated by the computer in 2 μs bins. This enables us to measure YbF time of flight profiles which provide the main signal for the experiment. The PMT amplifier is covered in foil to shield the amplifier.

The initial design of the Yb target was a piece of Yb hammered into an aluminum metal block. This block was attached to the top of the valve mount positioned approximately 1 to 2 mm away from the valve aperture. This target design worked well; however, its major drawback was that after firing the YAG laser at it over a period of about two days, the Yb surface would become coated with a black material[3]. After this, the target's surface would need to be filed down and cleaned to renew the YbF signal. This required that the vacuum chamber be let up to air, the target removed, cleaned and returned and the vacuum recovered. This limited our operational time. To eliminate the problem a rotatable disc target was designed and built, see Figure (2.5). The target assembly attaches to the valve mount and the target disc can be rotated in the vacuum. The target disc is connected to a rotation vacuum feedthrough via a length adjustable drive shaft and a gear assembly. This enables the target spot to be changed by rotating the disc and increases the time between target cleaning. We normally file and clean this target approximately once every two to three weeks. We use a lathe to skim the target surface ensuring a smooth and round finish.

The target disc is made from stainless steel and Yb, in the form of home-made rolled strips, which are glued to the disc edge using Torr Seal. The position of the Yb disc edge relative to the valve aperture can be adjusted in the plane of the valve surface. The height of the target disc with respect to the valve surface can also be adjusted. These adjustments were found to be important for optimising the gas pulse signal. The optimal location of the target disc was approximately 2 mm above the valve surface sitting on a metal plate and 2 mm horizontally away from the valve aperture.

[3]The source of this material has not been rigourously investigated. However, it is most probably sulphur from the carrier gas.

Parameter set	Parameter
Valve	Repetition rate
	Voltage
	Pulse length
	Backing pressure
	Poppet Tension
	Position
YAG laser	Repetition rate
	Flash lamp to Q-switch delay
	Valve to Q-switch delay
	Missed shots
	Spot position
	Spot focus
	Yb target position
	Yb target rotation

Table 2.1: Source Parameter space

2.4 Characterisation

In this section I characterise the YbF molecular beam and explain how we optimise this beam for maximum signal. First I explain the procedure for producing carrier gas pulses, and then how we create the YbF beam and how this beam is optimised for maximum signal. I then explain what the important source parameters are to obtain a stable and intense YbF signal over longer periods of time.

To generate a strong YbF beam we first need to create intense supersonic carrier gas measured using the FIG. To optimise this beam we adjust many parameters, listed in Table (2.1). The transverse position of the valve with respect to the skimmer is the first parameter to be adjusted to obtain gas pulses. While the valve is pulsing we may move it with screws on the outside of the source chamber. These push on a translation vacuum flange which holds the valve mount, see Figure (2.5). The valve-skimmer distance is normally set to around 10 cm and can also be adjusted by moving the valve mount. Once a carrier gas signal is observed on the FIG it can be optimised by varying the other parameters. When varying the poppet tension it is important to concomitantly change the valve voltage. Our procedure is to make a small adjustment to the poppet tension and then adjust the valve voltage to maximise the signal. This is repeated for different tensions and the optimal signal can be found. A typical time of flight signal after optimisation

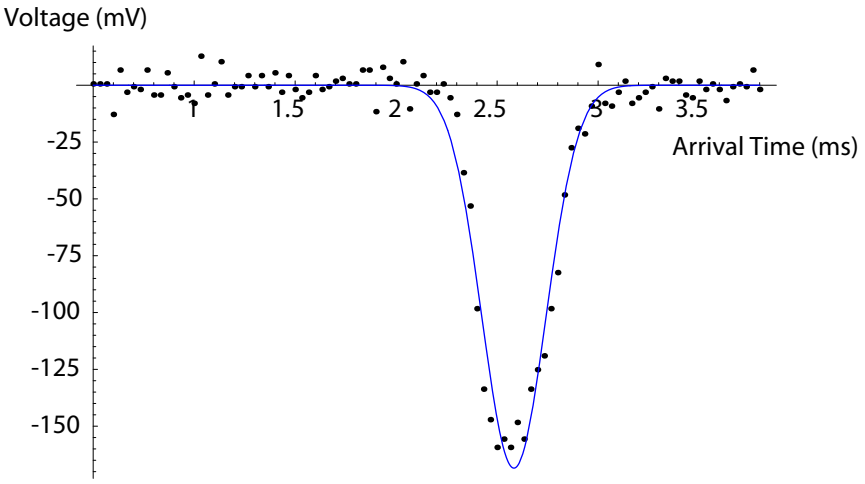

Figure 2.6: Example TOF signal. The valve pulse length was 350 μs, valve voltage 140 V. The time axis shows the gas arrive time after the valve pulse. The blue curve is a Gaussian fit to the data to guide the eye.

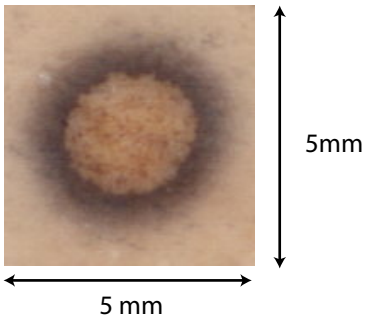

Figure 2.7: YAG profile picture. The pulse energy was approximately 45 mJ from a Spectron YAG laser.

is shown in Figure (2.6). The x-axis shows the arrival time of the molecules in ms after the valve pulse. The y-axis shows the voltage recorded by the FIG. The solid curve is a Gaussian fit to the data to guide the eye. Once the gas pulses have been optimised we are ready to produce YbF.

The YAG laser is turned on. To check the laser beam intensity profile we flash the laser onto a piece of burn paper, Figure (2.7) shows an example of the result. If the YAG beam profile is not of a similar form to Figure (2.7) the laser may need to be realigned. Next the beam is steered onto the Yb target by eye[4]. The target flashes with a blue colour, through the goggles, when the YAG beam hits it. When

[4]Looking through some laser goggles!

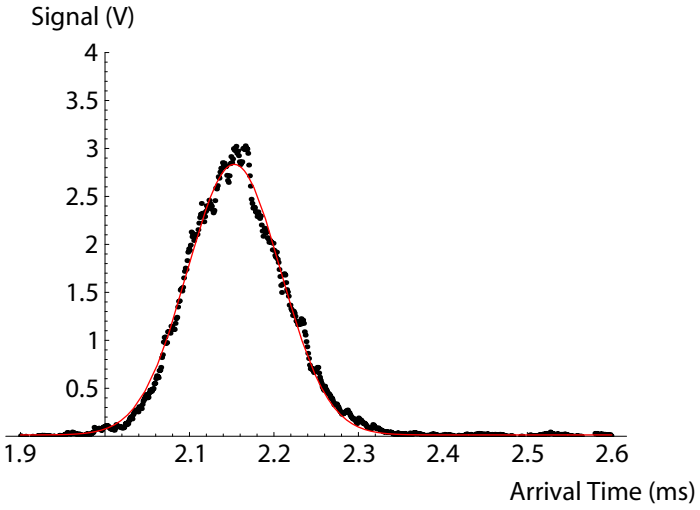

Figure 2.8: Example YbF Pulse. The time axis shows the delay between the valve pulse and the gas arrive time. The y-axis plots the YbF signal. The red curve is a Gaussian time of flight fit.

aligning the YAG laser to the Yb target it is necessary to have the valve pulsing, otherwise the valve aperture gets obstructed with Yb. To measure the YbF beam we use the LIF signal, detected by the PMT, which naturally requires the probe laser to emit light at the correct frequency, see Section (3.3). The YbF signal is then optimised by tuning the YAG parameters listed in Table (2.1). Normally the position of the YAG spot on the target is adjusted first, and the target rotated to a fresh spot of Yb. A typical YbF pulse is shown in Figure (2.8). If one compares the mean arrival time of the YbF in this figure with the mean arrival time of the carrier gas, Figure (2.6), we find that the YbF molecules arrive sightly earlier. This indicates that the YbF molecules do not completely thermalise with the carrier gas and do not cool to the same temperature. The solid line in Figure (2.8) is a Gaussian fit described below.

It is possible to calculate the translational temperature of the YbF molecules from the time of flight profile. Fitting the Gaussian

$$F(t) = N + \frac{Q}{\sqrt{2\pi W}} Exp\left(\left(\frac{t - t_0}{W}\right)^2\right) \tag{2.9}$$

to the time of flight data, and comparing this to equation (2.8) we find a translational temperature

$$T = \frac{(WL)^2 M}{k_B t_0}, \tag{2.10}$$

where L is the distance the pulse travelled: 1.3 m. The parameters of the fit are the

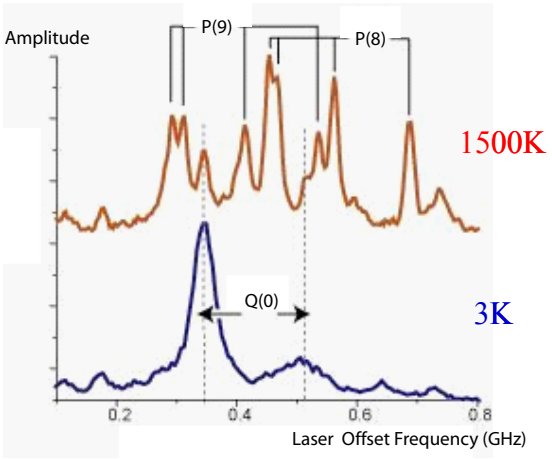

Figure 2.9: Example YbF spectrum comparing the oven and supersonic sources.

background N, the peak height Q, and the width W. For the data shown in Figure (2.8) we find a translational temperature of 5.6 K. The rotational temperature can be found to be of the same order as the translational temperature from measuring relative intensities of spectra lines [72]. It is possible to compute the mean velocity from the fit which for this data was 604 m.s^{-1}. This measure of the velocity however, does not take into account that the gas accelerates through the valve until the skimmer region. We can also see from Figure (2.8) that the Gaussian form describes the YbF pulse reasonably well. The departures from the Gaussian lineshape are probably due to temperature differences within the molecular pulse.

Another signal can also be extracted from the time of flight data. For this each time of flight profile is integrated to form one point of fluorescence data. This raw integrated signal, in units of Vμs, is used extensively in our experiment because it is proportional to the YbF fluorescence. The YbF spectrum is obtained, by scanning the probe laser frequency and integrating the time of flight signal at each laser frequency. Figure (2.9) shows the YbF spectrum around the Q(0) line of interest in the experiment. This figure also shows a spectrum taken with the old oven source at a temperature of 1500 K. The oven source spectrum has many overlapping rotational lines because the molecules are produced hot. The supersonic source spectrum by contrast has far fewer rotational lines because of the supersonic cooling, explained in Section (2.2).

After the position of the YAG laser spot has been aligned to the target for the maximum signal other parameters can be adjusted. An important parameter to set is the timing delay between the firing of the YAG flash lamps and the Q-switch opening. This sets the YAG laser pulse energy which decrease as the delay

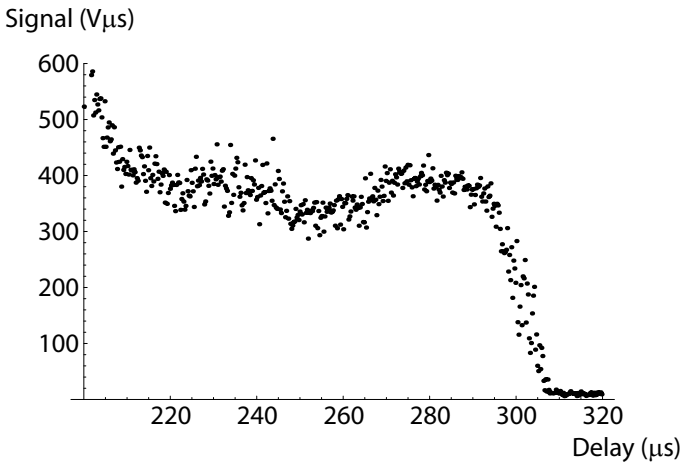

Figure 2.10: Flash to Q-switch delay scan. The YAG laser pulse energy decreases with longer flash to Q-switch delay. Each point in the scan is an integrate time of flight profile. The x-axis is the delay in μs, starting at 200μs. The y-axis is in units of Vμs.

increases. The parameter is referred to as the flash to Q-switch delay and can be scanned by the control computer. There are several interesting features in the pulse energy scan shown in Figure (2.10). At the beginning of the scan, between 200 and 220 μs, the signal decays from a maximum. This can be attributed to the target conditions changing due to the target heating up from the high YAG pulse energy. The background pressure in the source chamber may also contribute to this decay. The normal background pressure of the source chamber with the valve closed is below 1×10^{-7} mbar. However, this increases to around 5×10^{-4} mbar when the valve starts pulsing. As the background pressure increases in the source chamber more YbF is scattered out of the molecular beam. After 220 μs in the scan the signal plateaus and after 280 μs the signal drops sharply to zero. The signal drops because the YAG pulse energy is reduced to below the amount necessary to produce more YbF. From the curve we choose a value of the delay on the plateau region to use in the experiment.

Once the flash to Q-switch delay has been set we scan the other parameters to optimise the YbF pulses. After optimising the YAG laser parameters we optimise the YbF pulses with respect to the valve parameters. The optimum valve parameters for the FIG pulses do not necessarily correspond to the optimal parameters for the YbF signal. As a final stage of optimisation the valve voltage and poppet tension are often adjusted again.

2.5 Source Stability

The optimisation of the source parameters above, describes a procedure for maximising the YbF pulses. This procedure takes little notice of the long term signal stability. To perform a sensitive EDM experiment the YbF signal stability is also very important.

We would like the EDM measurement to be limited only by the shot noise of the photon counts. For a typical signal the peak of the time of flight profile is 5 V which converts to approximately 700 $V\mu s$. The calibration from $V\mu s$ to photon number in the pulse is 0.148 $(V\mu s)$/photon number. From this we can calculate that the shot noise from the 5 V TOF peak corresponds to a 1.5% variation in the signal. Once the source parameters have been set the temperature of the signal, proportional to the width of the time of flight profile, stays largely constant. Therefore, we would like our shot-to-shot YbF signal variation for a 5 V time of flight peak to be of order 1.5%.

To achieve this source stability it is important that the carrier gas pulse variation meets the required level. To measure this we compared an optimised FIG signal to a typical YbF signal and found that the shot-to-shot variation of the carrier gas pulses was less than the statistical noise of the fluorescence signal. This means that the carrier gas pulse variation does not limit the experiment.

The level of stability we require also puts constraints on the YAG laser pulse energy variation. However, for a typical YAG laser, which is well aligned, the pulse energy variation is not large enough to limit the EDM experiment. To measure the YAG pulse variation we use a fast photodiode. To avoid saturating the photodiode we fire the YAG onto a polystyrene beam dump which scatters the light. The photodiode is pointed at the scattered YAG light and its signal measured on an oscilloscope. If the noise measured by the photodiode is more than the specification of the laser the YAG can be realigned which often fixes the problem.

The stability of the supersonic source also depends on the source parameters chosen. Because of the large parameter space it is hard to find the optimum parameter set for long term stability. This problem is compounded by the fact that the source stability also depends upon the target history. This history makes it difficult to constrain the parameters and find the optimal set. We have therefore adopted an empirical process for optimisation of the source. Using this method we have discovered that the long term stability of the YbF signal depends on the YAG laser beam spot size, shape, and power as well as the other source parameters. This has been determined by a systematic investigation of the effect of the focusing of

the YAG spot, on the target, on the YbF signal strength and stability.

The focus of the beam at the target is important. If the beam is very tightly focused at the target then the signal from a new spot displays its typical behaviour of increasing, decreasing and then increasing again until the noise increases to above 3 or 4 shot noise. For optimised conditions this behaviour happens over the course of 30-40 minutes, however, for a tightly focused beam this happens over 30-40 seconds. As the focus is relaxed a stable signal can be found, above this spot size the signal becomes unstable again. It is also important that the laser beam is not focused in free space or on the source chamber window[5].

The stability also depends on the target spot, some spots give better signal to noise then others. After the target disc has been rotated through 360 degrees and most of is surface covered in holes drilled by the YAG laser, it is taken from the chamber and skimmed. We skim the target on a lathe 100 μm at a time. This removes most of the black deposited material and smoothes the surface. After skimming we clean the target in an ultra-sonic bath of isopropanol or acetone. The target is then put back in the experiment and a good signal can be expected.

By adjusting the parameters of the source it is possible to reduce the signal variation to below 1.5 times shot noise over several hours of data collection. This stability is also largely reproducible every day the experiment is run; however, it takes a long time to "home in on" the stable parameter set and the parameters change unpredictably for different YAG lasers.

[5]We have unintentionally drilled holes in a window and a lens.

Chapter 3

Manipulating the Molecules

In the first section of this chapter, I briefly describe the structure of YbF. In Section (3.2) I describe how we control the molecules state using two different techniques: Raman and pulsed rf excitation. I then describe in Section (3.3) the laser system used and the implementation of the Raman technique, in Section (3.4). Following this I characterise the performance of this Raman method, in Section (3.5). I then discuss the implementation of the pulsed rf system, and go on to characterise its performance, in Sections (3.6) and (3.7) respectively. Finally in Section (3.8), I discuss the measurement of the Stark shift of the first electronically excited state in YbF.

3.1 The Structure of YbF

In YbF, the Ytterbium atom, $[Xe]4f^{14}6s^2$, donates one of its 6s electrons to the Fluorine atom, $1s^22s^22p^5$, which has one electron missing from its 2p level. This forms the YbF radical with an ionically bound closed shell core and a single valence electron. We use the most abundant isotopomer ^{174}YbF, its structure is relatively simple since ^{174}Yb has zero nuclear spin. In the ro-vibrational state of the electronic ground state $X^2\Sigma^2_{1/2}(\nu = 0, N = 0)$, the Fluoride's nuclear spin 1/2 couples with the single valence electron spin 1/2 to form singlet and triplet hyperfine levels F=0 and F=1. The hyperfine splitting is approximately 170 MHz. Figure (3.1) shows these ground state hyperfine levels $\mid F, m_F\rangle$ as, $\mid 0, 0\rangle$, $\mid 1, -1\rangle$, $\mid 1, 0\rangle$, and $\mid 1, 1\rangle$, together with the first electronically excited $A^2\Pi_{1/2}(\nu = 0, N = 0)$ state in the presence of an electric field applied along the z-axis. The $\mid X^2\Sigma^2_{1/2}\rangle$ and $\mid A^2\Pi_{1/2}\rangle$ levels are connected by a Q(0) optical transition at approximately 542.811 THz or 552 nm, which is used for pumping and probing the molecules. The $\mid A^2\Pi_{1/2}\rangle$ state hyperfine splitting is only $\sim$3 MHz, which is small enough that we normally

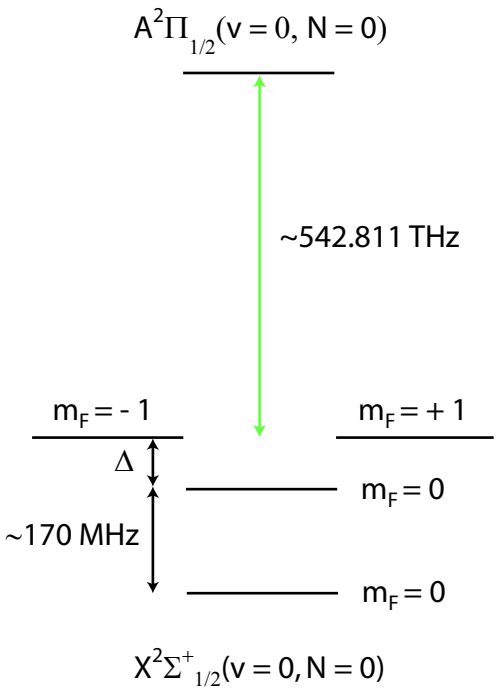

Figure 3.1: YbF energy level diagram showing the spectral lines used in the experiment. Δ is the Stark splitting of the $|\ 1, \pm 1\rangle$ to $|\ 1, 0\rangle$ states. The Stark shift is due to an externally applied electric field along the z-axis.

treat it as a single level. For further details on the structural properties of YbF see [14, 29, 64, 63, 65, 76].

When an electric field is applied to the molecules their energy levels acquire a Stark shift. The ground state energy is shifted along with an additional splitting of the hyperfine F=0 to F=1 splitting [64, 76], the degeneracy of the $|\ 1, 0\rangle$ and $|\ 1, \pm 1\rangle$ states is also lifted. This later splitting is due to the tensor part of the hyperfine interaction and is indicated in Figure (3.1) by Δ. Figure (3.2) shows both the Stark shifts for the $|\ 1, \pm 1\rangle$ to $|\ 0, 0\rangle$ splitting and the $|\ 1, \pm 1\rangle$ to $|\ 1, 0\rangle$ splitting [76], the x-axis of both graphs show the applied electric field in kV/cm. The Stark shift of the excited A-state has been measured during my PhD and is discussed in Section (3.8).

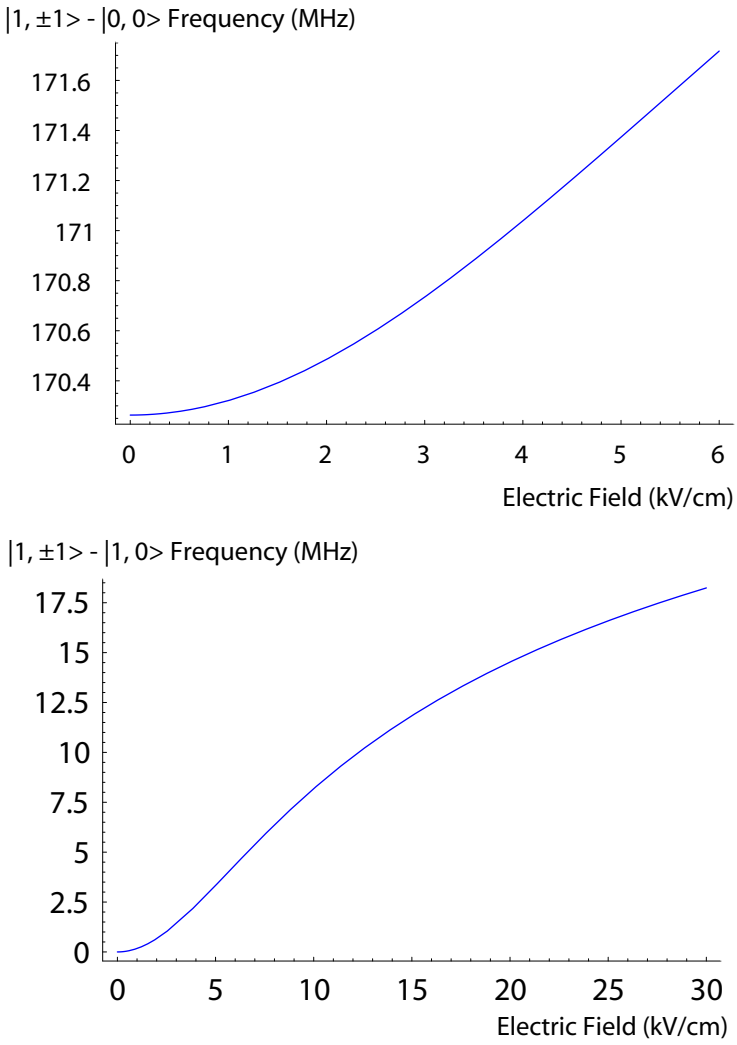

Figure 3.2: Stark Shift of the F=1 to F=0 transition and $|\ 1, \pm 1\rangle$ to $|\ 1, 0\rangle$ splitting.

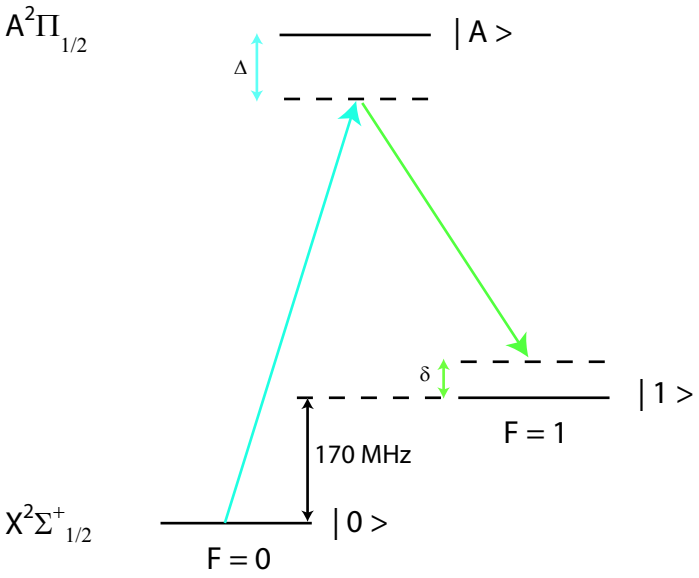

Figure 3.3: Simplified level scheme for Raman transitions.

3.2 Raman and Rf Excitation

Two methods are used to control the population and coherence between the hyperfine levels of the ground state. The simplest method is to drive radio frequency (rf) transitions with oscillating magnetic fields, see Section (3.6) [29, 53, 54]. The alternative method is to drive Raman transitions using two laser beams. The Raman technique is currently used in the experiment and was implemented during the later part of my PhD. It is the main topic of this section.

We first pump on the $F = 1$ state reducing its population. As discussed in Section (1.3.2), the pumping is not 100% efficient, however, for our purposes we assume that it is. After the molecules have been pumped out of the $F = 1$ state they pass through the Raman beams and undergo the transition to the $F = 1$ state from the $F = 0$ state. I will label the hyperfine states as $\mid 0\rangle$ and $\mid 1\rangle$ for $F = 0$ and $F = 1$ respectively. To connect the hyperfine levels we use two laser beams. These laser beam connect the levels via an intermediate state $\mid A^2\Pi_{1/2}\rangle$, which will be labelled $\mid A\rangle$ for bravity. The Raman transitions are driven in regions where an electric field is applied, see Section (3.4). The electric field provides a nature quantization axis since it polarises the molecules strongly.

The Raman laser frequencies are chosen to be well detuned from the signal photon Q(0) transition, Δ in Figure (3.3). This avoids losses into other molecular states by spontaneous emission. Figure (3.3) shows a simplified level structure for the ground state and $\mid A\rangle$ state. In the diagram we see the two Raman lasers

connecting the F=0 state to the F=1 state via the intermediate $\mid A\rangle$ state. The first laser connecting the F=0 state to the intermediate $\mid A\rangle$ state is detuned by Δ. The second laser couples the $\mid A\rangle$ state to the F=1 state. The detuning in this case is $\Delta - \delta$, where δ is very small in comparison with Δ.

I consider this three level system under the perturbation of the two co-propagating laser fields,

$$E = A_{L1}\cos\left(kx - \omega_{L1}t\right) + A_{L2}\cos\left(kx - \omega_{L2}t\right) \tag{3.1}$$

where the subscripts L1 and L2 indicate the laser beam creating the radiation. For now we do not worry about the polarization of the light, though this is important when considering which of the F=1 magnetic sublevels we are coupling. We require one of the beams to be polarised along the x-axis of the experiment and the other beam to be polarised along the z-axis. Misalignment of the polarisations of the beams causes reduced transition efficiencies.

To uncover the essential physics, it is enough to treat the interaction by lowest order perturbation theory. For this three level system, the total wavefunction is

$$\Psi(x,t) = C_0(t) \mid 0(x,t)\rangle + C_A(t) \mid A(x,t)\rangle + C_1(t) \mid 1(x,t)\rangle \tag{3.2}$$

where C_0, C_A, and C_1 are the state coefficients. Each eigenstate of the wavefunction can be expanded into a product state with a time dependent part and a space dependent part,

$$\mid j(x,t)\rangle = \mid j(x)\rangle e^{-iE_j t/\hbar} \tag{3.3}$$

where j is the state label. Since the detuning Δ is large there will be little spontaneous emission from the $\mid A\rangle$ state. Therefore, I neglect the complex nature of E_A that in a more comprehensive treatment would include a term $i\gamma$ which takes into account the spontaneous emission.

The Hamiltonian for the system has two parts $H = H_A + H_I$, where H_A is the Hamiltonian of the molecule in the static electric field, and H_I is the Hamiltonian for the molecules interaction with the light fields. By substitution of (3.2) and (3.3) into the Schrödinger equation we obtain a differential equation for the state coefficients which simplifies to,

$$H_I\left(C_0(t) \mid 0(x,t)\rangle + C_A(t) \mid A(x,t)\rangle + C_1(t) \mid 1(x,t)\rangle\right) = i\hbar\left(\dot{C}_0 + \dot{C}_A + \dot{C}_1\right) \tag{3.4}$$

where the raised dots indicate we are taking the first differential with time. To separate (3.4) and find the dynamics of the coefficient C_0 we multiply on the left

by $\langle 0(r,t) \mid$ and integrate over all space, leaving

$$C_0\langle 0(r,t) \mid H_I \mid 0(r,t)\rangle + C_A\langle 0(r,t) \mid H_I \mid A(r,t)\rangle + C_0\langle 0(r,t) \mid H_I \mid 1(r,t)\rangle = i\hbar\dot{C}_0 e^{-iE_0 t/\hbar}. \quad (3.5)$$

To evaluate the matrix elements in (3.5) we make the electric dipole approximation and approximate the electric field over the molecules as being constant in space:

$$\left(C_A e^{-i\omega_{0A}t}\langle 0(x) \mid ex \mid A(x)\rangle + C_1 e^{-i\omega_{01}t}\langle 0(x) \mid ex \mid 1(x)\rangle\right) \times \left(A_{L1}\cos\omega_{L1}t + A_{L2}\cos\omega_{L2}t\right) = i\hbar\dot{C}_0. \quad (3.6)$$

In (3.6) the eigenstates are now only the space dependent parts, also ω_{0A} and ω_{01} are the transition frequencies between $\mid 0\rangle$ to $\mid A\rangle$ and $\mid 0\rangle$ to $\mid 1\rangle$ respectively. Now I substitute the Rabi rates $\Omega^k_{ij} = \langle i \mid ex \mid j\rangle A_k/\hbar$ into (3.6), where the index k indicates which laser field (laser one or laser two) is interacting with the molecules causing the Rabi rate. This leaves us with,

$$C_A e^{-i\omega_{0A}t}\left(\Omega^1_{0A}\cos\omega_{L1}t + \Omega^2_{0A}\cos\omega_{L2}t\right) + C_1 e^{-i\omega_{01}t}\left(\Omega^1_{01}\cos\omega_{L1}t + \Omega^2_{01}\cos\omega_{L2}t\right) = i\dot{C}_0. \quad (3.7)$$

Following a similar procedure we may find the evolution of the coefficients C_A and C_0 with time,

$$C_0 e^{i\omega_{0A}t}\left(\Omega^1_{0A}\cos\omega_{L1}t + \Omega^2_{0A}\cos\omega_{L2}t\right) + C_1 e^{i\omega_{A1}t}\left(\Omega^1_{A1}\cos\omega_{L1}t + \Omega^2_{A1}\cos\omega_{L2}t\right) = i\dot{C}_A, \quad (3.8)$$

and

$$C_0 e^{-i\omega_{01}t}\left(\Omega^1_{01}\cos\omega_{L1}t + \Omega^2_{01}\cos\omega_{L2}t\right) + C_A e^{-i\omega_{A1}t}\left(\Omega^1_{A1}\cos\omega_{L1}t + \Omega^2_{A1}\cos\omega_{L2}t\right) = i\dot{C}_1. \quad (3.9)$$

To solve this set of coupled first-order differential equations without any further approximation is beyond my mathematical skill and also beyond the scope of this thesis. However, it is possible to solve these equations in a power series of the Rabi rates provided the Rabi rates here are very small compared to ω_{0A} and ω_{A1} [44]. In this approximation a zeroth-order set of solutions, $C_0(t) = 1$, $C_A(t) = 0$, and $C_1(t) = 0$, is substituted into (3.7), (3.8), and (3.9) enabling the equations to be solved to first-order in the Rabi rates. Thus we may solve (3.8) as follows:

$$i\dot{C}_A = \frac{\Omega^1_{0A}}{2}\left(e^{i(\omega_{0A}+\omega_{L1})t} + e^{i(\omega_{0A}-\omega_{L1})t}\right) + \frac{\Omega^2_{0A}}{2}\left(e^{i(\omega_{0A}+\omega_{L2})t} + e^{i(\omega_{0A}-\omega_{L2})t}\right), \quad (3.10)$$

integrating over time and substituting the initial conditions $C_0(0) = 1$, $C_A(0) = 0$, and $C_1(0) = 0$ gives,

$$C_A(t) = \frac{\Omega_{0A}^1}{2}\left(\frac{1-e^{i(\omega_{0A}+\omega_{L1})t}}{\omega_{0A}+\omega_{L1}} + \frac{1-e^{i(\omega_{0A}-\omega_{L1})t}}{\omega_{0A}-\omega_{L1}}\right) + \frac{\Omega_{0A}^2}{2}\left(\frac{1-e^{i(\omega_{0A}+\omega_{L2})t}}{\omega_{0A}+\omega_{L2}} + \frac{1-e^{i(\omega_{0A}-\omega_{L2})t}}{\omega_{0A}-\omega_{L2}}\right). \quad (3.11)$$

This can be simplified by making the rotating wave approximation which eliminates the terms furthest from resonance. We also assume that the energy separation of the $\mid 0\rangle$ and $\mid 1\rangle$ states is large compared to the linewidths of the lasers and that there is no power broadening. This avoids the interference effects from laser one driving the transition that laser two is tuned too, and visa-versa. With these approximations we find,

$$C_A(t) = -\frac{\Omega_{0A}^1}{2\Delta}\left(1-e^{-i\Delta t}\right) \quad (3.12)$$

where $\Delta = \omega_{L1} - \omega_{0A}$ is the detuning of the first laser from resonance with ω_{0A}. Equation (3.12) is precisely what one finds for a single photon transition between the states $\mid 0\rangle$ and $\mid A\rangle$.

Having solved (3.8) we may substitute the solution into (3.9) and solve for $C_1(t)$. Using similar approximations as above, and considering which lasers are closest to resonance with the transitions we find that,

$$C_1(t) = \frac{\Omega_{0A}^1\Omega_{A1}^2}{4\Delta}\left(\frac{1-e^{i\delta t}}{\delta} - \frac{1-e^{i(\Delta+\delta)t}}{\Delta+\delta}\right) \quad (3.13)$$

where $\delta = \omega_{L2} - \omega_{L1} + \omega_{0A} - \omega_{A1}$ is the difference between the splitting of the states $\mid 0\rangle$ to $\mid 1\rangle$ and the frequency difference between the lasers. In order to drive the Raman transition on resonance between $\mid 0\rangle$ and $\mid 1\rangle$ we require $\delta = 0$. One also recognises that $\mid \Delta \mid \gg \mid \delta \mid$, implying that we may simplify (3.13) to,

$$C_1(t) = \frac{\Omega_{0A}^1\Omega_{A1}^2}{4\Delta}\left(\frac{1-e^{i\delta t}}{\delta}\right). \quad (3.14)$$

This means that the probability with time of populating the $\mid 1\rangle$ state is,

$$\mid C_1(t) \mid^2 = \frac{\left(\Omega_{0A}^1\Omega_{A1}^2\right)^2}{2\Delta^2\delta^2}\sin^2\left(\frac{\delta t}{2}\right). \quad (3.15)$$

Equation (3.15) is of the same form as that of a single photon transition [44] if we substitute an effective Rabi rate $\Omega_{eff} = \frac{\Omega_{0A}\Omega_{A1}}{2\Delta}$ for the transition from $\mid 0\rangle$ to $\mid 1\rangle$. On inspection of equation (3.15) one finds that as the power of the laser beams is increased the population in state $\mid 1\rangle$ increases with seemingly no limit. This is because we have not taken into account the effects of power broadening

which introduces Rabi oscillations as the laser beam powers are increased. Indeed as the Rabi rates are increased and become comparable with ω_{0A} and ω_{A1} perturbation theory brakes down. A more comprehensive treatment would find that the maximum population in state $\mid 1\rangle$ is met at time t_π when $\Omega_{eff}t_\pi = \pi$. This is called a π pulse.

In [20] a similar treatment of Raman transitions can be found in Appendix E[1]. In [20] the interactions of the two lasers with an atom are treated separately, however the resulting equation for the population of the $\mid 1\rangle$ state is the same as (3.15). The method I have used to solve the coupled equations (3.7),(3.8), and (3.9) can be found in [20, 44]. Also in these books, as well as in [80], most of the approximations I have used are explained in more depth. For an in-depth account of the theory of atomic and molecular coherent excitation see [69].

In the above calculation I have neglected the effects of spontaneous emission. This approximation is valid when the detuning frequency Δ is much greater than the spontaneous emission rate, $\mid \Delta \mid \gg \Gamma$. For a π pulse it is possible to estimate the number of spontaneously emitted photons to be [20],

$$R_{scat}t_\pi \simeq \frac{\Gamma\Omega_{0A}}{4\Delta^2}\frac{\pi}{\Omega_{eff}} \simeq \frac{\pi\Gamma}{2 \mid \Delta \mid}\frac{\Omega_{0A}}{\Omega_{A1}}. \tag{3.16}$$

For the case where $\mid \Delta \mid \gg \Gamma$ the number of spontaneously emitted photons is very small. In the experiment we normally set the detuning, Δ, to be approximately 100 linewidths from the $\mid A\rangle$ state, then since $\Omega_{0A}/\Omega_{A1} \simeq 1$, the number of spontaneously emitted photons from $\mid A\rangle$ is approximately 1/100 photons, which is negligible.

I have derived the above results using perturbation theory for the case where $\Delta \gg \Gamma$ and $\delta \ll \Delta$. When the Raman transition is very close to resonance, $\delta \simeq 0$. However, it is possible to consider the system when $\delta \neq 0$. This is treated in [69], and it is relatively simple to derive the equation governing the dynamics of the coefficients of the states. Essentially we rewrite equations (3.7-3.9) in a much nicer way by making the rotating wave equation, and writing the dynamics of the coefficients as

$$\frac{d}{dt}\begin{pmatrix} C_0 \\ C_A \\ C_1 \end{pmatrix} = \begin{pmatrix} 2\Delta_{0A} & \Omega_{0A} & 0 \\ \Omega_{0A} & 0 & \Omega_{A1} \\ 0 & \Omega_{A1} & 2\Delta_{A1} \end{pmatrix}\begin{pmatrix} C_0 \\ C_A \\ C_1 \end{pmatrix}. \tag{3.17}$$

In deriving this equation some phases have been inserted into the expansion of the three-state wavefunction, changing the definition of the C coefficients. The

[1]The treatment in [20] is more concise than the derivation here.

wavefunction is written,

$$\mid \Psi(r,t)\rangle = e^{-iE_A t/\hbar}\left(C_0(t) \mid \psi_0(r)\rangle e^{i\omega_{L1}t} + C_A(t) \mid \psi_A(r)\rangle + C_1(t) \mid \psi_1(r)\rangle e^{i\omega_{L2}t}\right). \tag{3.18}$$

Equation (3.17) follows from this wavefunction, using the rotating wave approximation, and setting the Rabi rates to be real. In the equation Δ_{0A} and Δ_{A1} are the detunings of the first and second laser beams with the upper state transition frequencies respectively. When these detunings are equal, the laser frequency difference is equal to the transition frequency between the hyperfine levels.

From equation (3.17) it is possible to analytically solve the system when the detunings are equal with no further approximations. However, in the more general case, that the detunings are not equal we have to solve equation (3.17) numerically. The results of performing this calculation agree with the perturbation theory approach used here.

3.3 The Laser System

In this and the following sections I discuss the laser system needed to drive the Raman transitions.

The YbF is detected by laser induced fluorescence (LIF)[13, 53] on the Q(0) A-X transition. A PMT connected through an amplifier to the control computer records the LIF signal. To produce the required light for the Q(0) transition we use a Spectra 380D dye laser pumped by an Spectra Physics 2580 Ar^+ lasing on all visible lines. Figure (3.4) shows a schematic of the laser system. In the figure we see that the Argon ion laser pumps two dye lasers. The Coherent 699 is an auxiliary laser which is sometimes used for spectroscopy. The main Spectra dye laser is locked by a reference cavity and an iodine spectrometer, both seen to the right of the Spectra laser in the figure. The iodine lock is described later in this section. The Spectra light wavelength is measured by a wavemeter, shown in the figure. The main purpose of the laser is to produce light on the Q(0) line and to produce the light for the Raman transitions used in the experiment.

The output of the Spectra dye laser, running on fresh dye, is approximately 300 mW from 3 W of pump power. This power decreases over time as the dye gets old. However, fresh dye can be added to the old dye whilst the laser is operating to increase its life. This is especially useful when taking data for extended periods. The normal procedure for changing the dye involves flushing the laser and circulator with first methanol and then glycol. After this the new dye can be poured in. However,

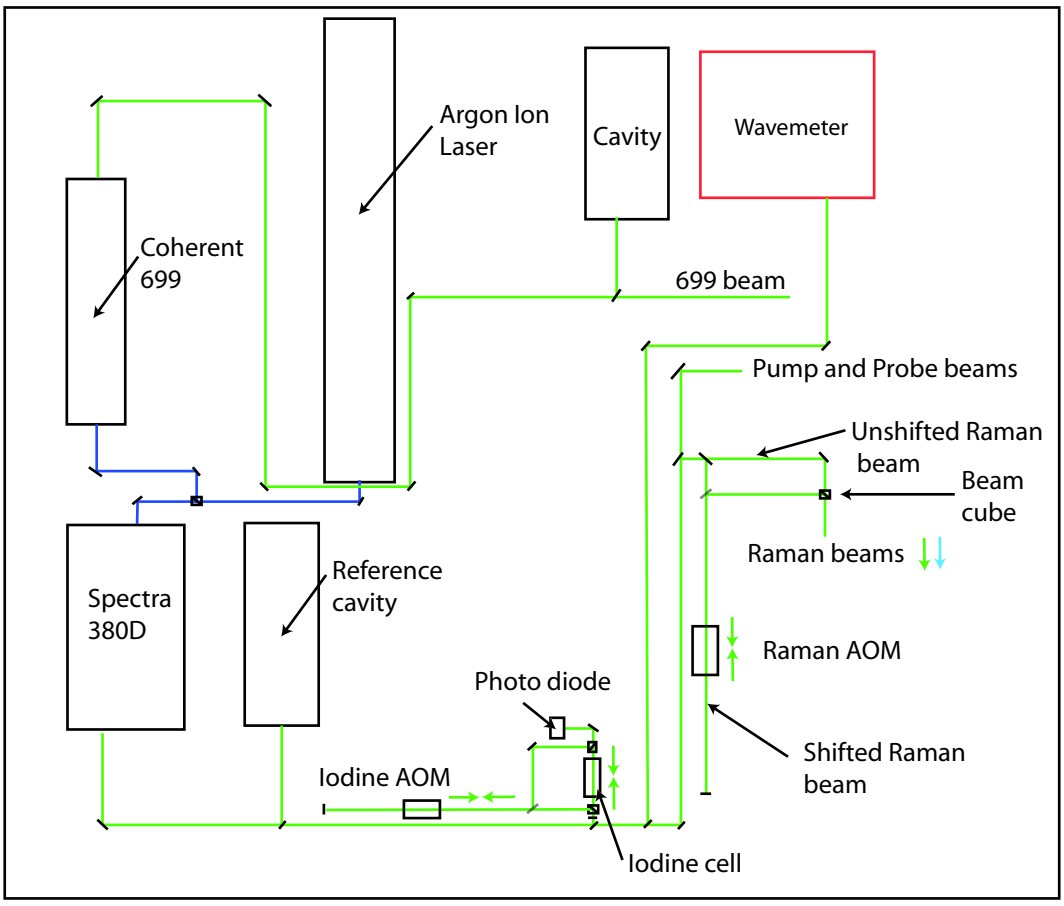

Figure 3.4: Optical Setup.

it takes around a day of running for the air bubbles in the dye to escape. During this time the laser unlocks frequently. To avoid this problem we mix up new dye and let it sit for a day. Then while the laser is operating, without flushing it first, we pour in the freshly made dye whilst draining out the same quantity of old dye. This increases the output power of the laser without it unlocking frequently, allowing the data run to continue.

To lock the laser some of the light is sent into two Febry-Perot cavities which are housed in the reference station of the laser [54], see Figure (3.4). These provide feedback from which the laser is stabilised. The absolute frequency stability of this laser system is approximately 5 MHz.hr^{-1}, which is limited by the reference cavities drifting as their temperature slowly changes. The width of the Q(0) transition is approximately 10 MHz. Therefore, to run the experiment for several hours, lasing on the Q(0) transition, it is necessary to lock the reference cavities to a more stable reference. This is provided by locking to a saturated absorption line in Iodine [13, 29, 54].

We use approximately 150 mW of the dye-laser light in the Iodine lock. Most of this power is used to pump and saturate a transition in the I_2 molecules contained within an Iodine cell. This pump beam overlaps a probe beam which goes through the cell in the opposite direction and is detected on a photodiode. To produce the saturated absorption signal the probe and pump beams must interact with the same velocity class of the molecules.

When the laser is tuned through an I_2 absorption line we measure the absorption line with sub-Doppler resolution. This allows us to lock the laser to absorption features with widths of around 20 MHz compared to the Doppler width of approximately 1 GHz. This reduces considerable the difficulty of frequency stabilising the laser. To guaranty that the laser can be locked to an Iodine line we use an acousto-optical modulator (AOM) to select a molecular velocity class that is Doppler shifted on to resonance with the laser beams at the Q(0) wavelength. This of course only works within the Doppler width of the Iodine absorption line. The AOM is set to shift the pump beam by approximately $\Delta F = 254$ MHz, and therefore the laser beams interact with molecules Doppler shifted by $\Delta F/2$. To further improve the signal to noise we apply a 100 kHz modulation to the AOM frequency which facilitates phase sensitive detection. The modulation is around 12 MHz deep and produces a signal with a dispersion type lineshape and zero crossings. These zero crossings can be shifted in frequency by adjusting the AOM frequency. This enables us to lock the laser to a zero crossing at the same frequency as the Q(0) transition in YbF. Using this lock, the laser can be stabilised to the centre of the Q(0) transition

for over ten hours[2].

3.4 Raman Implementation

The laser beams required for this Raman scheme derive from the same Spectra Physics 380D dye laser that provides the pump and probe.

The Spectra laser light is split with beams going to the reference cavity, the Iodine cell, the wavemeter, and the experiment, see Figure (3.4). The beam going to the experiment is split again one beam for pump and probe and another for the Raman setup. The Raman beam is again split with one part being double passed through an AOM and the other going through a polarising beam splitter (beam cube). The Raman beam that goes through the AOM is blue shifted by around 170 MHz, and is referred to as the shifted beam. The AOM is driven by a HP8657A synthesizer which is controlled by the control computer using a GPIB connection. The shifted and unshifted Raman beams are combined on the beam cube.

It is important that the beams are well overlapped on the beam cube and parallel going to the experiment. The two overlapped beams go through a telescope lens system expanding them to around 5 cm horizontally and 1 cm vertically. An aperture then transmits only the centre section of around 7 mm horizontally by 3 mm vertically in order to give the light a roughly constant intensity profile. Finally the beams pass through a laser port in the vacuum chamber to interact with the molecules.

To control the detunings, Δ, of the beams from the $|\, A^2\Pi_{1/2}\rangle$ state we drive the transitions in a region of electric field, which Stark shifts the molecular A-X interval. A further small detuning of the shifted Raman beam can be controlled by altering the AOM frequency. In this way both the detunings Δ and δ, of equation (3.15) can be finely controlled to optimise the transition efficiency while reducing the spontaneous emission from the $|\, A^2\Pi_{1/2}\rangle$ state.

The electric field setup is described fully in Section (4.2.2). To summarise, the field plates are split into three sections, as shown in Figure (3.5b). Figure (3.5b) also shows the rf loops, and the positions relative to the field plates that the Raman beams pass. The electric field plates support rods are also shown: the rest of the support structure is described in full in the next chapter. Figure (3.5a) is discuss later in this section. There are two Raman transition regions in the experiment one near the pump region and the other near the detection region,

[2]This largely depends upon how well the laser has been tuned prior to locking.

separated by approximately one metre. Each Raman transition region has a set of two electric field plates, roughly 8 cm long, 6 cm wide, and 2 cm thick. The plates are separated by a distance of approximately 1.15 cm. The field plates in the Raman transition regions are called the guard plates. The other pair of electric field plates are called the centre plates because they are in between the guard plates. The Raman transitions are driven in between the guard plates.

The spacing of these plates is different for each region. This means that the electric field that interacts with the molecules is slightly different in the two Raman regions and therefore the transition frequencies are different. The different electric fields alters Δ, so that its value is different in the lower Raman region compared to the upper region. However, this change is a very small fraction of the total value of Δ, small enough that we can compensate by changing the Raman AOM frequency. The reason why the electric fields plates have different spacings is historical.

Until we introduced the Raman technique to the experiment we used oscillating magnetic fields from the rf loops to drive the F=0 to F=1 transition. Both rf fields were switched on at the same time, unlike the technique that is described in Section (3.6). This meant that the top rf loop could drive the molecules while they were still in the lower rf loop region, and visa versa. This had the potential to cause systematic effects because the molecules could keep a coherence between the F=0 and F=1 states which evolves in the electric field due to the Stark interaction. This effect is called the Ramsey effect. To avoid it the rf frequencies used in the lower and upper rf loop regions should be different. In which case the rf transition frequencies of the molecules should also be changed to keep the rf fields on resonance. This was achieved by changing the electric fields between the lower and upper regions by changing the plate spacings.

To accommodate this infrastructure with the new Raman implementation we first used two sets of Raman beams each with their own AOM, which is different from the set up described above. One set of beams was used to drive the Raman transition in the lower Raman region, and the other set of beams was used to drive transitions in the upper Raman region. This enabled us to set the correct transition frequency for each set of beams, using the AOM's. However, we found that the Raman transition efficiencies were limited by laser power. To solve this problem we devised a set-up using only one AOM. To achieve this the Raman light is sent through the upper Raman region first. On exiting the vacuum chamber the Raman beams are sent through a telescope, back into the vacuum chamber, and through the lower Raman region. Figure (3.5a) shows the pump, probe, and Raman laser beams and there positions relative to the vacuum chamber. The figure also

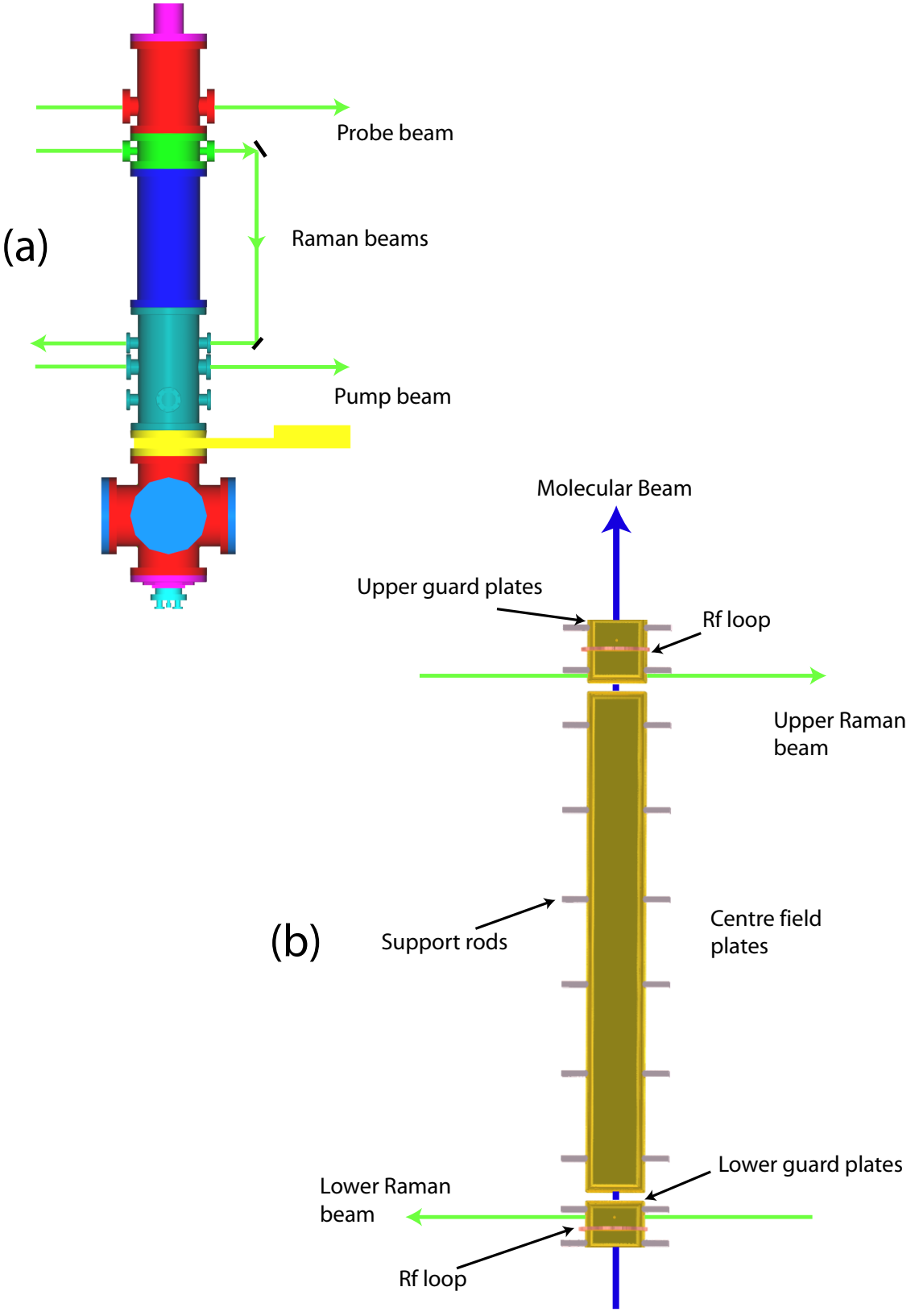

Figure 3.5: (a): Shows the laser beams enter and exit the vacuum chamber. The Raman beams enter at the top and are reflected down to go through the bottom part of the vacuum chamber. (b): Inside the vacuum chamber sit the electric field plates and rf loops. The Raman beams position is shown relative to the field plates. The electric field support rods are also shown, see Chapter (4).

Parameter set	Parameter
Raman	Frequency difference between lasers beams
	Laser intensities
	Detuning from $\mid A\rangle$ state
	FM modulation frequency ($\geq$ 99 kHz)
	Relative polarisations
	Spot size
	Laser beam overlap
	Laser beam alignment
	Laser beam position relative to field plates

Table 3.1: The Raman beam parameter space

shows that the Raman beam enter the vacuum chamber near the top, then they are reflected down to go through the bottom Raman region. The positions where the upper and lower Raman beams pass relative to the electric field plates is shown in part (b) of the figure.

To operate the AOM with the correct drive frequency for each transition region we frequency modulate (FM) the HP8657A synthesizer's output by the appropriate amount. Just before the molecule pulse reaches the lower Raman region we pulse the AOM on with the correct frequency for the lower Raman transition. After the molecular pulse has exited the lower Raman region the AOM drive is changed to operate with the correct frequency for the upper Raman region. In this way both Raman regions use the same set of laser beams and use only one AOM, conserving laser power. The HP8657A synthesizer can frequency shift its signal in FM mode by a maximum of 99 KHz, which is sufficient for the two transitions.

3.5 Raman Transitions

The laser powers in the shifted and unshifted Raman beams are set to around 20 mW each. To make sure that the overlap of the Raman beams with the molecular beam is optimal we switch the electric field off and block the pump and shifted Raman light. The unshifted Raman beam operates as a pump, pumping the F=1 molecules into the F=0 state. Final alignment, of the unshifted beam, can be made of by optimising the pumping efficiency. Since the shifted beam is overlapped and parallel with the unshifted beam both beams are aligned to the molecules in this way. We then switch the electric field back on and unblock the shifted beam to

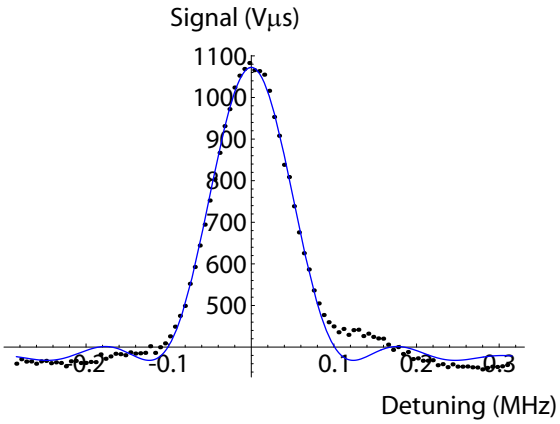

Figure 3.6: Upper Raman transition. The x-axis shows the detuning of the Raman light from the transition frequency. The solid curve is a fitted sinc squared function.

drive the Raman transitions. A list of the tunable Raman parameters are shown in Table (3.1).

To find the transition frequency we scan the frequency of the shifted Raman beam. A typical Raman resonance signal is shown in Figure (3.6). The signal, in Vμs, is proportional to the number of molecules in the F=1 state after undergoing the Raman transition. The x-axis is the laser beam detuning δ from the resonance frequency. The peak of the signal is approximately 1100 Vμs, this corresponds to approximately 56% of the total number of F=1 molecules, measured when the pump and Raman beams are blocked. The solid line in the figure is a fitted sinc squared function. We see that the theory fits the data well around the peak of the signal. However, data does not fit the theory curve very well in the wings of the transition. This is probably due to target heating, from the YAG, over the time of the scan, which changes the number of molecules in the YbF pulses. The width of the Raman transition is determined by the amount of time the molecules spend in the Raman laser beams, which is approximately 6 μs.

The AOM power can also be scanned and set to achieve a π pulse. Figure (3.7) shows the AOM power scan with the Raman light on resonance with the hyperfine transition. This can be contrasted with the rf transition power curve, Figure (3.8) in Section (3.7). With the rf we are able to scan through more that one π pulse. However, the Raman laser beams are limited by the output power of the laser and the limited range of the AOM. With these limitations we barely have enough laser power to drive the π pulse necessary for the experiment.

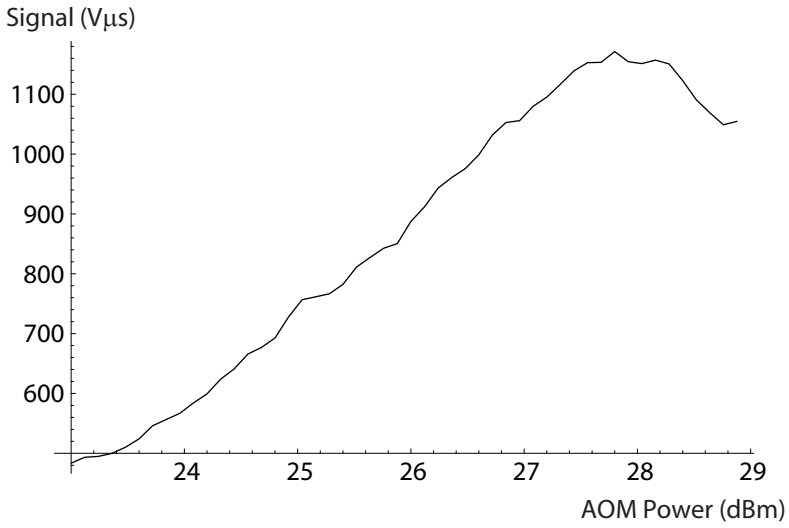

Figure 3.7: Upper Raman transition Rabi power curve. The x-axes shows the AOM power and the y-axis the LIF signal.

3.6 Rf Implementation

The rf setup is described in [29] and has not been changed significantly during my PhD. Around each set of guard plates there is an rf loop connected to the synthesizers through d.c. blocking capacitors. The rf antennas are made from copper loops 8 cm in diameter, 1 cm wide, and 1 mm depth. They are placed such that the fields they produce are perpendicular to the electric field. This ensures the correct transitions are driven, see Figure (3.5. There are two synthesizers one is the same used for the Raman AOM and the other is a HP3325B. This synthesizer can supply a maximum frequency of 61 MHz. In order to drive the transition between the ground state hyperfine levels it is frequency quadrupled to approximately 170 MHz. Both synthesizers are amplified before reaching the rf antennas. The signal from the HP3325B synthesizer is also filtered appropriately.

The rf signals are sent to the rf loops via a switch box, which is computer controlled such that the time the rf is switched on relative to the valve pulse can be altered. This means that the lower rf loop can be switched on as the molecular pulse arrives and switched off when it has passed that region of the experiment. Then the upper rf loop can be switched on and off when the molecules arrive and leave. This switching of the rf helps avoid systematic Ramsey effects from the two rf fields interfering with each other.

Parameter set	Parameter
Rf	Frequency
	Power
	Upper and lower switch on time
	Upper and lower switch off time

Table 3.2: The rf parameter space

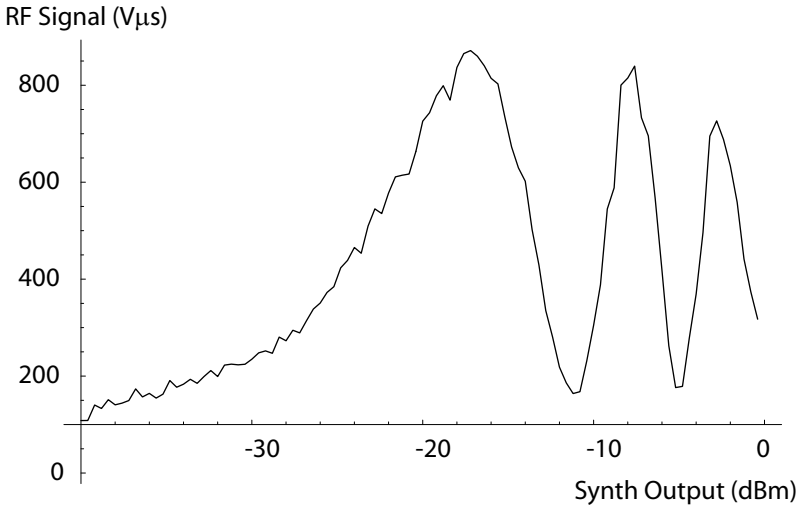

Figure 3.8: Rf power curve.

3.7 Pulsed Rf Transitions

The procedure for optimising the rf transitions for both rf loops can be found in [29, 54]. However, since we have implemented the switching scheme, to switch on each rf drive when it is required, there are some extra parameters to optimise. Table (3.2) lists the tunable parameters that optimise the rf transitions.

To optimise the lower rf transition we first apply the pump laser beam to the molecules. Then the rf transition frequency is scanned. After finding the peak transition frequency we scan the rf power sent to the loop. An example curve is shown in Figure (3.8). On the y-axis the rf signal is shown in Vμs. This is proportional to the number of molecules in the F=1 state after the rf transition, measured by the PMT. From this graph we read off the amplitude for a π pulse, and set the synthesizer to this. In this case we see that the π pulse occurs at a synthesizer output power of approximately -18 dBm. The other rf transition is optimised in a similar fashion.

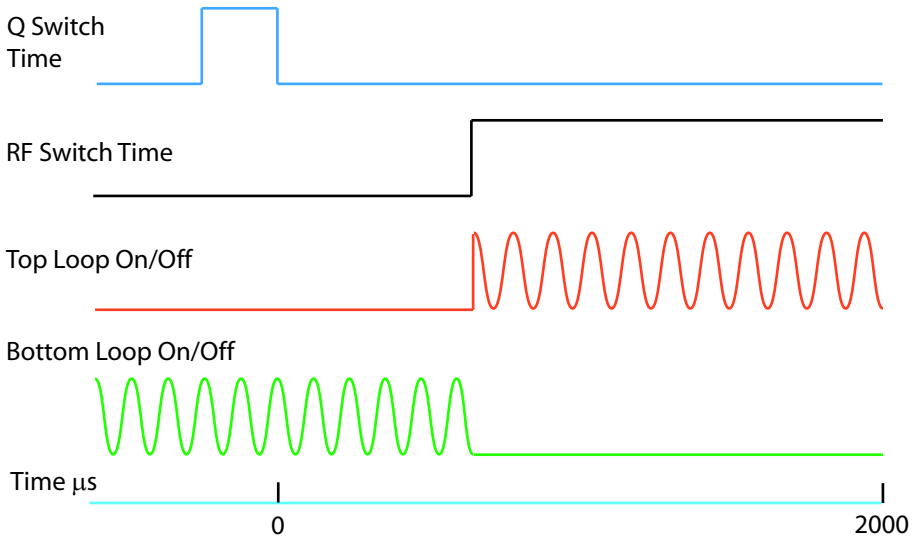

Figure 3.9: The rf switch timings relative to the Q-switch.

Once the rf has been setup for the correct frequency and power, the timings are scanned. Using the control computer to scan the rf switch time: the time, relative to the Q-switch pulse, when the rf drive is switched from the lower loop to the upper loop. For example, if the rf switch time is set to 1000 μs, then the lower rf loop will be switched on at the Q-Switch pulse and switched off after 1000 μs. Simultaneously the upper rf loop will be switched on and then switched off again after the molecules have been detected. Figure (3.9) shows a timing diagram for the rf switching. In this diagram we see that at the beginning the Bottom rf loop is switch on. Some time after the Q-Switch is fired the bottom rf is switch off and the top loop switched on. This occurs at the rf switch time, which switches from low to high.

The rf switch time can be scanned, as shown in Figure (3.10), to find the optimum timing. The signal in the Figure starts to rise at around 900 μs which indicated that the leading molecules in the pulse start to undergo rf transitions after 900 μs. At around 1000 μs all of the molecule pulse has been acted upon by the rf field indicated by the plateau of the signal. In a similar fashion it is possible to determined how long the rf needs to be on for in order to get the maximum transfer of molecules. For the lower rf region, the rf field is only required to be switched on for 100 μs to get the maximum signal. For the upper rf region, the rf field needs to be switched on for slightly longer because the molecular pulse has spread out spatially.

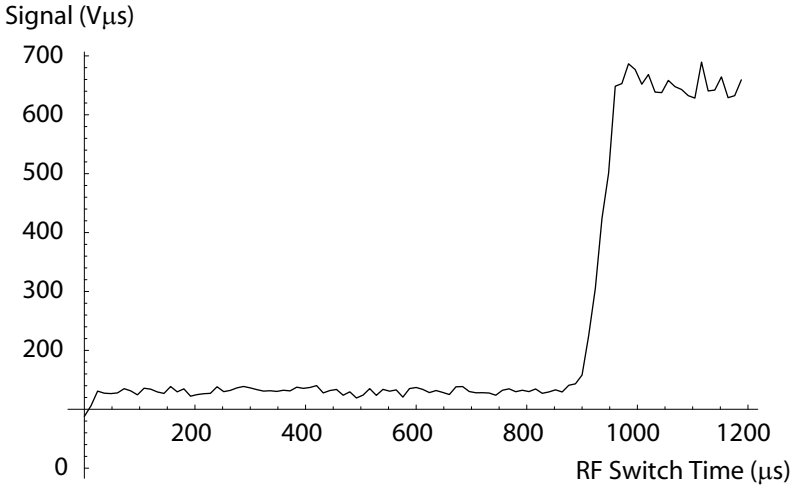

Figure 3.10: Scan of the rf switch timing.

After the rf timings have been set it is worthwhile to scan the rf power again to find the optimum for the pulsed rf. This leads to some interesting effects in the time of flight profiles. In Figure (3.11a) I have plotted the results of a model simulation. On the x-axis is the rf amplitude required to drive Rabi flops in the molecules, and on the y-axis is the arrival time of the molecules at the detector. The light regions indicate the molecules in the F=1 state after the rf loop. The brightness of these light regions indicate the number of molecules. In (b) the experimental data is shown, and this time the x-axis indicates the rf synthesizer output in dBm.

In this experiment we scan the rf synthesizer output connected to a single rf loop and recorded the time of flight profiles of the molecules. For each new value of synthesizer output power we record a time of flight profile. The contour plots in Figure (3.11) show all of the time of flight profiles together, with the brightness representing the normal Vμs signal. The model, used to generate Figure (3.11a), simulates an rf transition between a two level system from a single rf loop. The equations for the population transfer are derived in [53]. These equations do not take into account that the rf field is not uniform over the molecular beam line. To include this in the model the rf field amplitude is modelled as the magnetic field amplitude from a signal loop of wire. This approximation does not include the finite thickness of the rf loop, or more seriously the effect that the electric field plates have on the rf field. However, the approximation is reasonable since the effect of the field plates on the rf field has been measured to be negligible. The model also takes into account the velocity distribution of the molecules which approximated the supersonic source to be a point source producing a Gaussian velocity distribution.

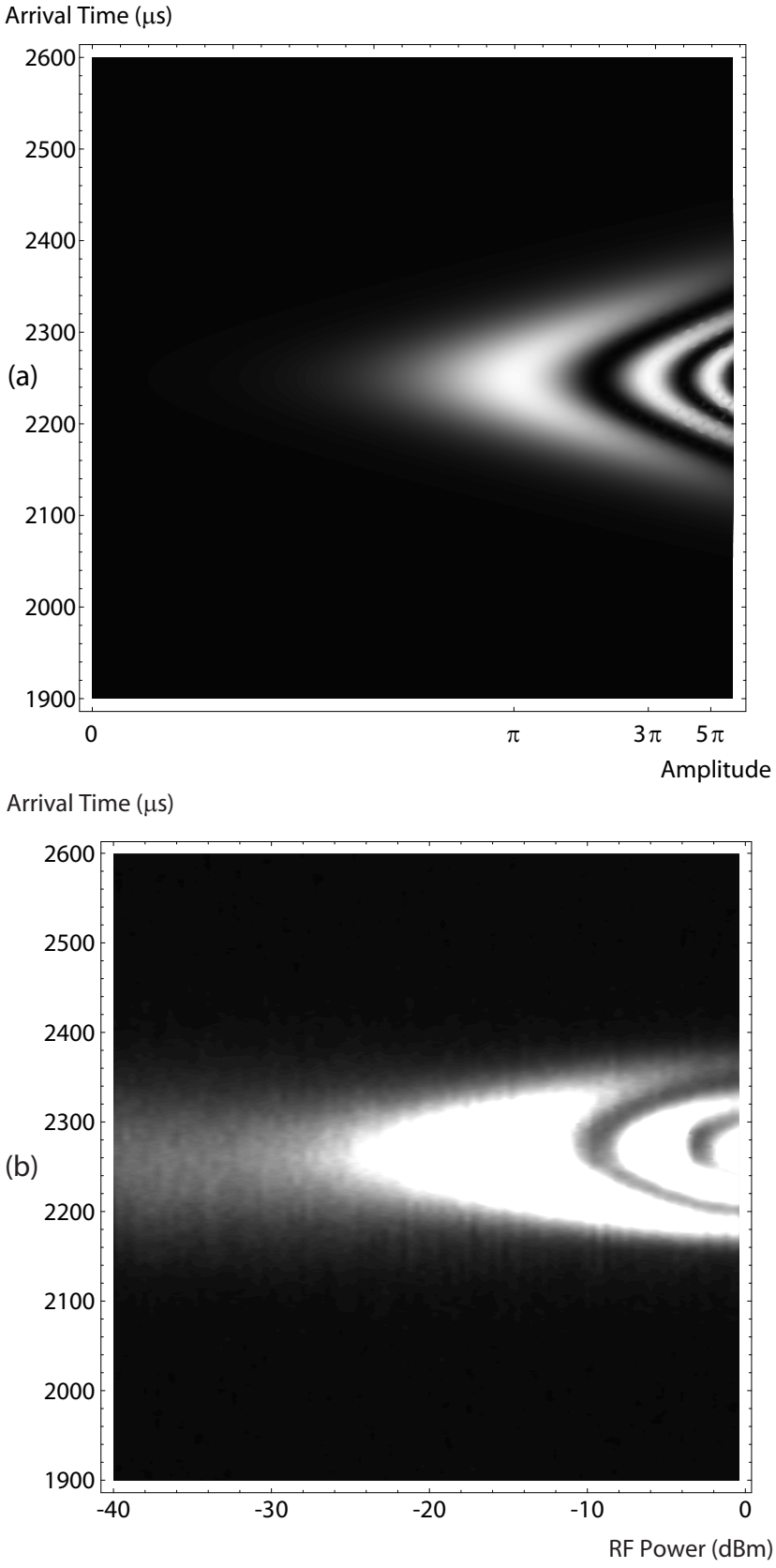

Figure 3.11: (a) Simple model of the rf transitions. With rf amplitude on the x-axis and molecular arrival time on the y-axis. The brightness of the light contours indicate the amount of molecules detected in the F=1 state after the rf loop. (b) This plot shows the experimental data. This time the x-axis shows the synthesizer power output in dBm.

In the model the rf field is switched on when the fastest molecules arrive at the rf loop. Molecules of different velocities reach different positions when the rf field is switched on and therefore interact with different rf field amplitudes because of the spatial variation of the rf field. The molecules then interact with the rf field for the time that it is on, 100 μs. If the rf amplitude is such that the molecules of mean velocity undergo a π transition, the other molecular velocity accumulate more or less Rabi flopping phase. The results of the simulation are shown in Figure (3.11a). It shows molecules arriving at 2250 μs undergoing a 5π transition, whereas slower molecules arriving at 2190 μs undergo a 3π transition and even slower ones arriving at 2140 μs only undergo a π transition. This is because the slower molecules are further from the centre of the rf loop when the field is turned on, and therefore acquire less Rabi flopping phase. A similar effect is seen for the faster molecules. In the experimental data a similar behaviour is found, Figure (3.11b). The reason why the data does not seem to be symmetric around the mean arrival time is most likely to be due to incorrect setup of the rf timings. For example, if the rf was switched on slightly late, then the faster molecules would be nearer the edge of the electric field plates then they should be. At the edge of the field plates the electric field is less than in the middle of the plates and therefore the molecules' Stark shift is different. These faster molecules would therefore be slightly Stark shifted out of resonance with the rf field, reducing the transition efficiency.

3.8 The Stark Shift Measurement

Since we use the Stark shift of the A-X transition to control the Raman transition, we need to have a good understanding of it. In this section I describe how we measured it [10].

This measurement was performed before the implementation of the supersonic source. Instead, a crucible, containing four parts Yb metal pieces and one part aluminum fluoride powder, by mass, was resistively heated to 1500 K. At the top of the crucible was a slot of approximately 0.5 x 4 mm through which the molecules escaped into the vacuum chamber forming a molecular beam. The vacuum system used was essentially the same with two turbo pumps top and bottom. Above the oven, some baffles collimated the beam, the upper baffle with a slot of 6 x 36 mm. These baffles also reduced the background blackbody radiation from the oven which was enclosed in a magnetic shield which also acted as a heat shield. For further details on the oven source see [29, 54].

To manipulate the population of the molecules in the different states we applied a

pump laser beam tuned to the Q(0) transitions, which interacted with the molecules in the lower guard electric-field region. The plate spacing was 11.85 ±0.01 mm. (This was measured, by recording the plate spacing at the four corners of the plates. The diagonal measurements were averaged together, and then these two spacing were also averaged together to give the spacing above.) The laser frequency was scanned by 2 GHz through the Q(0) resonances. This laser light was produced by a Coherent 699 dye laser and was referenced to a cavity of free spectral range (FSR) 151.8 ±0.2 MHz, see Figure (3.4). The cavity was not temperature stabilised, but had enough passive stability for our purposes, as we could see from a comparison of the Q(0) line with the cavity fringes.

In this experiment we measured the Stark shift of Q(0) transitions. This was achieved by scanning the pump laser frequency through the Q(0) transition lines while recording the F=1 LIF signal with the probe laser. This was preformed for several different applied electric fields. If the Q(0) line were the only resonance excited by the laser light, then this would have been enough to measure its Stark shift. However, other rotational lines were also excited by the laser which have different Stark shifts obscuring the Q(0) transition of interest. In order to eliminate this background we tagged the Q(0) line using the rf loop, downstream from the capacitor, to excite transitions between the ground state hyperfine levels. This enabled us to take the difference between the count rate with the rf on and the rate with the rf off, ΔI, and suppress the background signal.

An example pump laser scan is shown in Figure (3.12). In plot (a) the top graph shows the cavity output and below the molecular spectrum, ΔI, for the laser frequency scan. This data was taken with the electric field off and the data was averaged for two consecutive scans. Plot (b) shows the same molecular spectrum, but Stark shifted in an applied electric field of 4.1 kV, together with the corresponding cavity transmission fringes. This was repeated for each value of the electric field. First we took two scans with the electric field off and then with the electric field on. This enabled us to use the Q(0) transitions in zero field as a frequency reference for each different electric field, thereby avoiding possible systematic errors from cavity and laser drift.

The main feature of these plots is the peak and dip in the molecular spectrum. When the rf field is switched on, some of the molecules which were initially pumped out of the $F = 1$ state are repumped back into the $F = 1$ level by the rf field. When the rf field is switched off this does not occur. This explains the peak in the spectrum. When the scan laser is on resonance with the $F = 0$ state the effect is reversed making a dip in the signal.

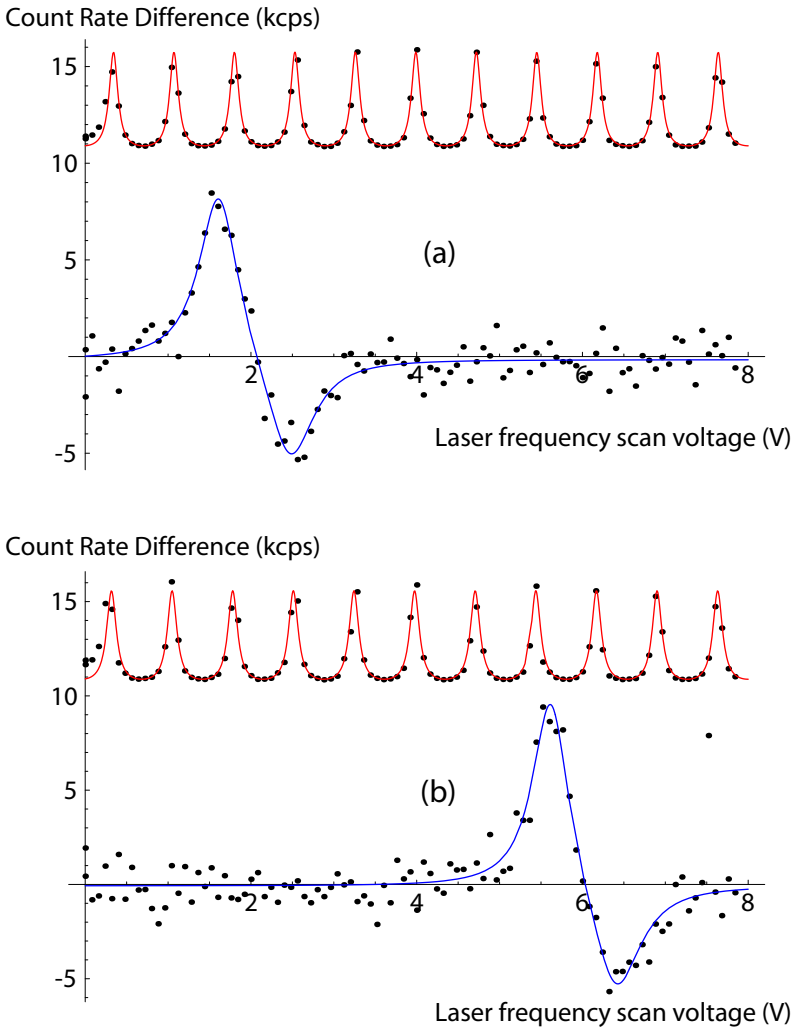

Figure 3.12: ΔI measured in thousands of counts per second. The x-axis shows the control voltage to the laser controlling its frequency. Graphs show both the cavity output and the ΔI signal.

To extract the Stark shift from the data we first converted the laser scan voltage into a laser output frequency. This was performed by separately fitting the cavity scans for each electric field value to an Airey function,

$$A(v) = N + \frac{B}{1 + F\sin^2(\frac{CV}{2} + \phi)}. \tag{3.19}$$

The fit parameters were the background light scatter N, a scalar proportional to the light intensity B, the finesse of the cavity F, a scalar C proportional to the known FSR, and a phase offset ϕ. For each fit we are able to extract a conversion between laser scan voltage, V, and laser output frequency, f_L using the standard theory of Febry-Perot cavities. We found no systematic drift of these calibration which enabled us to average them together.

Using this conversion between scan voltage and laser frequency, f_L, we converted the x-axis of the pump laser scans into laser frequency scans. We then fitted each ΔI spectra to the sum of two Lorentzians,

$$rf(f_L) = Q_1 \left(\frac{\delta_1}{2}\right)^2 \left(\frac{1}{(f_L - c_1)^2 + (\frac{\delta_1}{2})^2}\right) - Q_2 \left(\frac{\delta_2}{2}\right)^2 \left(\frac{1}{(f_L - (c_1 + s))^2 + (\frac{\delta_2}{2})^2}\right). \tag{3.20}$$

The fit parameters were the amplitudes Q_1 and Q_2, the centre frequencies of the Q(0) F=1 line c_1, and the widths of the transitions δ_1 and δ_2. The centre frequency of the Q(0) F=0 line was constrained to be the centre of the Q(0) F=1 line plus the known Stark shifted hyperfine splitting, s, between the F=1 and F=0 levels. Example fits of the cavity and ΔI spectra are shown as red and blue lines respectively in Figure (3.12).

For each electric field value we extracted the Stark shift of the Q(0) transition frequency from the data, Table (3.3). We then subtracted the known Stark shift of the ground F=0 hyperfine state to find the Stark shift of the $|\ A^2\Pi_{1/2}\rangle$ state. The X-state Stark shift is known to 1% from the spectroscopy of Sauer *et al* [64]. The differential splitting between the F=0 and F=1 levels of the X-state is only 1 MHz in the largest electric field, which is negligible here. Table (3.3) shows the data. For each electric field value the measured Stark shift of the A-X state, δf_{A-X} is listed. In the next column the known ground F=0 state Stark shifts, δf_X, are shown, including the 1% systematic error due to the uncertainty in the X-state dipole moment. In the next column the derived A-state Stark shifts, δf_A, are given. The numbers in parentheses indicate one standard deviation of the measurement, due to random noise and the systematic uncertainty of the absolute value of the

Field V/cm	δf_{A-X} MHz	δf_X MHz	δf_A MHz
819	35.4 (2.6)	-59.9 (0.6)	-24.5 (2.6)
1646	142.4 (2.9)	-239.5 (2.4)	-97.1 (3.7)
2473	319.1 (3.6)	-532 (5.3)	-214 (6.4)
3300	543.9 (4.0)	-931 (9.3)	-387 (10)
4127	826.3 (5.4)	-1423 (14)	-596 (15)
4954	1151.5 (6.8)	-1997 (20)	-846 (21)

Table 3.3: Measured Stark shift δf_{A-X} of the A-X transition at the six values of the applied electric field. Numbers in parentheses indicate one standard deviation of the measurement, due to a combination of random noise and systematic uncertainty in the absolute electric field. The known ground state shift δf_X is also given, including the systematic error due to the 1% uncertainty in the X-state dipole moment. The derived A-state shifts δf_A are given in the final column.

electric field. The hyperfine splitting of the A-state is approximately 2.5 ± 0.7 MHz, this means that the systematic error due to its Stark shift is negligible.

The Stark shift of the A-state fits very well to a purely quadratic form,

$$\delta f_A = -\frac{1}{2}\alpha E^2 \tag{3.21}$$

as shown in Figure (3.13). This figure shows the Stark shift of the A-state versus the square of the electric field, E^2. The error bars show only the measurement error and not the error from the uncertainty in the X-state shift. The solid line is the fit of the above function. The polarisability of the A-state, α, was found by fitting the Stark shift, δf_A, data to the above expression. The error bars used in the fit were from the measurement error in δf_{A-X} and the uncertainty in δf_X. This was due to the 1% uncertainty in the electric field, which corresponds, by equation (3.21), to a 2% uncertainty in the δf_X shifts. In this way we found the polarisability of the A-state is,

$$\alpha = (70.3 \pm 1.5) Hz/(V/cm)^2. \tag{3.22}$$

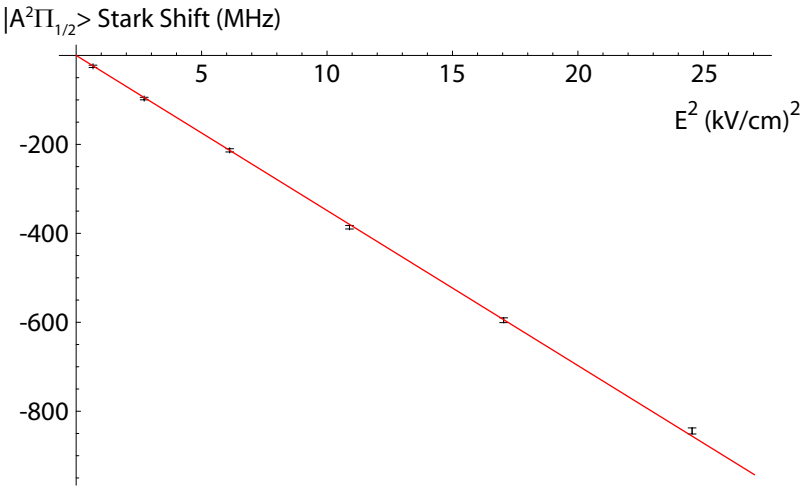

Figure 3.13: Stark shift of the $|\, A^2\Pi_{1/2}\rangle$ state versus the square of the electric field, E^2. The solid line shows the fit for the polarisability.

Chapter 4

The Interferometer

In this chapter I describe how we perform molecular interferometry to make sensitive measurements of magnetic and electric field interactions with the YbF molecules. The first section in this chapter outlines the theory behind the molecular interferometer. The experimental implementation and a characterisation of the interferometer's performance follow.

4.1 Theory

Optical interferometry has been used for a long time in physics to measure small length differences or changes. The light beam is split and the optical path lengths of the two beams differ. When the light is recombined the intensity depends on this path difference through the phase shift. In this experiment we use YbF to probe for small phase shifts due to magnetic and electric fields interacting with the molecules. The two arms of this interferometer are the $\mid F, m_F\rangle = \mid 1, -1\rangle$ and $\mid 1, +1\rangle$ hyperfine states in the $X^2\Sigma^2_{1/2}(\nu = 0, N = 0)$ ground state of YbF. Small changes in interaction energy lend to phase differences between the two arms and this changes the interferometer's signal.

In summary, we start with the YbF molecules in the $\mid 0, 0\rangle$ state and drive a Raman transition to put the molecules in a coherent superposition of the $\mid 1, \pm 1\rangle$ states. The molecules then evolve in electric and magnetic fields, producing a phase difference between the $m_F = \pm 1$ levels. We then apply a second Raman transition to drive the two parts back to the $\mid 0, 0\rangle$ state. The population remaining in the F=1 state is probed by LIF spectroscopy and depends on the phase difference evolved between the $m_F = \pm 1$ levels. This technique is very similar to a Ramsey separated oscillator type of experiment which tests the coherence between the $F = 0$ and $F = 1$ states [53]. In this experiment however we test the coherence between the

nearly degenerate $\mid 1, \pm 1\rangle$ states.

To describe the operation of this theoretically I choose a basis set of five states: $\mid 0,0\rangle$, $\mid A^2\Pi_{1/2}\rangle$, $\mid 1,+1\rangle$, $\mid 1,0\rangle$, and $\mid 1,-1\rangle$, with the direction of the quantization axis being that of the applied electric field. The first stage of the experiment is to optically pump out the $\mid 1,0\rangle$, $\mid 1,\pm 1\rangle$ levels with the pump laser beam. As previously discussed, the pumping is not 100% efficient, however incomplete pumping leads only to a background signal and a reduction in the interference fringe amplitude and does not compromise the operation of the interferometer. Therefore, I assume ideal pumping and hence the pumping stage is described by the matrix

$$\boldsymbol{Pump} = \begin{pmatrix} 1 & 0 & 0 & 0 & 0 \\ 0 & 0 & 0 & 0 & 0 \\ 0 & 0 & 0 & 0 & 0 \\ 0 & 0 & 0 & 0 & 0 \\ 0 & 0 & 0 & 0 & 0 \end{pmatrix}. \tag{4.1}$$

The next stage of the experiment is to change the state of the molecules from $\mid 0,0\rangle$ into a coherent superposition of the $\mid 1,\pm 1\rangle$ states. To achieve this we use the bottom Raman transition. Using equation (3.17) of Section (3.2) we can numerically find the state of the system after the Raman transition.

However, first of all we recognise that equation (3.17) is written in a three level basis: $\mid F=0\rangle$, $\mid A^2\Pi_{1/2}\rangle$, and $\mid F=1\rangle$. Therefore, to use this equation here we must write it in our five level basis. To do this I will introduce a coupled-basis with basis vectors: $\mid 0,0\rangle$, $\mid A^2\Pi_{1/2}\rangle$, $\mid 1,+1\rangle + \mid 1,-1\rangle$, $\mid 1,0\rangle$, and $\mid 1,+1\rangle - \mid 1,-1\rangle$. When we include the polarisation of the Raman lasers, the Raman amplitude takes the form of $\vec{E}_{L1} \times \vec{E}_{L2}$. If we choose the polarisations to be along the z and x directions, the Raman lasers couple the $\mid 0,0\rangle$ state to the state $\mid 1,+1\rangle + \mid 1,-1\rangle$ and not to the state $\mid 1,+1\rangle - \mid 1,-1\rangle$. This is shown in Figure (4.1) which shows the ground and first electronically excited state in the new coupled-basis, with the states connected by the lasers. Laser one is polarised along the z-axis, and laser two is polarised along the x-axis. This means equation (3.17) becomes,

$$\frac{d}{dt}\begin{pmatrix} C_0 \\ C_A \\ C_c \\ C_{1,0} \\ C_u \end{pmatrix} = \begin{pmatrix} 2\Delta_{A0} & \Omega_{A0} & 0 & 0 & 0 \\ \Omega_{A0} & 0 & \Omega_{1A} & 0 & 0 \\ 0 & \Omega_{1A} & 2\Delta_{A1} & 0 & 0 \\ 0 & 0 & 0 & 0 & 0 \\ 0 & 0 & 0 & 0 & 0 \end{pmatrix}\begin{pmatrix} C_0 \\ C_A \\ C_c \\ C_{1,0} \\ C_u \end{pmatrix} \tag{4.2}$$

where C_c and C_u are the state coefficients for the coupled and uncoupled states.

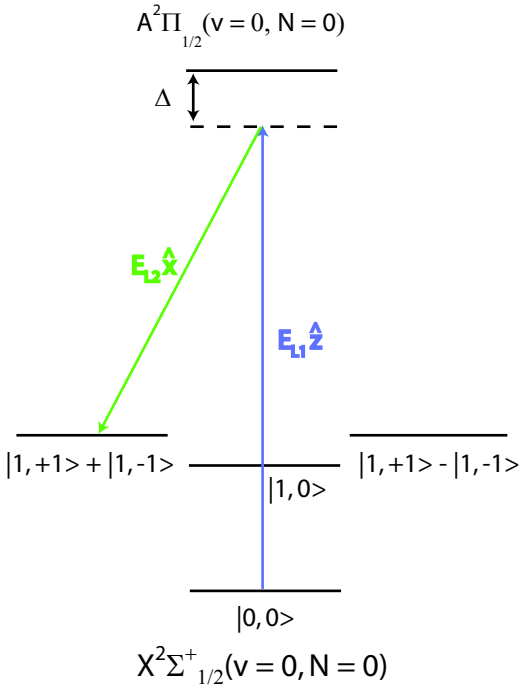

Figure 4.1: The ground and first electronically excited states are shown in a coupled-basis. The laser fields are polarised such that the $\mid 0,0\rangle$ state couples to $\mid 1,+1\rangle + \mid 1,-1\rangle$ state.

Now we can transform this equation back into the original basis with the operator,

$$\begin{pmatrix} 1 & 0 & 0 & 0 & 0 \\ 0 & 1 & 0 & 0 & 0 \\ 0 & 0 & \frac{1}{\sqrt{2}} & 0 & \frac{1}{\sqrt{2}} \\ 0 & 0 & 0 & 1 & 0 \\ 0 & 0 & \frac{1}{\sqrt{2}} & 0 & -\frac{1}{\sqrt{2}} \end{pmatrix}. \tag{4.3}$$

Applying this transformation to equation (4.2) gives,

$$\frac{d}{dt}\begin{pmatrix} C_{0,0} \\ C_A \\ C_{1,+1} \\ C_{1,0} \\ C_{1,-1} \end{pmatrix} = \begin{pmatrix} 2\Delta_{A0} & \Omega_{A0} & 0 & 0 & 0 \\ \Omega_{A0} & 0 & \frac{\Omega_{1A}}{\sqrt{2}} & 0 & \frac{\Omega_{1A}}{\sqrt{2}} \\ 0 & \frac{\Omega_{1A}}{\sqrt{2}} & \Delta_{A1} & 0 & \Delta_{A1} \\ 0 & 0 & 0 & 0 & 0 \\ 0 & \frac{\Omega_{1A}}{\sqrt{2}} & \Delta_{A1} & 0 & \Delta_{A1} \end{pmatrix}\begin{pmatrix} C_{0,0} \\ C_A \\ C_{1,+1} \\ C_{1,0} \\ C_{1,-1} \end{pmatrix}. \tag{4.4}$$

Equation (4.4) may be written as $\frac{d}{dt}C = RC$. In principle we may solve this by means of an operator P that diagonalises R. Then equation (4.4) can be written as $\frac{d}{dt}(P^{-1}C) = D(P^{-1}C)$, where $D = P^{-1}RP$ is diagonal. We may now substitute $Y = (P^{-1}C)$ and solve with the solutions $Y = Y_0 e^{Dt}$, where Y_0 depends on the initial state of the system. Thus

$$\begin{pmatrix} C_{0,0} \\ C_A \\ C_{1,+1} \\ C_{1,0} \\ C_{1,-1} \end{pmatrix} = P\begin{pmatrix} 1 \\ 0 \\ 0 \\ 0 \\ 0 \end{pmatrix} e^{(P^{-1}RP)t} \tag{4.5}$$

for the initial condition that at $t = 0$, $C_{0,0} = 1$ and $C_A = C_{1,+1} = C_{1,0} = C_{1,-1} = 0$. The solution for the diagonal matrix D can be found numerically and with this solution we may plot the state population as a function of time, Figure (4.2). In this figure red curve is the probability of the molecules occupying state $\mid 0, 0\rangle$. The blue curve is for state $\mid A^2\Pi_{1/2}\rangle$, and the green curve is for states $\mid 1, \pm 1\rangle$. The initial conditions are that the molecules only occupy the state $\mid 0, 0\rangle$ before the Raman lasers are switch on. The $\mid 1, 0\rangle$ state is not shown as it is never populated. The parameters have been chosen such that a π pulse occurs at $t = \pi$, and molecules are transferred maximally to states $\mid 1, \pm 1\rangle$.

From Figure (4.2) we can see that at the π pulse condition, $\Omega_{eff}t_\pi = \pi$, there is maximal transfer from state $\mid 0, 0\rangle$ to the $\mid 1, +1\rangle$ and $\mid 1, -1\rangle$ states. We can also see that the upper $\mid A^2\Pi_{1/2}\rangle$ state occupation probability, the blue curve, remains

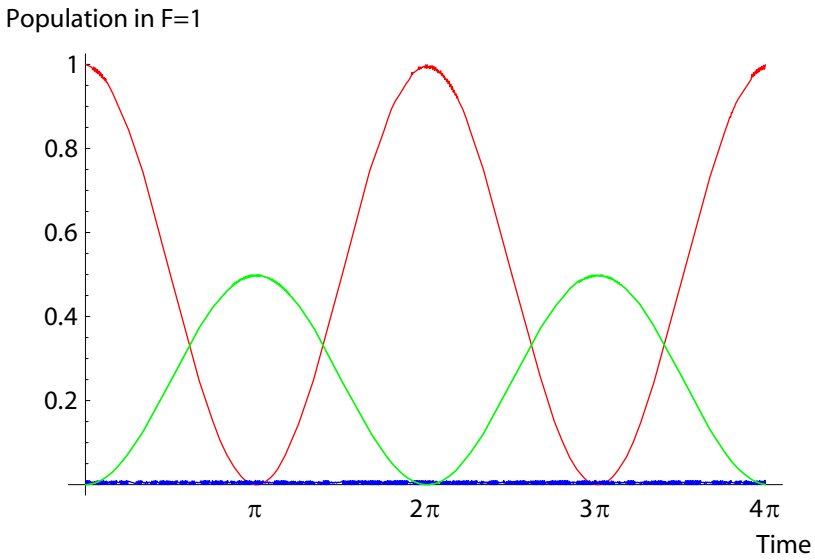

Figure 4.2: Numerical solution of the Raman transition. The red curve is the probability of the molecules occupying state $\mid 0,0\rangle$. The blue curve is for state $\mid A^2\Pi_{1/2}\rangle$, and the green curve is for states $\mid 1,\pm 1\rangle$. This is for the initial condition that the molecules only occupy the state $\mid 0,0\rangle$ before the Raman lasers are switch on. The $\mid 1,0\rangle$ state is not shown as it is never populated. The parameters have been chosen such that a π pulse occurs at $t = \pi$, and molecules are transferred maximally to states $\mid 1,\pm 1\rangle$.

extremely small at all times. For the interferometer we require that the Raman transitions act on the molecules with π pulses. This is achieved by increasing the laser beam powers to maximise the number of molecules transfered to the F=1 states. I represent the Raman transition as a function called $\boldsymbol{Raman}(t, l_p, state)$, whose arguments are the interaction time, the laser powers, l_p, and the initial state of the system.

After the bottom Raman transition, the molecules evolve in parallel electric and magnetic fields. The normal Stark interaction will be ignored here as there is no differential Stark shift of the F=1 levels of interest. The evolution of the wavefunction in the magnetic and electric field is described by the matrix,

$$\boldsymbol{Bfield}(T) = \begin{pmatrix} e^{-i\Omega_0 T} & 0 & 0 & 0 & 0 \\ 0 & e^{-i\Omega_A T} & 0 & 0 & 0 \\ 0 & 0 & e^{-i(\Omega_1+\xi)T} & 0 & 0 \\ 0 & 0 & 0 & e^{-i\Omega_1 T} & 0 \\ 0 & 0 & 0 & 0 & e^{-i(\Omega_1-\xi)T} \end{pmatrix} \tag{4.6}$$

where $\xi = \frac{1}{\hbar}(\mu_B B - d_e.E_{eff})$ is the energy for the magnetic and electric field interaction, $\hbar\Omega_0$, $\hbar\Omega_A$, and $\hbar\Omega_1$ are the unperturbed energies of the F=0, $\mid A^2\Pi_{1/2}\rangle$, and F=1 states, and T is the interaction time. The molecules now undergo the second Raman transition. We may describe the total evolution of the system for arbitrary initial conditions as,

$$\boldsymbol{Int}(B, T, t, l_p, state) = \boldsymbol{Raman}\left(t, l_p, \boldsymbol{Bfield}\left(T\right) \cdot \boldsymbol{Raman}\left(t, l_p, \boldsymbol{Pump} \cdot state\right)\right) \tag{4.7}$$

where "*state*" represents the initial state that the system evolves from. If the system starts in state $\mid 0, 0\rangle$ then the final population measured in states $\mid 1, \pm 1\rangle$ is given by the modulus squared of,

$$P_1 = \langle 1, +1 \mid \boldsymbol{Int}(B, T, t, l_p, \mid 0, 0\rangle) + \langle 1, -1 \mid \boldsymbol{Int}(B, T, t, l_p, \mid 0, 0\rangle). \tag{4.8}$$

The first thing that we should note about this equation is that it includes nothing about the velocity of the molecules. Since different velocity classes will not be transferred optimally in the Raman transitions and will spend different amounts of time in the magnetic field we should integrate this equation over the velocity distribution. Using the velocity distribution of equation (2.7) of Section (2.2) we write,

$$\overline{P}_1 = \int_0^\infty f(v)[\langle 1, +1 \mid \boldsymbol{Int}(B, \frac{a}{v}, \frac{b}{v}, l_p, \mid 0, 0\rangle) + \langle 1, -1 \mid \boldsymbol{Int}(B, \frac{a}{v}, \frac{b}{v}, l_p, \mid 0, 0\rangle)]dv \tag{4.9}$$

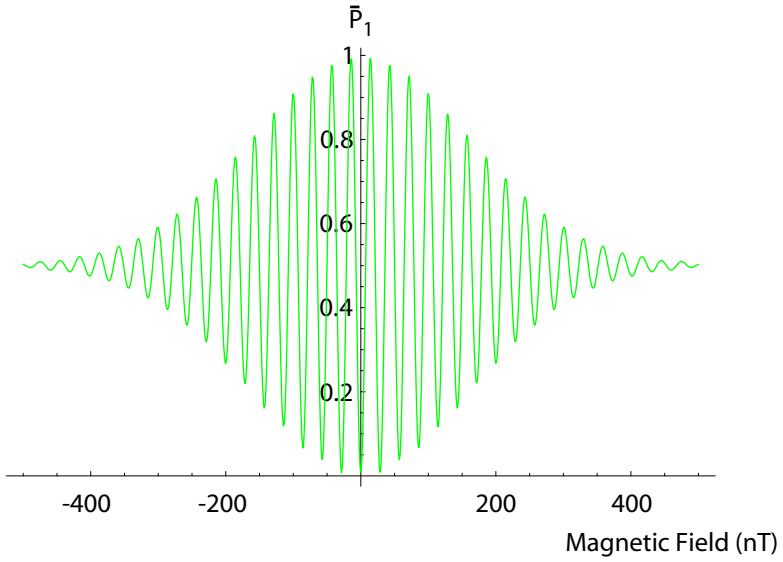

Figure 4.3: Numerical calculation of molecular interferometer lineshape. On the x-axis we scan the magnetic field, and the y-axis shows the probability of the molecules ending up in the F=1 states.

where a is the length of the interaction region between the Raman transition regions, and b is the length of the Raman transition regions. We can now numerically calculate the signal we expect to find in the F=1 state for the parameters used in the experiment. Figure (4.3) shows the results for the population in the F=1 state at the end of the experiment, I have assumed for simplicity that the EDM is zero. In the Figure we see that the interference fringes are "washed out" as the magnetic field is increased. This is due to the velocity distribution of the molecular pulse. The predicted lineshape is for an idealised experiment. In reality all the stages of the experiment are not perfect. For example there is always some background signal in the detector, the pumping stage does not work with 100% efficiency, the magnetic field is not perfectly homogeneous, and the Raman transitions do not always operate with maximum efficiency. To accommodate this, extra parameters will be added to the lineshape in Section (4.3) when we compare with experimental data.

Let us consider what happens if we have not chosen the correct detuning of the Raman beams from the $|\, A^2\Pi_{1/2}\rangle$ state. When the detuning Δ is set too large then one only need increase the power in the Raman beams to compensate. However, if Δ is small, the light is liable to excite to the $|\, A^2\Pi_{1/2}\rangle$ state and there is excessive spontaneous decay from that state. This reduces the interference fringe height

because some of the molecules are lost to other states. Also there is an increase in the background because a small fraction of the molecules decay back into the F=1 ground levels.

4.2 Implementation

Having discussed the principle of the molecular interferometer, I now discuss how the static magnetic and electric fields are produced.

4.2.1 Magnetic Field Hardware

One troublesome aspect of the experiment its extreme sensitivity to magnetic fields, which must be controlled to a level of a few pT. It is also necessary that this magnetic field be homogeneous over the length of the interaction region. We achieve this by using magnetic shields made from highly permeable mu-metal. For a detailed description of how magnetic shields function refer to [70].

We use two layers of magnetic shielding, one outside the vacuum chamber and the other located inside. The outer shield is 140 cm tall, 62 cm in diameter, and approximately 1 mm thick. The outer shield is made from four curved sections that are bolted together to form a continuous cylinder surrounding the beamline. These sections are dropped into the bottom end cap of the shield. The vacuum chamber fits through a hole in the bottom end cap. Further holes in the shields provide access for laser beams and a large hole near the bottom of the shields accommodates turbo pumps. The holes in the shield reduce their effectiveness slightly.

The inner shield is formed from a single cylinder of mu-metal 79 cm tall, 17.3 cm in diameter, and approximately 1 mm thick. The inner shield has two end caps, top and bottom, both with a hole in their centre. These holes allow the molecular beam to pass through. There are also holes for the upper and lower Raman beams to pass through and for electrical connections. The position of these Raman beam access holes with respect to the electric field plates are shown in Figure (4.5) in Section (4.2.2). The magnetic shields are degaussed by an oscillating field produced by a current through a copper coil wrapped around each shield vertically. We degauss the outer shield using a maximum 60 Amp-turns, and the inner shield with a maximum of 20 Amp-turns. When degaussed the two layers of shielding produce a shielding factor of approximately 1000.

We apply carefully controlled magnetic fields which interact with the molecules in the interferometer. These are produced by sets of coils attached to the inside

Plate set	Separation along z-axis (cm)
Bottom Guard	11.85(2)
Centre	11.54(6)
Top Guard	11.51(2)

Table 4.1: The electric field plate separations along the z-axis of the experiment.

of the inner magnetic shield with epoxy. The wires to the coils enter and exit the shield through the top end caps. The most important set of coils produces a field along the z-axis parallel to the electric field. This consists of two long coils attached on opposite sides of the inner magnetic shield approximately 8 cm apart [54]. Figure (4.4) shows these coils and the inner magnetic shield.

Across the molecular beam line the field variation is approximately 1% [54]. This inhomogeneity has the effect of "washing out" the interference fringes, however this effect is negligible compared to the effect from the velocity distribution of the molecular beam. The experiment also has a second coil for diagnostic purposes which produces a field along the y-axis, the other axis transverse to the molecular beam. The currents supplied to these coils are controlled by the computer, using its analog output. Outputs in the range 0 to 5 Volts, are converted to currents in the range -15 mA to 15 mA. For the z-field the conversion from current to magnetic field is 16.5 nT.mA^{-1}, measured using the Zeeman splitting of the ground state hyperfine levels [54]. This means we are able to scan the magnetic field over a range of approximately 245 nT. The resolution of the current supply is 0.4 nT.

4.2.2 Electric Field Hardware

The polarisation of the molecules in an applied electric field sets the upper limit on the electric field strengths required for the experiment. YbF is 72% polarised along the field direction at around 25 kV.cm^{-1} [47]. Above this, very large increases in the electric field are needed to significantly improve the sensitivity of the experiment. Three pairs of electric field plates are currently used in the experiment to achieve such fields.

The electric field plates are made from aluminium which is coated with gold. The gold coating is used because aluminium oxidises to form a dielectric surface layer. The three pairs of plates are called the bottom guard plates, the centre plates, and the top guard plates. The gap between the guard plates and the centre plates is 9.65 mm at the bottom, and 10.65 mm at the top. The separations between the plates are listed in Table (4.1).

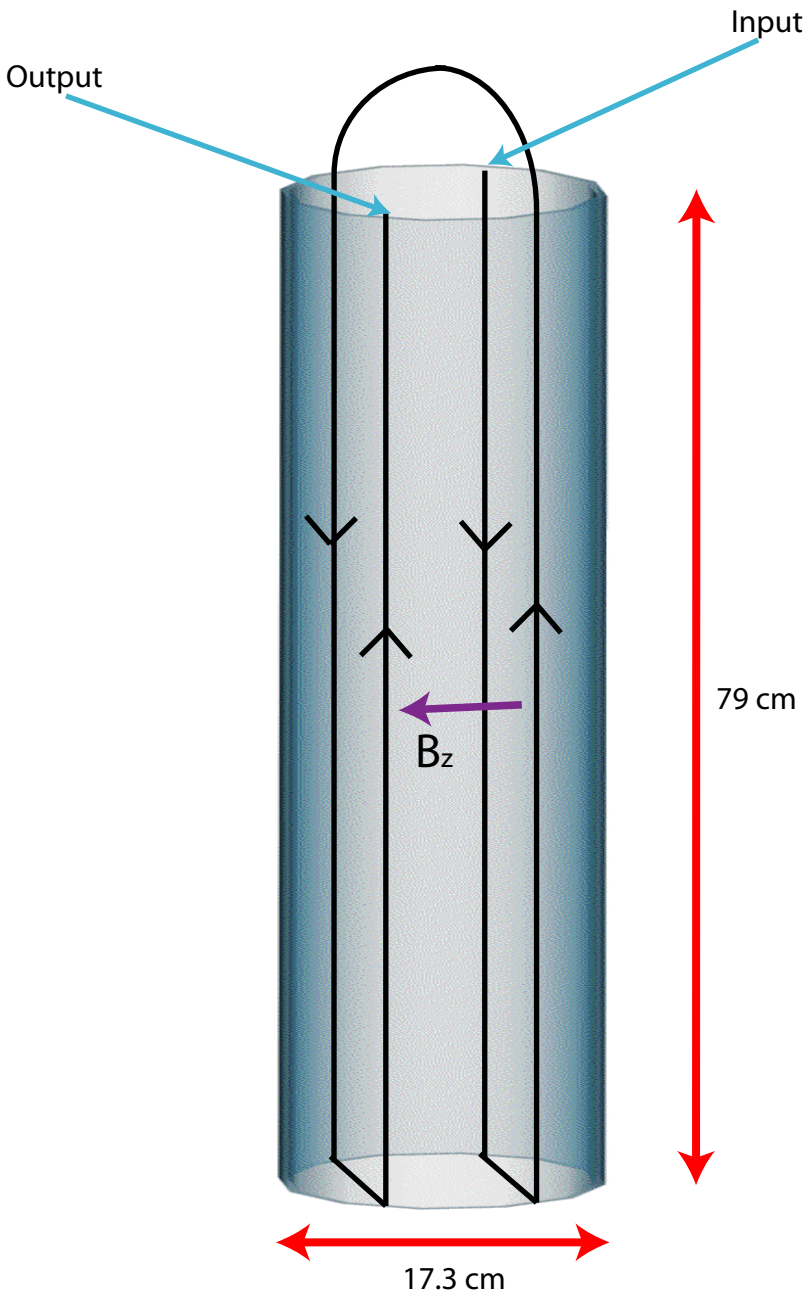

Figure 4.4: The inner magnetic shield is drawn with the coils for producing a magnetic field along the z-axis.

The field plates are supported by a frame, made from two aluminium plates whose sides are machined parallel and flat. Figure (4.5) shows the rear support plate with the electric field plates in front of it. Near the top we see the top guard plates and the top rf loop around them. The access hole for the upper Raman beams is also shown in the support plate. Further down the centre and bottom field plates are shown along with the bottom rf loop. Again the Raman access hole is shown. This frame rests on the bottom of the inner magnetic shield via ceramic locators. At the top of the frame are Teflon spacers which rest against the inner walls of the shield. This provides a stable support to hold the field plates. The electric field plates are connected mechanically to the frame with Torlon and ceramic rods, see Figures (4.5), that run through holes in the field plates and fit snugly into the support plates. The guard plates have two ceramic rods for each plate and the centre plates have six Torlon rods for each plate.

Because the experiment is very sensitive to small magnetic fields along the z-direction, the plates and support structure must be designed in such a way as to minimise leakage currents, especially those producing such magnetic fields. With this in mind the support structure was designed so that the electric field plates do not have any direct mechanical connections between them. Also ceramic spacers are used between every metal-to-metal mechanical connection and resistors are placed such that the leakage path is controlled. This path has been chosen such that the magnetic fields produced are along the x- and y- directions which the experiment is very insensitive to.

In order to achieve large electric fields without electrical breakdown it is necessary to condition the plates. This involves a small amount of argon gas being leaked into the vacuum chamber. Typically the argon pressure is in the range between $10^{-4} - 10^{-5}$ mbar. The plates are charged, to low voltages at first, and the field direction is flipped, approximately every 30 seconds. The leakage currents are monitored and as they decrease, the voltage applied to the plates is increased. This procedure is followed until the leakage currents at the desired operating field are less than 1 nA. If the field plates are taken out of the vacuum for modification or inspection, this procedure normally takes around three days to complete. However, the first time the plates are put into the vacuum the conditioning takes longer. This process is thought to work by removing high points on the microscopically rough surface of the plates. Since they are points of high electric field, they are subjected to particularly strong argon ion bombardment and are preferably ablated.

The guard plate power supplies are Bertan 602C-150P and Bertan 602C-150N. A further two supplies charge the centre region plates (Bertan 612A-500P, and 205A-

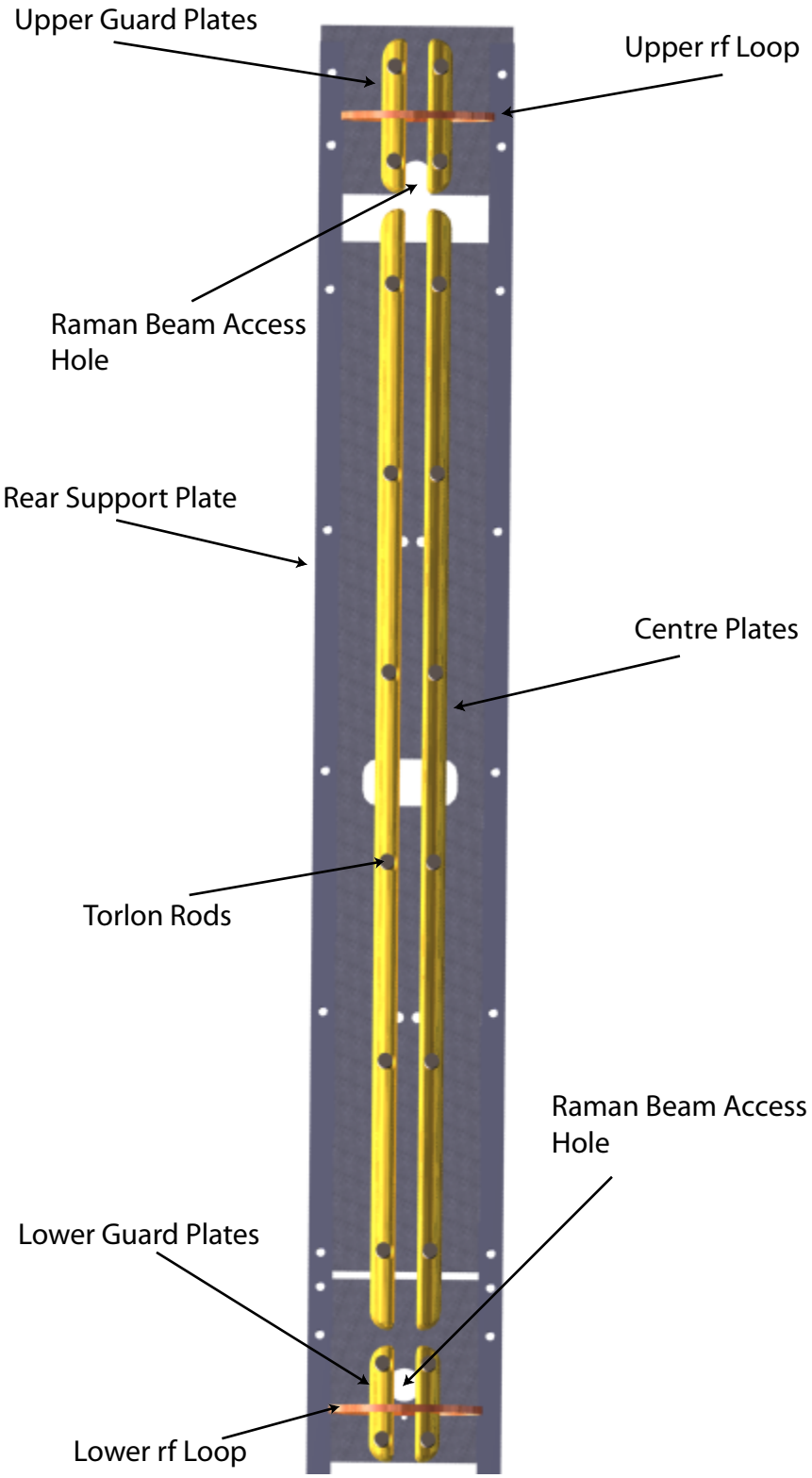

Figure 4.5: This Figure shows the field plates, the position of the laser access holes through the magnetic shields, and the rear support plate of the support structure.

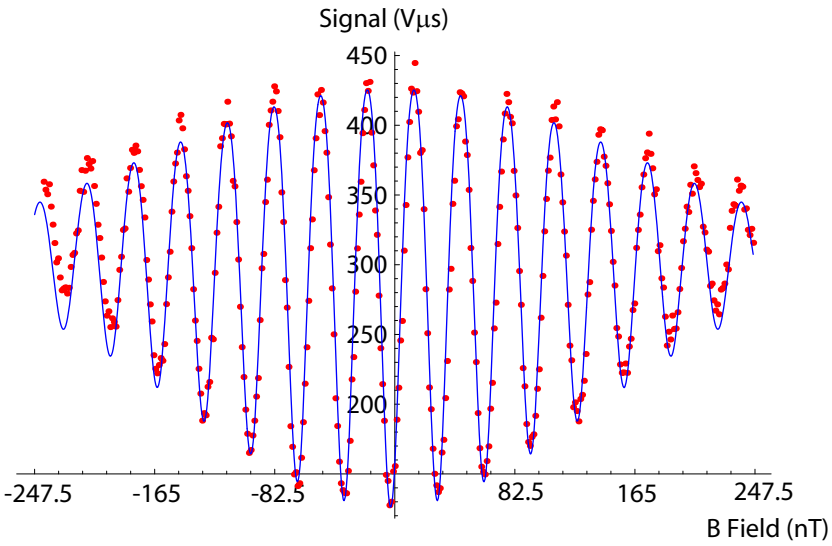

Figure 4.6: Interference signal

50N). These supplies are not directly connected to the electric field plate. They connect first to a relay box which allows the field to be reversed under computer controlled, then through resistors to limit charging currents that can polarise the magnetic shields, and finally through vacuum feedthroughs to the plates. The centre region voltage supplies are also connected to two leakage current monitors so that currents as small as one nA can be monitored when the plates are fully charged. This is an important check for systematic problems described in Section (6.2).

4.3 Characterization

The first steps towards measuring the interference signal, described in Section (4.1), are to optimise the molecular beam, the laser pumping, and the rf or Raman transfer efficiencies. With these stages optimised it is normally just a matter of plugging in the computer-controlled current supply to the z-axis magnetic field coils and scanning over a reasonable field range to see the interference fringes.

Figure (4.6) shows a typical interference lineshape. In this scan the current range is at the maximum of the current supply -15 to 15 mA. We see that the population in the F=1 state oscillates as the magnetic field is scanned. With this magnetic field range one also clearly sees a decay of the fringe visibility as the magnetic field increases in either direction. This is due to the molecular velocity distribution of the supersonic source. As discussed in Section (4.1) the rf and Raman model

interference lineshapes are exactly the same provided that the detuning Δ allows the upper $|\ A^2\Pi_{1/2}\rangle$ state to be eliminated. The lineshape for the population in F=0 state is [29],

$$\overline{P}_0(B) = \int_0^\infty f(v)\left[cos^4(\frac{\pi}{2}\frac{v}{v_m}) + cos^2(\frac{\mu_B B}{\hbar}\frac{a}{v})sin^4(\frac{\pi}{2}\frac{v}{v_m})\right]dv \tag{4.10}$$

where $f(v)$ is the velocity distribution, equation (2.7) of Section (2.2), v_m is the mean velocity of YbF gas which is found by fitting to the time of flight profile, $a = 0.625$ m is the coherence length between the Raman transitions, and B is the magnetic field. The population in the F=1 state is simply $\overline{P}_1 = 1 - \overline{P}_0$. However to get a reasonable fit with the data we modify this to,

$$I = N + Q\left(1 - \overline{P}_0(B-\delta)\right)\left(1 - A\overline{P}_0(B-\delta)\right) \tag{4.11}$$

where N is the signal background, Q the peak to peak amplitude of the curve, δ the centre zero offset, and an asymmetry, A, describing the asymmetry of the peaks and the troughs.

Comparing the data of Figure (4.6) to the lineshape we see an excellent fit over many fringes. However, the lineshape agrees less well at the very largest currents. This is probably due to the fact that in the model the magnetic field interaction has only been included in the centre region and not in the transition regions. The magnetic field in the transition regions detune the Raman light from the F=0 to F=1 transition frequency. In large magnetic fields this detuning is big enough to washing out the interference because the F=1 levels become less populated as the field increases. This is rather similar to the Ramsey interference lineshape in large magnetic fields [53]. There are also other effects at work here relating to the target conditions changing over the scan and the temperature variation in the YbF pulses themselves. These effects can cause changes in the total signal and change the widths of the YbF pulses. These effects are particularly difficult to measure and not understood well enough theoretically to model.

Another interesting feature of the interference data comes from the time of flight profiles. Since we measure time of flight distributions for each point in the interference lineshape we can look at the molecules arrival time at the detector against the applied magnetic field. Figure (4.7) shows this for the data shown in Figure (4.6). The x-axis of the plot is the arrival time of the molecules at the detector. The y-axis shows the applied magnetic field. The white regions indicate that molecules in the F=1 state are detected, with the brightness proportional to their number. A cross-section along the x-axis would reveal the time of flight profiles. A slice along the y-axis would reveal the interference signal.

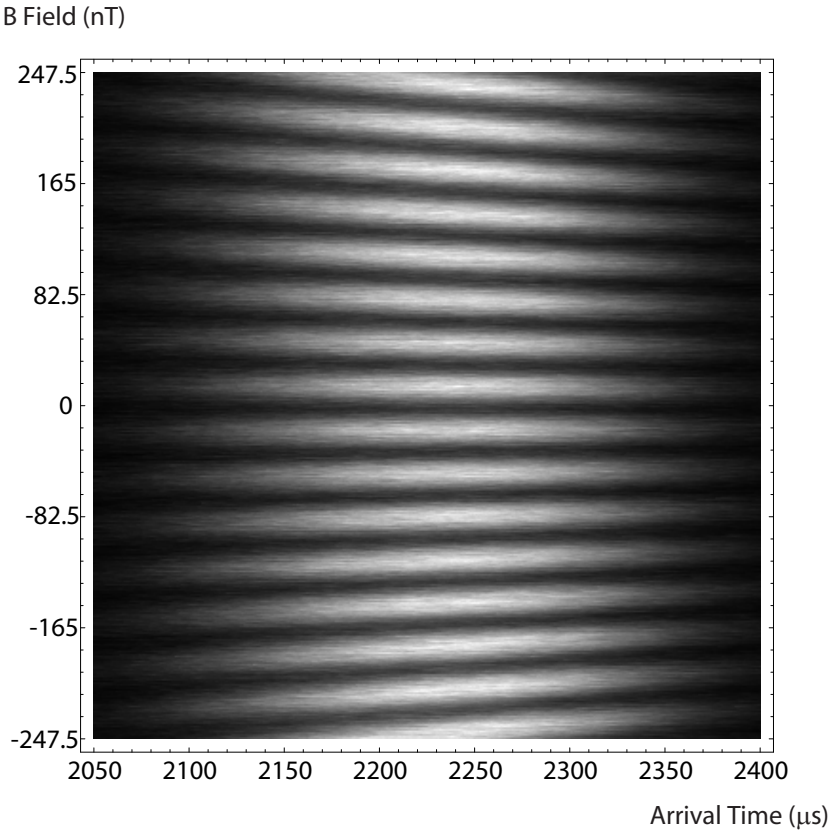

Figure 4.7: Interference signal. The arrival time is plotted on the x-axis, and magnetic field amplitude on the y-axis. The light regions indicate that F=1 molecules are detected, with the brightness of those regions indicating their number.

An interesting feature of the plot is that molecules arriving at 2100 μs give interference fringes separated by approximately 35 nT. However, the molecules arriving at 2350 μs have fringes separated by approximately 30 nT. The explanation for this asymmetry is that the faster molecules spend less time in the magnetic field, than the slower molecules, collecting less phase per unit magnetic field than the slower molecules. This means that the "pitch" in the interference lineshape is higher for the slower molecules compare to that of the faster molecules.

Chapter 5

Principles of the EDM Measurement

The previous chapters have introduced the experimental hardware needed to measure the EDM of the electron using YbF. In this chapter I describe in detail how this is used to perform the measurement. I first describe a simplistic EDM measurement that could be performed with the molecular interferometer. I use this example to highlight why such a scheme is not used and illuminate the solutions to the problems identified. This motivates an in depth analysis of noise in the experiment and how this noise is dealt with. I then discuss how the control computer is used for data acquisition and how the EDM of the electron is extracted from the data acquired.

To measure the electron EDM we apply an electric field either parallel or anti-parallel to a magnetic field. In a simple approach one may set the experiment up in one of these two states, scan the magnetic field and record the interferometer output, then switch the direction of the electric field and measure the interference signal once more. The EDM could be inferred from the difference between the two signals, since it simply makes a small shift between them. This is indicated in Figure (5.1) by the red and blue curves which are for the two electric field states. This method was used in [54] as a primitive EDM measurement. As noted by the author of [54], this method has many faults, one of which is that it is sensitive to magnetic field drifts as a source of systematic error. Ignoring this, let us concentrate on the statistical sensitivity of the method. At the turning points of the interference pattern the derivative is zero and hence the EDM difference signal is zero. Therefore, time is wasted taking data there. A more efficient strategy is to spend most of the time taking data on the sensitive regions on the interference curve where the slope is large, as shown by the points “a” and “b” in Figure (5.1). The EDM interaction has

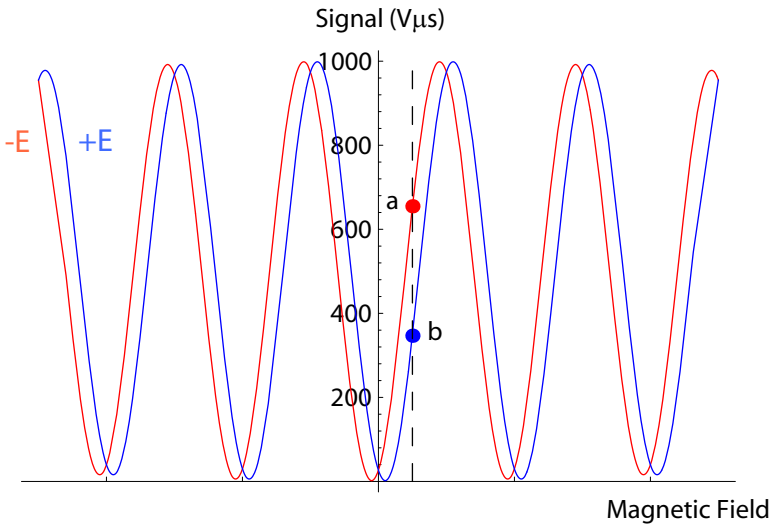

Figure 5.1: This shows the interferometer signal for opposite electric field states. The EDM interaction has been hugely exaggerated.

of course been hugely enhanced to make the signal difference visible in the Figure.

To convert the change of signal size to a corresponding magnetic field and hence to an EDM, one must know the gradient of the interference curve. This is measured by making a small known step of the magnetic field and measuring the signal change. The size of the step is chosen such that both points are on the linear part of the curve. One may also reverse the magnetic field so that the gradient of the interferometer signal becomes negative. This is equivalent to reversing the electric field, since the EDM shift reverses direction. Therefore, there are four applied magnetic fields where the interference signal is measured, two on either side of the central minima, each of these is called a "state", of the experiment. With the two electric field states this makes a total of eight states of the experiment. Using these states, possibly the simplest way to take data would be to spend equal amounts of time in each of the eight states, switching between them one after another.

In order to find the statistical sensitivity of the experiment we need to know the number of photons collected by the PMT. In current mode the PMT outputs a current proportional to the photon count rate, this is then converted into a voltage by the PMT amplifier. The PMT amplifier circuit diagram is shown in Figure (5.2). After the input the current from the PMT is converted to a voltage. This voltage is amplified by the operational amplifier and inverted. The background is cancelled out with the offset potentiometer shown in the figure. The voltage is then amplified again. This second operational amplifier's gain can be chosen. The voltage from

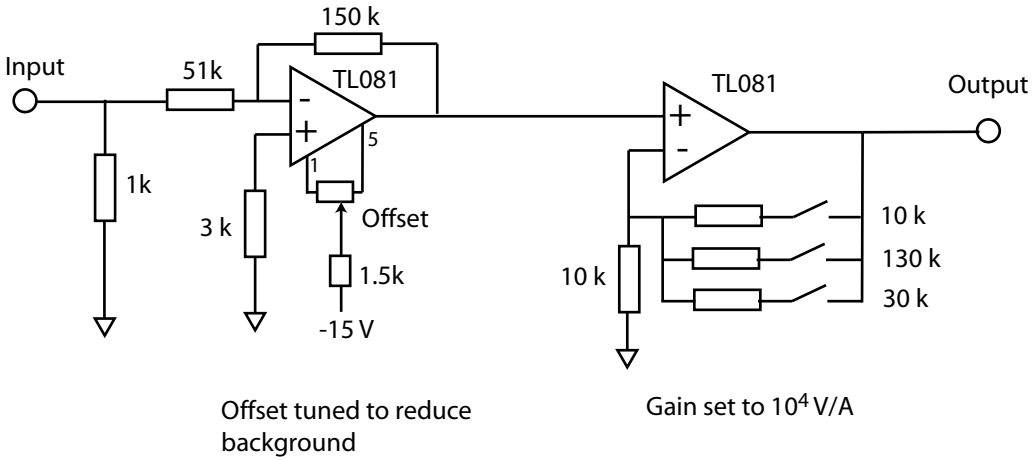

Figure 5.2: This is a circuit diagram of the PMT Amplifier.

the amplifier is read by the control control computer. In order to calibrate this we shone the probe laser through the vacuum chamber and scattered some of the light into the PMT at a steady rate. First we ran the PMT in pulse counting mode and measured the count rate, then compared we this to the voltage from the PMT amplifier. This comparison was made for a range of laser light intensities.

Figure (5.3) shows the calibration curve. At low count rates, the curve is linear, showing that the PMT voltage in current mode is indeed proportional to the photon count rate. We also see some saturation of the PMT count rate at high rates. In the figure, the non-linear curve is used to show this. There are three main saturation effects that could limit the performance of the PMT measurement system. In pulse counting mode the electron pulses, that the PMT produces in response to a photon, are sent to a discriminator which amplifies the signal and turns it into a logic pulse. The width of the electron pulse is of the order of 5-10 ns, which is typically much smaller than the width of the discriminator pulse, which in this case is around 50 ns. During this 50 ns the discriminator will not response to other electron pulses, therefore this time is called the "dead time". If the dead time of the discriminator is τ, then if the interval between two successive electron pulses is less than τ the second pulse will not be detected. If the interval is greater than τ the second pulse will be detected regardless of whether the previous pulse was detected or not. Since the photons arriving at the PMT are governed by Poisson statistics, the electron pulses arriving at the discriminator correspond to a Poisson probability distribution. The probability that the interval between two successive pulses is greater than τ is $e^{-r\tau}$, where r is the average number of pulses arriving at the discriminator per

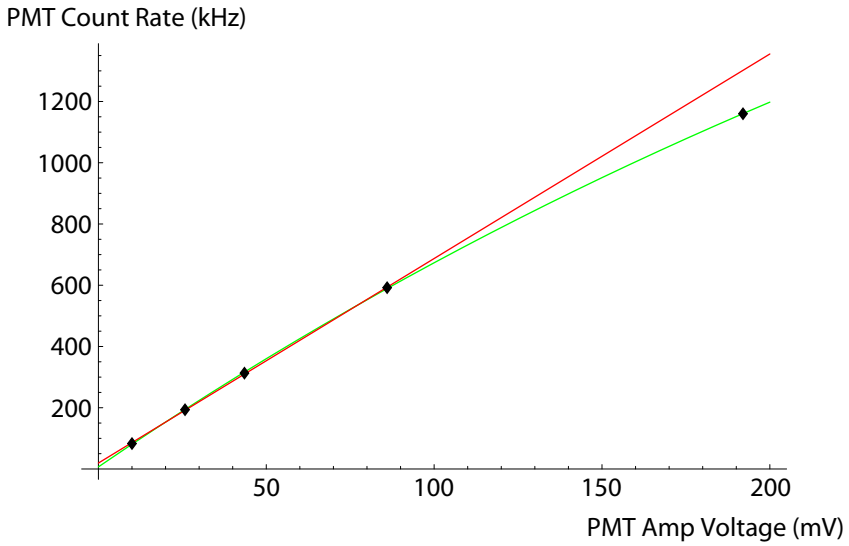

Figure 5.3: This is the calibration curve for the PMT amplifier. The green curve is a non-linear curve to guide the eye. The red curves is a linear fit to the data, excluding that last point, to find the calibration.

second. Therefore, the ratio of the measured count rate, R, to the real count rate, r, is equal to $e^{-r\tau}$. Hence the measured count rate is [6],

$$R = re^{-r\tau}. \tag{5.1}$$

This means that at high count rates the PMT will saturate because it will record a lower count rate than the real one.

In the current mode of the PMT the saturation is of a different nature. At high count rates space charge becomes a problem because the electrons produced from a photon count shield the potential that the other electrons, from subsequent pulses, interact with. Also at high rates the current that the PMT produces at its final stage is large enough to produce a sizable voltage drop across its resistor chain. This means that the potential at each stage of the PMT becomes smaller, reducing its overall efficiency. These two saturation effects occurs at a much higher count rates and do not limit our experiment.

To calibrate the amplifier response correctly we fit a linear function to the points of the calibration curve in the linear region. Since the last data point in Figure (5.3) is not in the linear region I neglected it in the calibration and used the remaining points. With this method we found the conversion between PMT count rate and the amplifier output was 0.148 mV.kHz^{-1}. This leads to a calibration between Vμs and photon counts of 0.148 Vμs per photon count.

The sensitivity of the experiment is fundamentally limited by statistical shot noise. This can be estimated by calculating the photon-count difference between points "a" and "b" of Figure (5.1). Using a simple model of the interferometer, described in Section (1.3.2), the interference signal count rate can be written as $R = R_0 sin^2(\phi_B + \phi_e)$, where R_0 is the height of the curve in Hz, and ϕ_B and ϕ_e are the phase shifts due to the Zeeman and EDM interactions respectively. If we measure the signal at points "a" and "b" for equal amounts of time T/2, the photon count difference due to the EDM will be,

$$S_{EDM} = \frac{T}{2}R_a - R_b = \frac{TR_0}{2}[sin^2(\phi_B + \pi_e) - sin^2(\phi_B - \phi_e)]. \tag{5.2}$$

The steepest slope of the interferometer signal occurs when $\phi_B = \pi/4$, around this point the slope is linear. Therefore,

$$S_{EDM} = R_0 T\phi_e = R_0 T\frac{d_e E_{eff}\tau}{\hbar} \tag{5.3}$$

where τ is the coherence time. The statistical uncertainty on this signal will be approximately $\sigma = \sqrt{TR_0/2}$, because the background interference signal is much larger than the EDM signal and the addition background from laser scatter. By equating the uncertainty and the EDM signal we can find the minimum EDM that we could discriminate from zero with 1σ uncertainty in time T,

$$d_e = \frac{\hbar}{\tau E_{eff}}\sqrt{\frac{1}{2R_0 T}}. \tag{5.4}$$

The typical height of the interference signal is about 1000 Vμs and the coherence time is approximately $\tau = (0.675/550)$ which is the distance between the Raman transitions divided by the typical mean velocity of the YbF pulses. This means in one day of integration time, and the electric field set to the normal 16 kV/cm we can measure an EDM with an uncertainty of,

$$\sigma_{d_e} = 9.6 \times 10^{-28} e.cm. \tag{5.5}$$

This sensitivity is approximately 40 times better than the previous EDM measurement using YbF, and is about the same statistical sensitivity as the experiment with the current best upper limit on the electron EDM [56].

5.1 Non-Statistical Noise

In addition to shot noise, there are many other sources of noise that we must examine, see Table (5.1). Since we produce YbF using carrier gas pulses we must estimate

Noise Source
Intrinsic noise from Poisson statistics
PMT
PMT Amplifier
Gas Pulses
Magnetic Field
YAG Laser Timing and Intensity
Target Conditions
Pump/Probe Laser Frequency and Intensity
Raman AOM Coupling
Electrical Pickup

Table 5.1: Noise sources

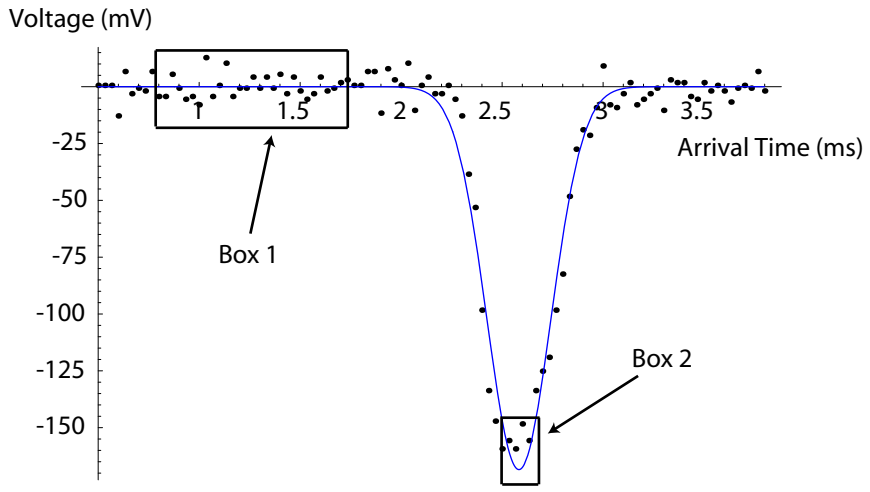

Figure 5.4: This is the same data shown in Figure (2.6). The box labelled "Box 1" shows the area we used to estimate the noise coming from the FIG measurement-system. This can be compared to the variation of the points in the second box labelled "Box 2". This allows an estimate of how much of the peak variation is due to the gas pulses, and not the intrinsic noise of the FIG measurement-system.

their shot-to-shot variation in order to access whether they limit the experiments sensitivity.

Figure (5.4) shows the same FIG data as Figure (2.6). The boxes indicate the regions of interest for analysing the data for the variation of the gas pulse signal. First we need to estimate the intrinsic noise of the FIG measurement-system and then compare it to the peak-to-peak variation of the gas pulse signal. Box 1 of the figure indicates the region of data which was used to find the instrumental noise. The standard deviation of the data within this box was calculated and compared to the standard deviation of the data within box 2. This showed that there was a detectable shot-to-shot variation. Further analysis was then performed to estimate whether this variation could be detected over the statistical noise of the YbF detection method. This was estimated by assuming that a typical FIG signal is proportional to a typical YbF signal. Using this comparison we found that the gas pulse variation was not contributing to the interferometer's output noise over the variation expected from the photon counting noise intrinsic to the LIF detection.

The next important source of noise comes from the magnetic environment in the laboratory. Since the interferometer is very sensitive to magnetic fields it is also sensitive to fluctuations of these fields. To measure the magnetic field in the laboratory we used a Flux gate magnetometer, Bartington Mag-03MCL100, and recorded the field over many hours.

We have used two magnetometers one to measure the magnetic field outside both magnetic shields and another to measure the field between the shields. Unfortunately the flux gate magnetometer is itself highly magnetic and therefore can not be put inside the inner magnetic shield when EDM data is being taken. This is because strong magnetic gradients and fields cause problems with the interferometer. The magnetometer outside the both magnetic shields measured the magnetic noise in the laboratory. From this data we analysed the frequency spectrum of the magnetic noise to find "quiet" frequencies which could be taken advantage of by using a phase sensitive EDM measurement technique, see Section (5.1.1).

Figure (5.5) shows the magnetic field, recorded by the outer magnetometer, as a function of the field's frequency components. The data was recorded while all the equipment used for taking EDM data was operating in the normal fashion. The main features are the large "spikes" of magnetic field noise around 50 Hz, the mains electricity frequency, and its harmonics. Figure (5.6) shows a section of the above Figure between 9 and 11 Hz. The peaks in this plot are from unknown sources. The magnetic field was sampled by the magnetometer at 500 Hz over a 24 hour period. The amplitude of the component of the magnetic field at 10 Hz was 13 nT, this is

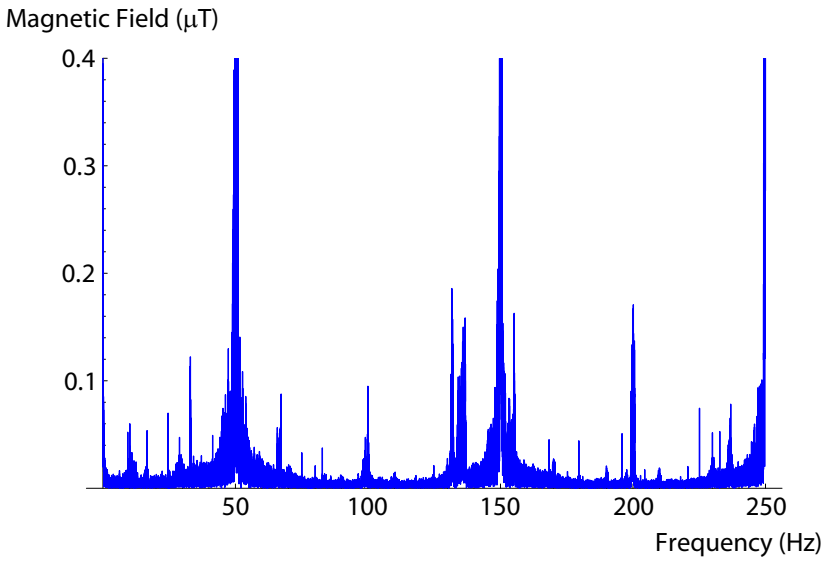

Figure 5.5: This shows the magnetic field frequency components outside the shields from 0 to 250 Hz.

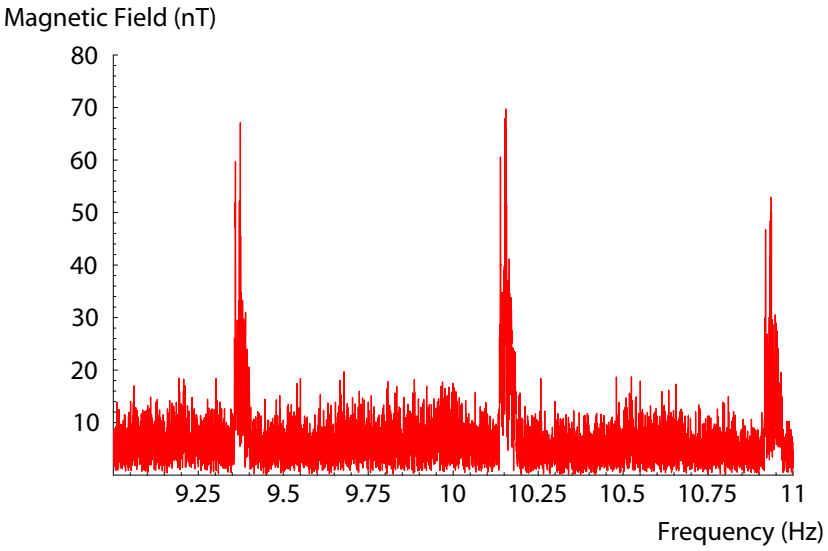

Figure 5.6: This shows the magnetic field frequency components outside the shields from 9 to 11 Hz.

compared to 2 μT at 50 Hz. This means that if record data at 10 Hz we can take advantage of the low noise. The next Section will describe how this is achieved.

5.1.1 Non-Statistical Noise Suppression

Phase sensitive detection is a method of reducing the non-statistical noise on the output signal of a system. By modulating the input of the system and recording the component of the output at the modulation frequency the noise can be reduced. This is because we are only sensitive to noise on the output around the modulation frequency. For a $1/f$ noise spectrum the noise at low frequency is large, however, at higher frequencies the noise becomes dominated by a baseline of statistical noise. To reduce the noise in this case we chose the modulation frequency so that it is high enough so that we are only limited by statistical noise. In practise there are often noise spikes at specific frequencies in the spectrum, at the mains frequency for example, and these frequencies and their harmonics should be avoided.

We use a phase sensitive detection scheme using a digital modulation [25], recording data in the eight states of the experiment. If the eight measurements are taking in a well chosen order we can automatically suppress some drifts and backgrounds. For example if the data contains a background that does not depend on the magnetic field, say, then one may take half the data in one state of the magnetic field and the other half in the other state. Then when one analyses the data it is possible to extract the signal that changes with the switch. Therefore, the background is removed from the magnetic field "analysis channel". Suppose next that the background has a linear drift. Without any parameters being switched a linear drift of the signal would look like a change in the interferometer output produced by a phase shift. However, if we record data for a quarter of the time in one magnetic field state, then switch to the opposite state for half the time, and finish for the remaining quarter in the original state we can eliminate the effect of the linear drift from the analysis. In this way more complicated switching patterns can be added to remove higher order drifts from the data in the analysis [25].

To describe the way in which EDM data is taken I must also introduce the terminology we use for this. The integrated signal over one YbF pulse is called a "Point", which has about 800 μs of gated YbF data and takes in total time of 10 ms to complete. A group of 1024 Points is a "Block" and a collection of Blocks in the same configuration of the apparatus is called a "Cluster". A complete switching waveform pattern is contained within a Block and each Block is analysed for the EDM of the electron amongst other things. Each Block therefore represents a unit

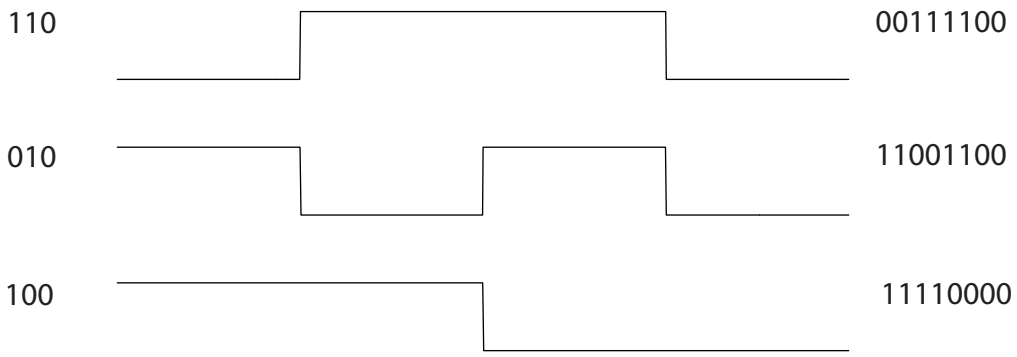

Figure 5.7: This shows some example 8 bit waveforms with their shorthand notation (left) and full notation (right).

of EDM data.

Within each Block the magnetic and electric fields switch direction according to a predefined waveform. The waveforms are made from a basis of orthogonal square waves with different frequency components. The waveforms can therefore be represented as a binary string with as many bits as there are points in a Block. Figure (5.7) shows some example waveforms. The square waves which make up the waveforms have periods of 2^n and a length equal to that of the Block, N. Where n is the number of basis components of the waveforms. A "waveform code" is used to specify the basis components of each waveform. For example, in Figure (5.7) the waveform code "100" specifies that the corresponding waveform should have a period of $N/(2^2)$, where the number of points, N, in this example is 8. The waveform specified by "110" has a waveform component with a period of 8/4, and a component with a period of 8/2. The waveform codes can be combined by using the Exclusive-OR (XOR) operation. For example, "100" and "010" combine to form the code "110", as can be seen in the Figure.

Each block of EDM data can be analysed for signals correlated with any of the switching waveforms and any combination of the switching waveforms. This is performed by taking the dot product between the signal and the waveform. That is to say the part Q_S of the data in a Block correlated with the waveform S is,

$$Q_S = \frac{1}{N}\sum_{i=1}^{N}(-1)^{S(i)}D(i) \tag{5.6}$$

where $D(i)$ is the i^{th} data point of the block, $S(i)$ is the i^{th} bit of the waveform, and N is the number of Points in the Block. The data can be analysed for many different effect, some of which highlight systematic problems. Table (5.2) lists the parameters which are switched in the experiment.

Switched Parameters	Waveform Name
Electric Field Direction	S_E
Magnetic Field Direction	S_B
Magnetic Field Amplitude	$S_{\Delta B}$

Table 5.2: Switched parameters and their waveform names

Switched Parameter	Waveform Code
S_E	1100000000
S_B	0000011011
$S_{\Delta B}$	1100110111

Table 5.3: Switching Waveforms

The switching patterns used in the experiment are listed in Table (5.3) and the analysis channels in Tables (5.4) and (5.5) of Section (5.3). The physical significance of these channels will become apparent in Section (5.3) and Chapter (6). The switching patterns have been chosen to limit the noise in the EDM analysis channel over the fundamental shot noise limit. By examination of the noise at the output of the interferometer we found that at 10 Hz the noise is only a small factor, of $\sim$1.2, over shot noise. Therefore, the switching patterns should have components up to around 10 Hz. Also to remove the effects of drifts from the source and magnetic field in the output the patterns should have as many components as possible.

On close inspection of Table (5.3) one finds that the electric field switch has slower frequency components than the other channels. This is because there is some dead time associated with each switching channel. The dead time for the magnetic field switching is insignificant, however the dead time involved for the electric field switch limits the frequency at which it can be reverse. This is because the charging/discharging currents involved when ramping the electric field up and down must not polarise the magnetic shields to avoid systematic problems. This means the charging of the plates must be done over about a 10 second time frame, and similarly for the discharging. Overall each reversal of the electric field takes around 20 seconds, therefore it is necessary to switch the electric field less often than the magnetic fields. In Table (5.4), of Section (5.3), one find that the "EShift" analysis channel is effected by this, together with our ability to discriminate against drifting magnetic fields. We sacrifice signal to noise on the "EShift" channel in order to maintain a good duty cycle of the experiment, since we are fundamentally limited by counting statistics. Including this dead time a Block takes exactly 125.4 seconds to complete.

5.2 Computer Control and Current Supply

In this section I describe the computer system used to control the experiment and to keep track of these complicated switching patterns.

The main function of the computer control is to orchestrate the many devices needed to take EDM data. Firstly the valve should pulse open and at a set time afterwards the YAG laser must ablate the Yb into the carrier gas. Then, the rf or Raman transitions should be driven and the detector gated to measure the YbF signal. To perform these functions the computer uses a National Instruments NI PCI 6534 pattern generator board. As the name suggests the board sends a pattern of pulses to its digital outputs. Each digital output is connected to a device of the experiment. For example, one of the digital outputs is connected to the valve driver which fires the valve when it receives a pulse from the computer. The pulse should be of the length that the valve is required to be open for. The pattern generator has thirty two digital lines in total which are coordinated by a computer software written in the C# programming language.

The purpose of the computer software is to write a pattern of digital pulses to the pattern generator which will control the experiment by sending the pulse sequence over the digital lines. An example pattern is shown in Figure (5.8), which shows the sequence of events in the experiment. First the valve is opened, the YAG flash lamps are fired, and the Q-Switch triggered. Sometime later the PMT is gated. After sending the pattern to the pattern generator board the software waits for the YbF fluorescence data to arrive. The data is collected by a National Instruments NI PCI 6024E data acquisition board. This board has sixteen analog input lines, two analog outputs, as well as some digital I/O lines and counters. The main input line is connected to the PMT amplifier. When the detector is gated by the pattern generator it outputs a current to the amplifier which converts it to a voltage and this is read by the analog input. The software reads in the analog inputs and stores them appropriately. The data inputs are the YbF signal, and the signal from a magnetometer measuring the magnetic field between the shields.

There are two main programs that we use to run the experiment. Each of these programs uses a common resource for building patterns and performing I/O tasks. “ScanMaster 2k5” is the program used to setup the experiment. We use this program to optimise the YbF signal, scan the rf/Raman transitions and the interferometer signal. The function of the program is to scan various outputs and read in the inputs for each point of the scan. At the start of a scan the program sets up the pattern generator with the pattern the user defines for the whole of the

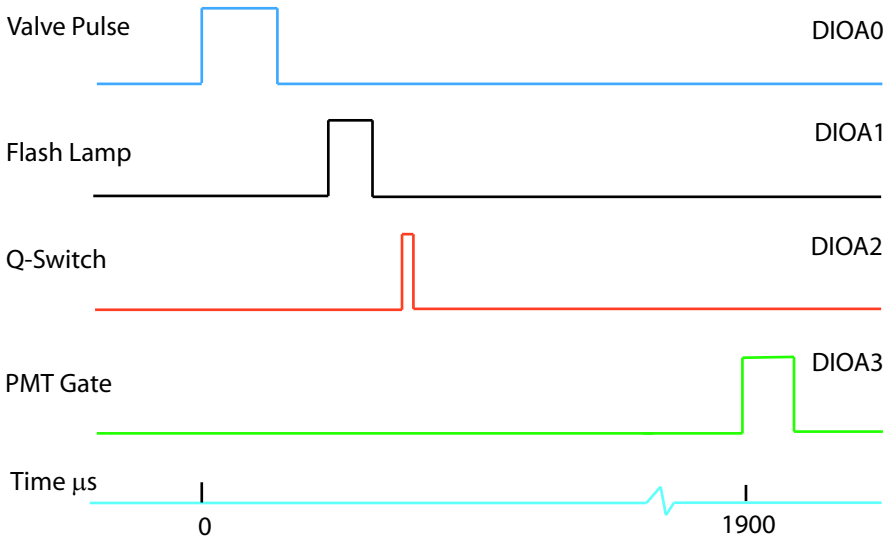

Figure 5.8: An example pattern from the pattern generator. The digital line for each device is labelled with the prefix "DIO"

scan[1]. It then scans a parameter of the users choice and inputs data. If the user has not interrupted the scan, the next scan is loaded to the pattern generator and so on. When the user stops the scan the averaged data can be saved. There are some subtleties due to hardware constraints, for example, the YAG laser has some dead time to warm up so it is run continuously between scans. This means that the new scan pattern is loaded as the previous one is still running. It is possible to perform this because the pattern generator is double-buffered.

The parameters loaded into ScanMaster are shared with the other main program called "BlockHead". This program is used to take a Block of data. These two programs use common code for the pattern generator and also communicate with a third program which is called "EDMHardwareController". This program controls the electric field state and voltage, and the rf/Raman centre frequencies. To take EDM data the electric field and rf/Raman frequencies are set with the hardware controller, Blockhead then commands ScanMaster to load a pattern for the whole Block into the pattern generator with the parameters for the YbF beam. The pattern generator sets the experiments going and at the end of the Block the YbF time of flight profiles which were acquired are saved, as well as the magnetometer data. The program then loops around this structure to acquire a Cluster.

One important aspect that I have overlooked thus far is that the current that

[1]For some scans the pattern generator is reloaded at every point of the scan.

generates the magnetic field for the experiment is supplied by a different current supply then the one used for measuring the interference signal, described in Section (4.2.1). The reason for using a different current supply for taking EDM data is that the magnetic field should reverse direction and change magnitude accurately to avoid systematic effects. This puts some constraints on the current supply used. The critical issue is that the magnetic fields reverse symmetrically to below 25 fT, which converts to a systematic EDM of below 10^{-28} e.cm. We can related this to a current difference, in the reversal, of less than 1 μA out of 460 μA.

With this in mind a current supply was purposely built and the circuit diagram is shown in Figure (5.9). The main feature of this circuit is that the voltage reference and the potentiometers are very stable. The inputs to this circuit are connected to the computer output board by fibre optical connections. This eliminates any electric noise on the input lines and also prevents the input signals from changes in different states which could cause a systematic problem. Starting on the left of the circuit, the input light is converted into TTL logic signals which control the main digital switch, labelled in the figure. The inputs to be controlled by this switch are the voltages V_c, and V_Δ which are set by their respective potentiometers. V_c sets the main current used to take data on the steepest slope of the interferometer signal, and V_Δ sets the magnitude step used to calculated that slope. The switch controls whether or not the input voltages will be inverted or not. After this stage, the voltages are added together with a bias voltage, V_{bias}, and this sum is converted into a current. To make sure that this current is stable, another operational amplifier is used maintains the output current which is sent to the field coils. This supply together with the z-coils produces the four magnetic field states used in the experiment, these are listed in the next section.

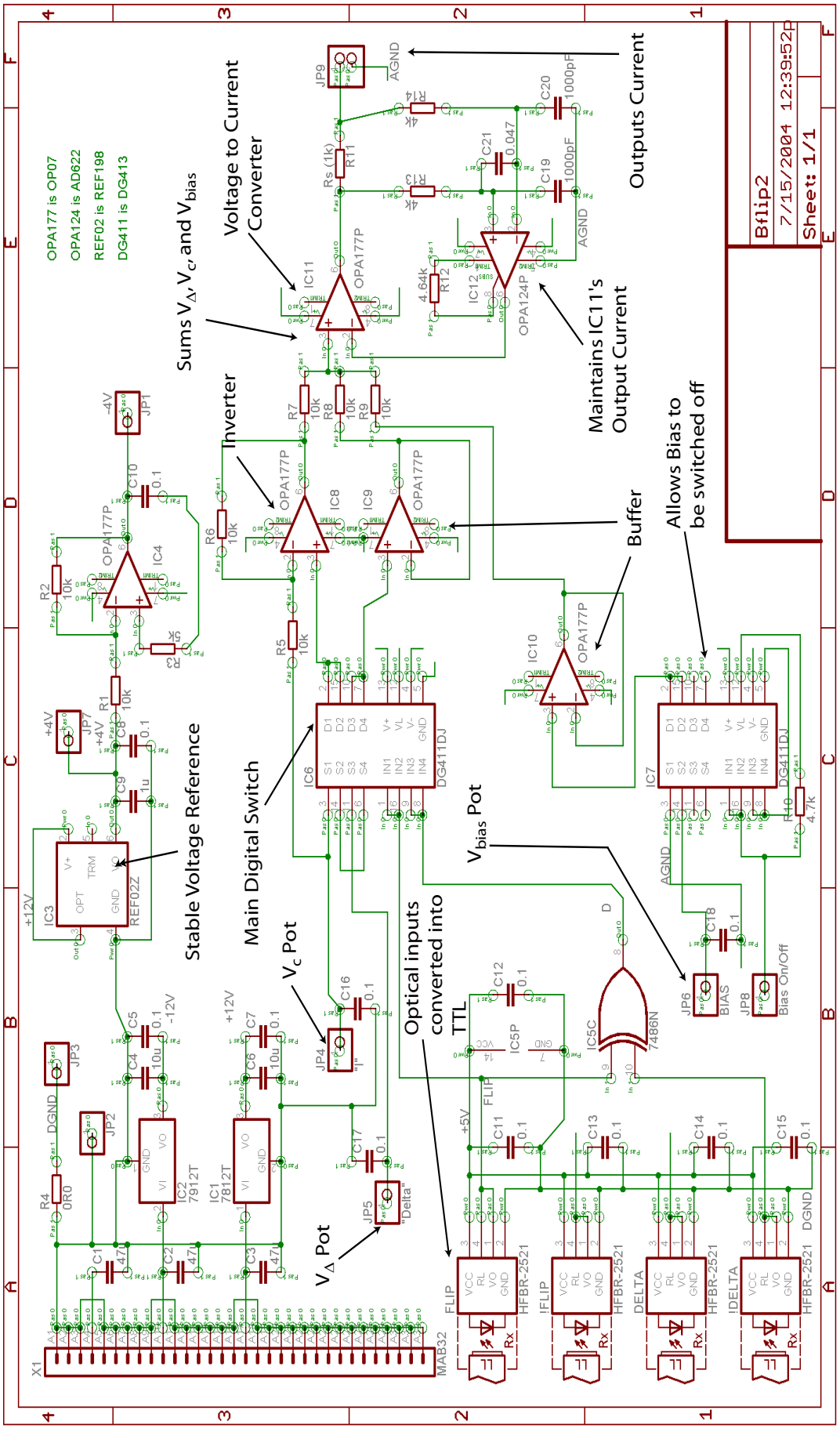

Figure 5.9: This is a circuit diagram of the current supply used for taking EDM data.

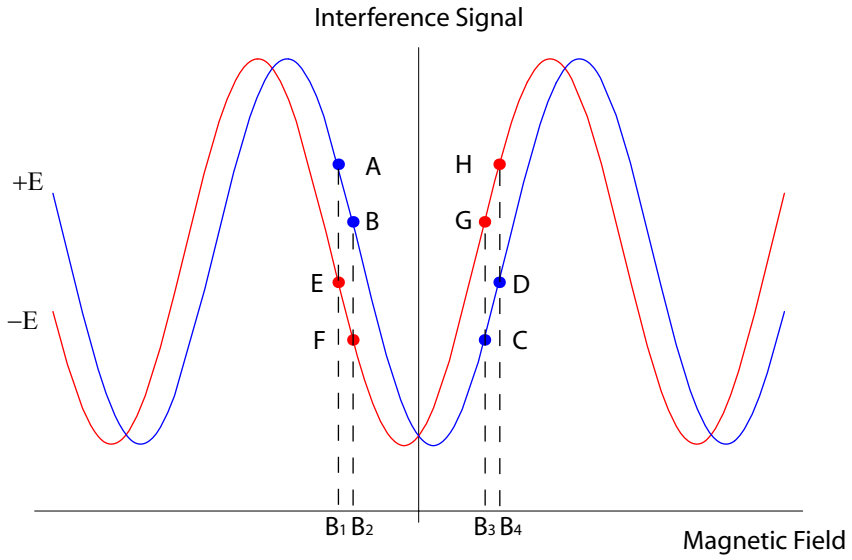

Figure 5.10: This shows two interference curves for each electric field state and the magnetic field states for taking EDM data. The data points are labelled and the physical significance of the combinations of these data points is explained in the text.

5.3 Data Analysis

The analysis of the EDM data taken in the above scheme is described below. Figure (5.10) shows the points on the interference curve where data is taken. The various possible combinations of the data points provide information on a variety of different physical effects. The complete set of analysis channels are defined in Table (5.4) with respect to Figure (5.10). A brief comment on their significance is shown in Table (5.5), for a fuller description of these analysis channels refer to [29].

When the experiment is under control of BlockHead, data is sent into the com-

Waveform	Analysis Channels	Data Combination
0	Signal	$\frac{1}{8}(A+B+C+D+E+F+G+H)$
S_E	EShift	$\frac{1}{8}((A+B+C+D)-(E+F+G+H))$
S_B	BShift	$\frac{1}{8}((A+B)-(C+D)+(E+F)-(G+H))$
$S_{\Delta B}$	Cal	$\frac{1}{8}((A-B)+(D-C)+(E-F)+(H-G))$
$S_E \otimes S_B$	EDM	$\frac{1}{8}((E-A)+(F-B)+(C-G)+(D-H))$
$S_E \otimes S_{\Delta B}$	ECal	$\frac{1}{8}((A-B)-(E-F)+(D-C)-(H-G))$
$S_B \otimes S_{\Delta B}$	BCal	$\frac{1}{8}((D-C)-(A-B)+(H-G)-(E-F))$

Table 5.4: Analysis channel definitions.

Analysis Channel	Comment
Signal	Total signal, it typically drifts over periods of 10 Blocks which is almost certainly due to changing target conditions.
EShift	Signal difference between E-states averaged over B-states, can indicate problems with electric field system.
BShift	Signal difference between B-states averaged over E-states, indicates the residual magnetic field in the laboratory.
Cal	Interference fringe gradient, good indicator of sensitivity. This channel should be maximised.
EDM	Measures the EDM. It can also be non-zero because of systematic problems.
ECal	Slope difference between E-states, can indicate leakage currents across the electric field plates.
BCal	Slope difference between B-states, can indicate interference lineshape asymmetry.

Table 5.5: Analysis channel physical significance.

puter via the analog inputs. At the end of each Block the YbF pulse data is saved, along with the magnetometer data and some preliminary analysis is performed on the YbF data to extract the analysis channel results for that Block. The first task of this preliminary analysis is to split that data into 8 sub-Blocks corresponding to the 8 primary states of the interferometer. These primary states correspond to the states of the magnetic and electric fields. Most of the data within each sub-Block is assumed to belong to a Gaussian distribution. However, some of the data points do not belong to this distribution because they have been disturbed by random events such as dust falling through the probe beam or spikes of electrical noise. These rogue points have a large effect on the mean and standard deviation of the data, and it is necessary to remove them in order to analyse the data using Gaussian statistics. Therefore, outlier data points in each sub-Block which lie 3.5 or more standard deviations from the mean of that sub-Block are removed. This results in loosing on average around a tenth of a data point per sub-Block. After the data has been "cleaned", the mean for each sub-Block is recalculated. At this stage we calculate the mean of each of the analysis channels by combining the sub-Block means, using the analysis channel definitions in Table (5.4).

At the end of each Block the preliminary data analysis for each channel is displayed on the computer screen. This provided a quick way of checking that

nothing catastrophic has happened to produce unexpected results in the analysis channels[2]. Our first check is to see that we have set up the magnetic field supply currents correctly to cancel out any residual magnetic field in the laboratory. The four magnetic fields used in the experiment are,

$$B_1 = -BCentre - \frac{\Delta B}{2} + Bbias$$
$$B_2 = -BCentre + \frac{\Delta B}{2} + Bbias$$
$$B_3 = +BCentre - \frac{\Delta B}{2} + Bbias$$
$$B_4 = +BCentre + \frac{\Delta B}{2} + Bbias$$

where Bbias compensates the residual field in the laboratory, and BCentre the field used to get to the centre of the interference fringe either side of the central maxima, see Figure (5.10). We add and subtract to this field $\Delta B/2$ which is the modulation field. Hence, the residual magnetic field can be calculated using the BShift and the Cal channel results, to be

$$B_r = \frac{BShift}{Cal}\frac{\Delta B}{2}. \tag{5.7}$$

To cancel out the BShift we adjust the bias current from the supply. For example if the BShift is 20% of Cal we adjust the bias current by 20% of the Cal step, the magnetic field amplitude step. With this method we can reduce the BShift to zero at the start of the data run. During the data run the residual field can drift, however we adjust the currents to compensate. This could be performed automatically by using the computer to control the current supply and lock the BShift to zero, however controlling the magnetic field in this way could easily lead to a systematic, if the electric field state influenced the locks output.

The most important result from the preliminary data analysis is to extract the EDM of the electron, which is given by the ratio of EDM to Cal:

$$\frac{EDM}{Cal} = \frac{-2d_e E_{eff}}{\mu_B \Delta B}. \tag{5.8}$$

The EDM of the electron is therefore,

$$d_e = -\frac{\mu_B \Delta B}{2E_{eff}}\frac{EDM}{Cal}. \tag{5.9}$$

There are some effects that will produce systematic EDMs therefore to get a correct answer we must perform further analysis and understand the systematic effects produced in the experiment. This will be the focus of the next chapter, along with the results of the experiment.

[2]These events can normally be attributed to human error.

Now all we have left to do is calculate the errors for the channels. For this we must make use of the covariance matrix[3] [3]. To find the covariance matrix for the analysis channels we first calculate the covariance matrix for the sub-Block data. Then we use the definitions of the each analysis channel to create a transformation matrix that transforms the sub-Block covariance matrix into the analysis channel covariance matrix. This transformation matrix is the same matrix which is used to calculate the means of the analysis channels. Using the analysis channel covariance matrix we calculate all of the analysis channel errors, and then find the weighted mean and standard error for each analysis channel. This concludes the first stage of data analysis and the results are saved into a database along with other parameters such as an estimate of the level of non-statistical noise, the experiment's state, the time of day and so on.

[3]Strictly the covariance matrix is an approximation because it should only be applied to data taken simultaneously, however, we can use it here because the data does not depend critically on the order it is taken it.

Chapter 6

Results and Systematics

In this chapter I describe the EDM results obtained using Raman transitions with the new supersonic source. I also describe the systematic effects that have been identified so far for this experiment.

6.1 Results

In this section I show some typical data and illustrate how problems can be identified using the data analysis.

In addition to the YbF pulses and data analysis results we also save magnetometer data, and metadata concerning the configuration of the experiment in the Block to be saved, listed in Table (6.1). This metadata is stored so that we can reconstruct, after the fact, possible correlations with the time of day or any other systematic aspect of the machine state. It is stored once in each Block as a zipped XML file along with the string of YbF pulses and magnetometer data.

On a typical day of running the experiment we expect to take around 150 to 200 Blocks. These are normally grouped in some 10 to 15 Clusters. In Figure (6.1) I have plotted the analysis channel results for the Cluster 18May0534. As the name suggests this data was taken on the 18^{th} of May 2005 and this was the 34^{th} Cluster of the day[1]. Before the start of this Cluster the target wheel was turned onto a fresh spot of Yb. The Signal analysis channel shows the typical behaviour for a new target spot, first it drops off, and then undergoes a small revival. This behaviour is mirrored in the Cal channel because as the Signal increases so too does the interference signal which results in a "bigger", more negative, Cal.

[1]The reason for the higher than usual number of Clusters was because the first Cluster of that day was started at 00:20 and this Cluster was started 22 hours later.

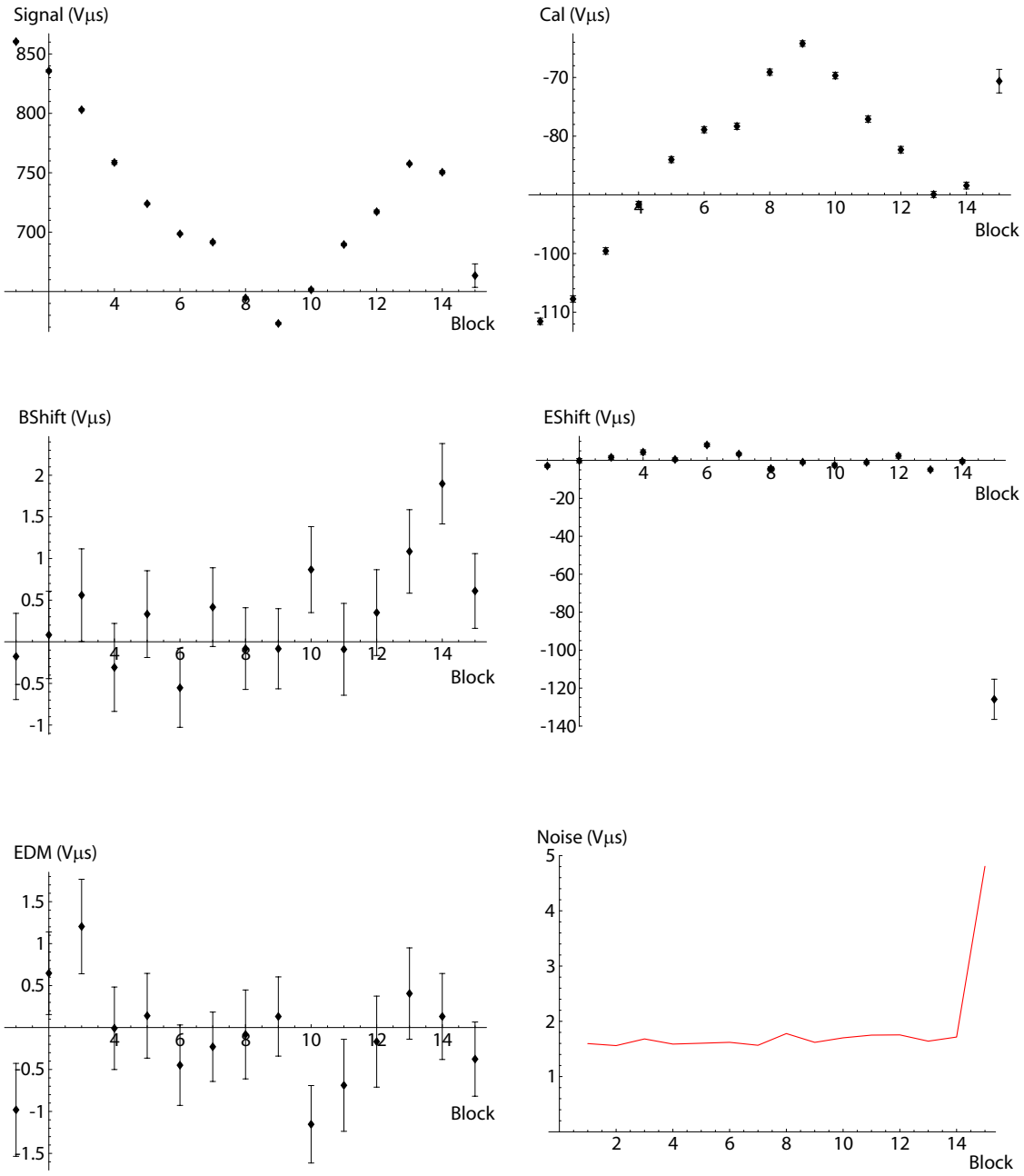

Figure 6.1: Some typical analysis channel results for a Cluster. Note that the laser unlocked during the last Block. On the x-axis is the Block number, and on the y-axis is the analysis result in $V\mu s$ except the Noise channel which indicates the estimated the noise in the EDM channel over statistical noise.

Block metadata
Date and time
Gate start time for each time of flight profile
Clock period between points of the time of flight profile
Electric field connections
Voltages to field plates (kV)
Magnetic field connections
Magnetic field amplitude step (μA)
Magnetic field reversal current (μA)
Magnetic field bias current (μA)
Current to magnetic field calibration
Cluster name
Switching waveform length
Switching waveform codes
Dead time before and after each switch

Table 6.1: EDM metadata. The magnetic and electric field connections parameters are explained later in this chapter.

If one looks more closely at the analysed data one sees that something odd happened to the Signal, Cal, EShift, and Noise Channels on the last Block. This indicates that something in the experiment changed during this Block. Indeed if one looks at the laboratory data book it says that the probe/pump laser unlocked from the Q(0) line during this Block. If the experiment had not been stopped after this Block all the analysis channels would have gone to zero. This can also happen when the YAG laser stops firing, which it does intermittently. The origin of this fault remains a mystery as the computer is seen to provide a "clean" pulse sequence to the YAG laser trigger. When such problems occur we exclude the "bad" Blocks from the final analysis of the data-set. The state of the experiment for this Cluster is shown in Table (6.2). In this table we see that the Cluster started at 10:18 at night on the 18^{th} of May 2005. The voltage supplies connected to the centre and guard field plates were set at ± 8 kV and ± 1.6 kV respectively. The current needed to cancel the laboratory residual magnetic field was $I_{bias} = +47$ μA. Next in the table are the Upper and Lower Raman frequencies, and the synthesizer output power to the Raman AOM. The PMT voltage is also recorded in order to know the correct calibration between photon counts and PMT amplifier voltage. The YAG parameters are also recorded. Finally the electric and magnetic field connections

Parameter	Value
Time and Date	22:18 pm, 18 May 2005
Voltage on C region plates	± 8 kV
Voltage on G region plates	± 1.6 kV
Magnetic field bias current	$+47$ μ A
Upper Raman centre frequency	85.315 MHz
Lower Raman centre frequency	85.31 MHz
Raman AOM drive Power	-4 dBm
PMT Voltage	1175 V
Flash to Q-switch delay	330 μs
Valve to Q-switch delay	405 μs
Electric field connections	True
Magnetic field connections	True

Table 6.2: Machine state for Cluster 18May0534.

are listed. These indicated how the connections from there supplies are arranged. These connections are periodically swapped to help us identify systematic problems. The significance of these connections will be explained later in this Chapter.

Using equation (5.9) from Section (5.3) we can convert the EDM analysis channel into an electron EDM result, this is called the "Raw EDM". Figure (6.2) shows the Raw EDM results for the Blocks in the Cluster above. The y-axis shows the Raw EDM in the conventional units of the EDM of e.cm. From this small Cluster of data one finds the weighted mean and error of $(6.17 \pm 8.8) \times 10^{-27}$ e.cm. This Cluster was 15 Blocks long, therefore, the data took approximately 32 minutes to collect. One can also estimate the sensitivity if we were to continue recording data with this sensitivity over a 24 hours period. The sensitivity from this Cluster is equivalent to 1.32×10^{-27} e.cm per root 24 hours of integration time which is about average for the experiment in its current configuration. This is a factor of about 1.4 less sensitive than the statistical sensitivity estimated in Chapter (5). However, it is over an order of magnitude better than the old YbF experiment with the oven source [29, 30]. This is due mainly to the new supersonic source producing cold YbF molecules in short pulses.

In order to take sensitive Clusters it is important to keep the noise as low as possible. Normally if one takes data on a fresh target spot of Yb, the noise level exceeds statistical noise by a factor of 1.2 to 2. However, after 15 to 20 Blocks the noise usually starts to increase probably because the target conditions are changing.

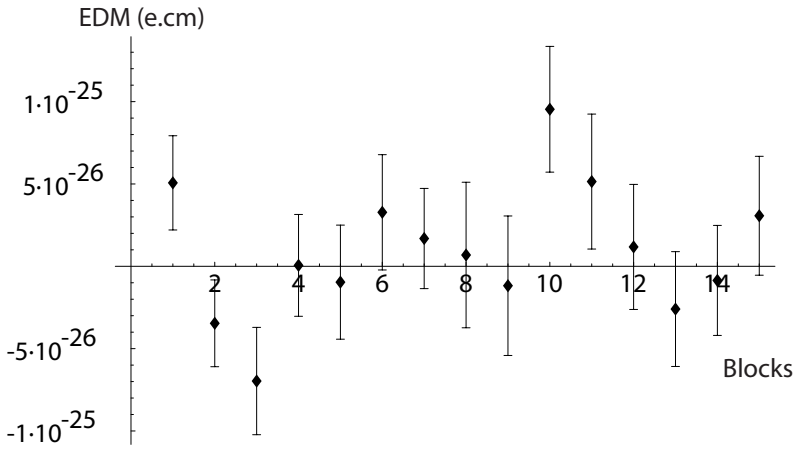

Figure 6.2: This shows the Raw EDM for the Cluster 18May0534. The y-axis shows the value of the EDM in e.cm, and the x-axis is the Block number.

Once the noise starts to increase we normally stop and restart the experiment on a new target spot. With this method we keep the noise level down and the sensitivity high over prolonged periods. Figure (6.3) shows an example of the typical behaviour for the noise in the EDM channel compared with statistical noise. The same Figure also illustrates the effect of the magnetic field drifting in the laboratory. These effects are independent of each other. This data was taken from Cluster 20May0515, under similar conditions to the previous Cluster example.

6.2 Systematic Effects

6.2.1 Internal versus External Effects

If a systematic effect is present in the data-set it is advantageous, when it comes to tracking down the effect's origin, that we can identify where the systematic is produced. To do this we manually swap the output connections of the high voltage supplies to the electric field plates, as indicated by the "True" or "False" in Table (6.2). Figure (6.4) shows a diagram of the electric field supply to the centre plates. The connections are manually reversed after the voltmeters which measure leakage current, discussed in Section (6.2.4). We can also swap the output connections from the magnetic field current supply. These manual changing of the connections are called "manual reversals". To decipher whether a certain systematic EDM is produced internally to the interferometer we look to see whether the systematic effect is correlated with the manual reversals. If it is then the effect is produced internally.

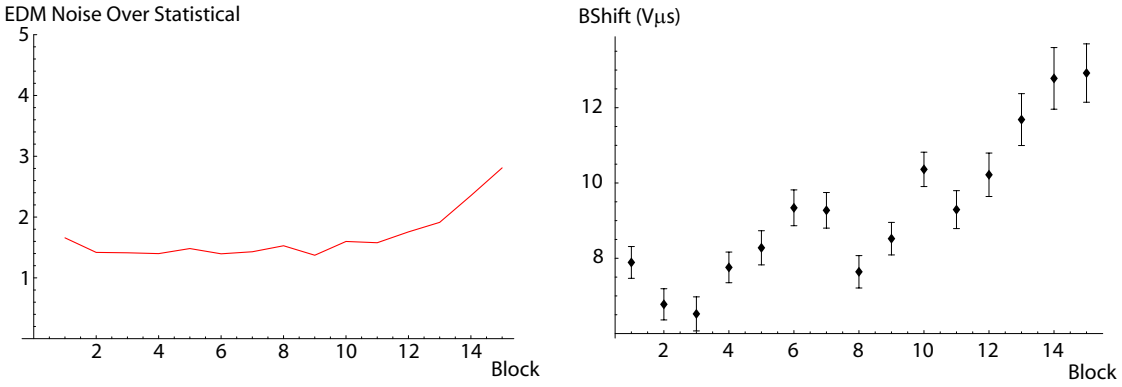

Figure 6.3: This shows the characteristic drift of the Noise channel, and also the BShift channel. The x-axis on both plots shows the Block number and the y-axis of the BShift plot is in unit of $V\mu s$.

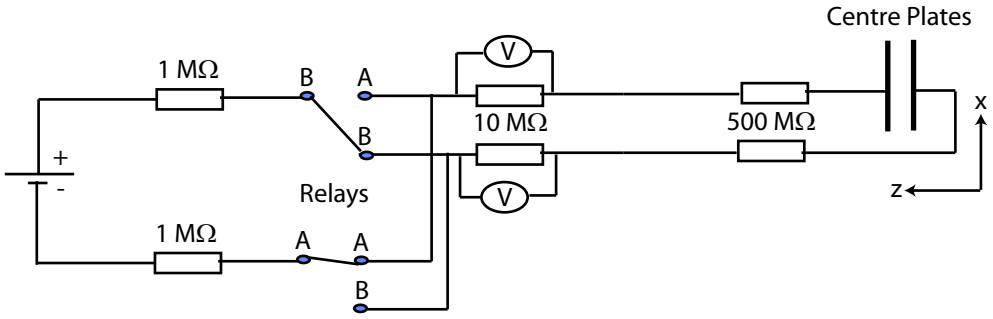

Figure 6.4: This shows the electrical connections for the centre plates.

For example, if leakage currents flow across the field plates, they would produce a systematic EDM. The sign of this false EDM would change when the electric field connections are reversed. This type of effect is called an internal systematic. On the other hand, if the effect were external then it would not be correlated to the manual reversal. For example, if the electric field relays were producing a magnetic field which was dependent on the relays state, then the false EDM produced would not change sign after the manual reversal because the effect depends on the magnetic field and not the polarity of the electric field in the interferometer. This type of effect is called an external systematic.

The signal from a real EDM of the electron changes when either one of the manual connections is changed. Systematic EDMs that change in this way can not be distinguished from real EDMs by simple using manual reversals of the fields. Systematics of this kind must produce a signal which is indistinguishable from a

magnetic field correlated to the electric field, which is internal to the experiment.

The electric field connections are swapped after the relays and the voltmeters, this means that the electric field plates are connected to the opposite relay and supply after the switch. For the magnetic field we simply swap the connections from the current supply to the z-coils which produces the same magnetic field magnitudes as before the swap except in the opposite direction. The convention for the magnetic field connections is that in the "True" state a positive current flowing out of the supply produces a positive magnetic field along the z-axis of the machine. The convention for the electric field connections state, is in state "True" and the relays in state B$\longrightarrow$B and A$\longrightarrow$A, the electric field points in the positive z-direction. The relay connections can be seen in the Figure (6.4).

6.2.2 Systematic Amplitude Effects

A systematic error can be produced when the interferometer's lineshape intensity is correlated with the electric field state and there is a residual magnetic field in the laboratory [29, 30].

It is easy to understand how the interferometer lineshape intensity could depend on the electric field state. For example, if there was a slight discrepancy in the amplitude of the electric field between its two states then the Raman/rf transition efficiency would be affected. Lets imagine they are slightly detuned from resonance in one of the states, but not in the other state. Then the interferometer signal would be more intense in one state of the electric field than the other. This effect would show up in the ECal analysis channel and produce a non-zero result. In Figure (6.5) a non-zero ECal signal is illustrated using the interference curve in the two electric field states. Ignoring the ΔB magnetic field steps for brevity, I have marked the data acquisition points on the curves. The graph on the left shows the ECal effect on its own, and the graph on the right shows the same effect with the addition of a residual magnetic field.

If we recall the definition of the EDM analysis channel, ignoring the ΔB step, we find the $\mathbf{EDM} = \frac{1}{4}(C - A + B - D)$. From the Figure we can see that there will be a false EDM generated when there is a non-zero ECal and residual magnetic field. However, this does not cause a major problem with our measurement because we are able to correct the EDM channel for the effect from the data itself. The false EDM is [29],

$$EDM_f = \frac{ECal}{Cal} BShift \tag{6.1}$$

where all parameters are known from the data analysis. Therefore, we can calculate

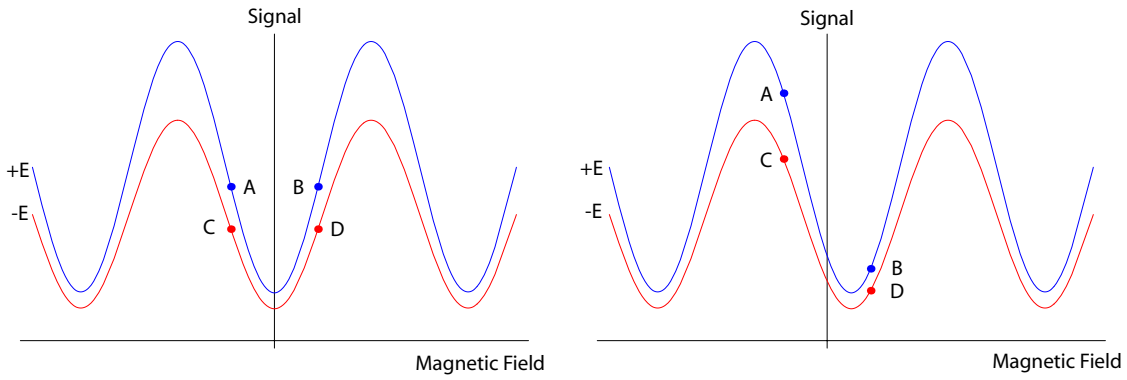

Figure 6.5: Left: The interference lineshape with a non-zero ECal. Right: The interference lineshape with a non-zero ECal and BShift.

EDM_f for each Block in a Cluster and subtract it from the EDM analysis channel. Fortunately, the extra noise from the ECal and Cal channels only leads to a small inflation of the EDM errorbar. When we take data we control the BShift by adjusting the currents to the z-coils. Normally we keep the BShift below 10% of Cal to minimise any correction that might be applied to the data later.

There is a second systematic of this type which we also correct for. This is the effect of the interference lineshape slope changing both with the electric field switch, ECal, and when the magnetic field is switched, BCal. The effect becomes clear when you look at Figure (6.6). The red and blue curves indicate the different electric field directions. The difference between the two peaks either side of the central minima are characteristic of the BCal effect. We calculate the full false EDM to be,

$$EDM_f = \frac{ECal}{Cal} BShift + \gamma \left(\frac{ECal \times BCal}{Cal} - EBCal \right). \tag{6.2}$$

Where EBCal comes from the analysis of $S_E \otimes S_B \otimes S_{\Delta B}$, and the constant γ tells us how far the applied BCentre field is from the centre of the central interference fringe.

The effect of these systematic corrections to the RawEDM results of the Cluster 18May0534 is small. The RawEDM result was $(6.17 \pm 8.8) \times 10^{-27}$ e.cm, and the corrected EDM, taking into account the electric field state, for this Cluster was $SignedCorrEDM = (1.23 \pm 8.92) \times 10^{-27}$ e.cm. As we can see the central value has changed by less than one standard deviation and the error bar is barely affected. A table of the other analysis channel results for this Cluster is shown in Table (6.3).

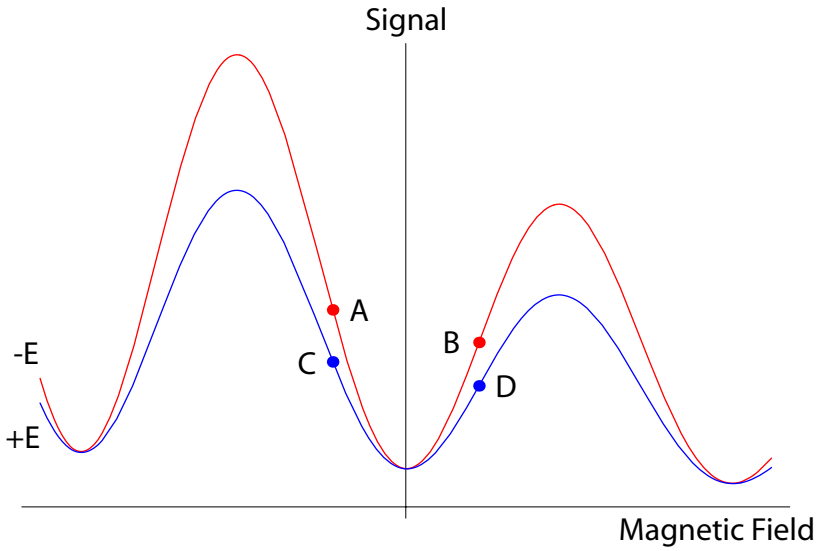

Figure 6.6: This shows the effect on the interference lineshape of non-zero ECal and BCal. This causes a systematic EDM result which we correct. The red and blue curves indicate the two electric field directions.

Channel	Mean and Uncertainty
Signal	$736.29 \pm 0.26\ V\mu s$
BShift	$0.34 \pm 0.13\ V\mu s$
EShift	$-0.15 \pm 0.24\ V\mu s$
Cal	$-84.46 \pm 0.14\ V\mu s$
ECal	$-0.22 \pm 0.14\ V\mu s$
BCal	$-0.01 \pm 0.16\ V\mu s$
EBCal	$0.51 \pm 0.16\ V\mu s$
RawEDM	$(6.17 \pm 8.80) \times 10^{-27}\ e.cm$
SignedCorrEDM	$(1.23 \pm 8.92) \times 10^{-27}\ e.cm$

Table 6.3: Corrected EDM for cluster 18May0534.

6.2.3 Systematic Magnetic Effects

In the best atomic experiment, [56], the atomic species was TI which has a maximum effective electric field of $E_{int} = 70\ MV.cm^{-1}$. In YbF this effective field is much larger with a maximum of $E_{int} = 25 \times 10^3\ MV.cm^{-1}$. Ignoring these enhancement factors both experiments would be equally sensitive to the Zeeman interaction because the magnetic moments in the states used are the same for both experiments. Therefore, taking the ratio of the two enhancement factors we find that the YbF experiment should be over two orders of magnitude less sensitive to magnetic field systematics than the TI experiment.

One of the main types of magnetic field systematics that cause many technical complications to some EDM experiments, is due to the motional magnetic field interaction with the molecules. This is caused by the molecules moving through an electric field. The magnetic field is given by the expression $B = v \times E/c^2$. The field produced is oriented perpendicular to the electric field direction. A systematic effect occurs when the applied magnetic field is not perfectly aligned to the electric field direction. This means that the applied magnetic field has a component along the direction of the motional field and the resultant field changes its magnitude when the electric field is reversed. As we will find out below, in this experiment the size of the systematic is highly attenuated due to a suppression of the molecules' interaction with the perpendicular magnetic field. An estimate of the size of this systematic effect with an exaggerated mis-alignment of the applied magnetic field puts it at the level of below 8×10^{-33} e.cm [29, 30]. This is well below the sensitivity of the experiment. For comparison the effect in the TI experiment was approximately 3×10^{-28} e.cm.

Apart from the enhancement factor, a second important advantage of YbF is its low sensitivity to magnetic field perpendicular to the applied electric field direction. To see how this comes about we need only consider the F=1 levels, $|\ 1,+1\rangle$,$|\ 1,0\rangle$,$|\ 1,-1\rangle$, of YbF interacting with magnetic and electric fields: $H = H_0 + \mu_B\left(B_z\sigma_z + B_x\sigma_x\right)$. Here the electric field interaction is contained within H_0 which also contains the rest of the molecular Hamiltonian. The magnetic field has been spilt into a part B_z along the electric field and a transverse part B_x. When $B_x = 0$, the eigenvalues are $E_{|1,\pm1\rangle} = \Delta \pm \mu_B B_z$ and $E_{|0\rangle} = 0$. That is to say, the $|\ 1,0\rangle$ state is energetically separated from the $|\ 1,\pm1\rangle$ states. For the field used in the EDM experiment this tensor Stark splitting, typically 6 MHz, is very much larger than the Zeeman splitting due to B_z, typically 40 Hz. The effect of some stray field B_x is to mix the $|\ 1,\pm1\rangle$ states with the $|\ 1,0\rangle$ state, but with the large

energy separation Δ, this leads to a much suppressed false EDM. As derived in [29] the suppression factor is,

$$S_r = -\frac{2\mu_B^2 B_x B_z}{\Delta^2}. \tag{6.3}$$

With the fields used in the experiment the transverse magnetic field systematic error is suppressed by many orders of magnitude, $S_r \sim 10^{-9}$. Consequently the EDM experiment is far less sensitive to transverse magnetic fields than atomic experiments.

Although the YbF experiment is comfortably insensitive to stray transverse magnetic fields, there is still a great concern from systematic effects due to magnetic field along the z-axis. This is because if one of these fields is correlated with the electric field switch it could cause a false EDM which would be indistinguishable from a real EDM. Also a problem would be caused if the magnetic noise, along the z-axis, is accidently correlated with the electric field switch. With this in mind we have installed a flux gate magnetometer between the magnetic shields to provide warning of any unwanted magnetic effects. The magnetometer is placed near the detection region and 25 measurements of the magnetic field along the z-axis are taken at the beginning of each YbF pulse. This data is saved along with the normal YbF data in every Block.

The Fourier spectrum of the magnetic field was presented in the last chapter. We saw that the dominate noise source was the field produced by the mains electricity in the laboratory. The noise from this source is so large that it affects the experiments sensitivity. This is because each shot of YbF molecules interact with a different magnetic field because they asynchronously sample the 50 Hz background field. The effect of this background field would average away if we took an very large number of measurements. However, the number of Points within a Block is not large enough to do this and therefore, every Block of EDM data is limited by the mains field. In order to eliminate this excess noise, we phase-lock the experiment to the mains frequency. At the start of each Block the experiment is synchronized to the mains frequency and each YbF pulse is triggered with the same phase, with respect that signal, as the last YbF pulse. In this way, all of the YbF pulses, within a Block, interact with the same main magnetic field, reducing that Block's error bar.

Figure (6.7) shows a sample of the magnetic field data acquired with the experiment phased-locked to the mains frequency. The top plot shows the 10 ms of magnetometer reading taken over each of the first three YbF pulses in a Block. They have been overlapped to show the 50 Hz background magnetic field. The

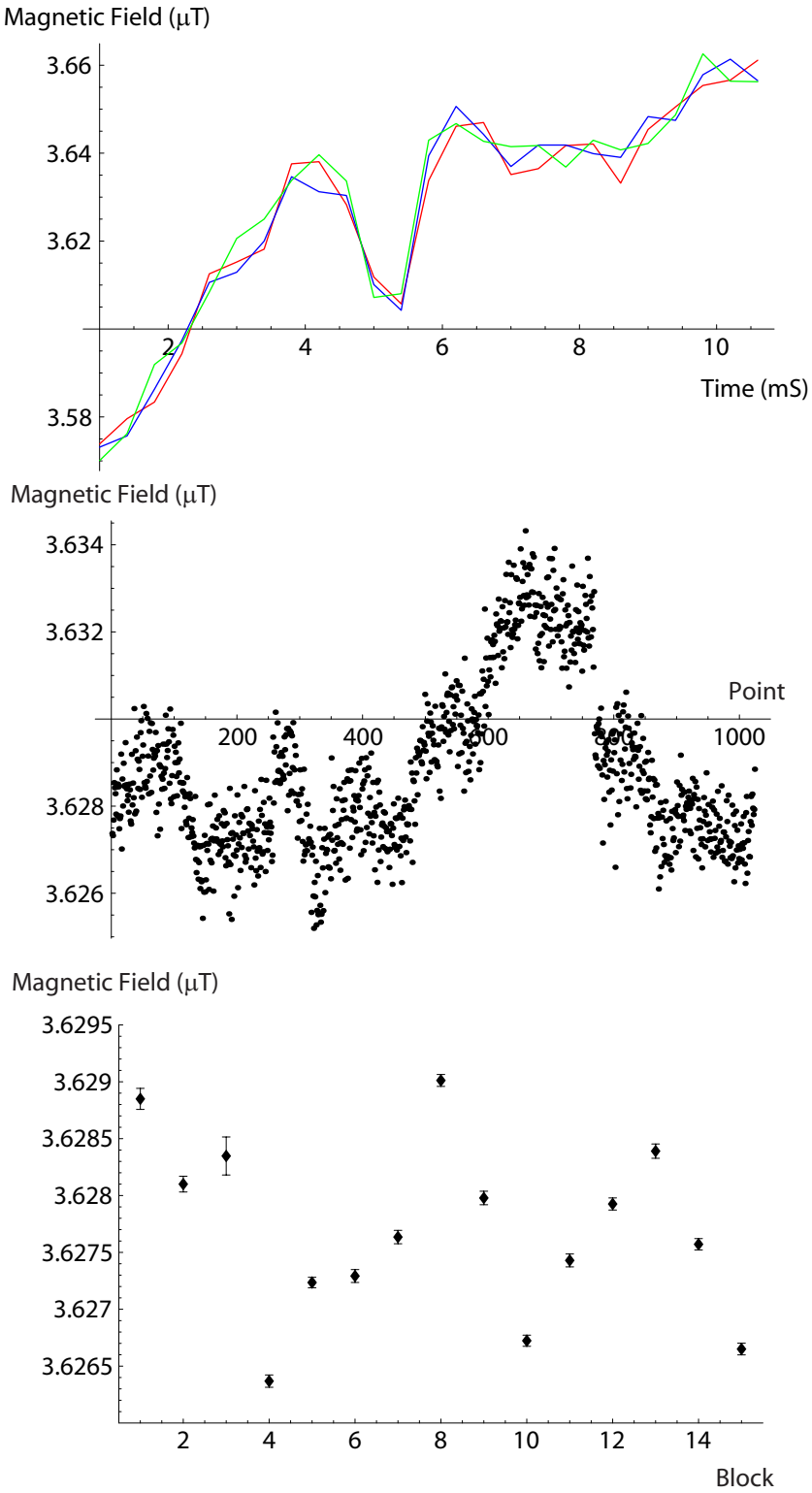

Figure 6.7: The data in the three graphs is from the Cluster 18May0534. Top: Three overlapped Magnetometer TOFs from the first Block of the Cluster. Middle: Magnetic field in the z-direction for the first Block. Bottom: Magnetic field in the z-direction for the Cluster.

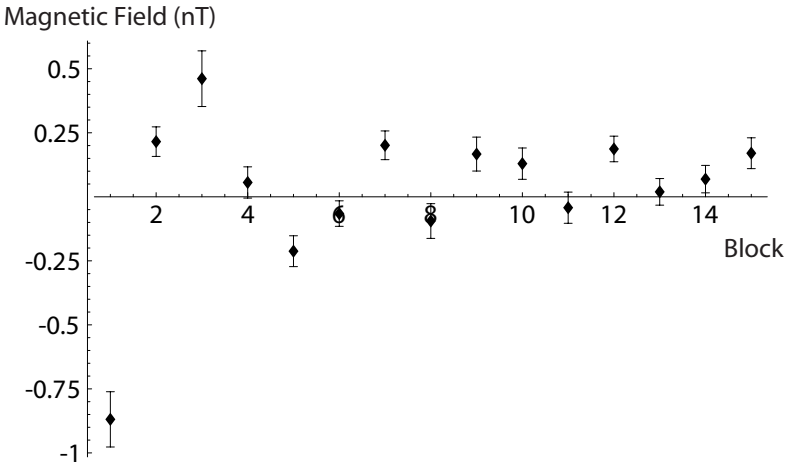

Figure 6.8: The magnetic field correlated with the electric field reversal measured in nT.

magnetometer is triggered 1000 μs after the Valve is pulsed, at the same time that the PMT is triggered to detect the YbF pulses. A magnetometer data point is then recorded every 400 μs for 10 ms, recording in total 25 data points per YbF pulse. These data points are then averaged together. Once the Block has finished all the magnetometer data is saved. The averaged magnetometer signal for each YbF pulse, of the sample Block, are shown in the middle plot of the figure. We can see from this middle plot that the magnetic field varies significantly during a signal Block of data, which lasts approximately 125 seconds. Each of the 1024 points on this plot, one for every YbF pulse in the Block, is the average of the 25 magnetometer data points. At the end of each Block the magnetometer data is analysed in exactly the same way that the YbF data is analysed. Therefore, at the end of each Block we have the magnetometer data results for the weighted means and standard errors of all the analysis channels. In the bottom graph of Figure (6.7) I have shown the magnetometer Signal channel for a whole Cluster. This Cluster is the same one that was used to show the YbF data earlier. Each data point has a mean and standard error from the Signal channel for each Block in the Cluster. As we can see there is a large variation of the magnetic field.

The magnetic field of interest is the field that is correlated to the switching of the electric field. This comes out in the EShift analysis channel applied to the magnetometer data, plotted in Figure (6.8) for the Cluster 18May0534. The weighted mean for the data in this Cluster tells us that the problematic magnetic field outside the inner shield was (42.5 ± 55.8) fT. To judge whether or not this size of magnetic field is a problem we need to know the shielding factor of the inner shield, and have a reasonable margin of error. This error margin allows for the

fact that the magnetometer reads the magnetic field at a point, but the molecules interact with the field along the length between the rf/Raman transitions. Also the magnetometer may not be perfectly aligned with z-axis defined by the electric field, this means that the field in non-troublesome directions is mixed into the magnetometers reading.

To measure the shielding of the inner magnetic shield we constructed a large rectangular coil of wire around the experiment, which produced a magnetic field along the z-axis. Looking down from the top of the experiment the coil was placed 25 cm outside the outer shield. The coil was 2.4 m tall along the beam direction, and 1.9 m wide parallel to the field plates. We ran a current of 3 A through the coil which produced a magnetic field of 270 nT along the z-axis, as recorded by the magnetometer. We then scanned an interference signal with the molecules and measured an offset of the central minimum of -34 μA from zero, compared to -169 μA before the current was applied to the coil. Hence, the molecules were measuring a change in the field of 2.23 nT. Taking the ratio of the magnetometer data and the molecular data tells us that with this geometry of externally applied field, the shielding factor from the inner shield was $S = 121$. We then changed the coil shape by reducing its height to 1 m. With this geometry we measured a shielding factor of $S = 50$. This indicated that the inner magnetic shield is more efficient at shielding homogeneous fields than fields from "close" point sources.

If we equate the phase produced by the Zeeman effect to that produced by an EDM, we can related the EDM in terms of a magnetic field which switches with the electric field. Using an electric field of 10 kV/cm, the conversion is (4×10^{-30}) e.cm/fT. Taking the worst-case for the shielding factor of $S = 50$ and the above conversion, we find the systematic magnetic field measured by the magnetometer, from the example cluster above is equivalent to a false EDM, inside the inner shield, of $(4.2 \pm 1.2) \times 10^{-27}$ $e.cm$. This is compared to the EDM measured by the molecules, for the same Cluster, of $(1.23 \pm 8.9) \times 10^{-27}$ $e.cm$. The fact that these two numbers are so close is somewhat alarming at first sight.

Figure (6.9) shows the EShift magnetic field in e.cm for 1510 Blocks taken continuously over a four day period. These Blocks are the dual of the EDM Blocks taken at the same time. One major feature of this graph is the large variation of the signal in comparison with its mean value: (13.6 ± 15.3) fT. The second point is the much larger standard deviation of the data in the day time, between 0800 and 2000 hours, than at night. Figure (6.10) illustrate this further. Here the data has been binned according to the time in a 24 hour period and the number of standard deviations of each Block's mean from the data-set's mean is plotted.

The brightness of the light regions indicate the number of Block with a particular number of standard deviations from the mean of the data-set. If we took a cross section of the plot along the x-axis we would see a histogram showing how many Blocks had a mean value a certain number of standard deviations from the mean of the data-set, for a given time. We can see that in the period between midnight and 0500 the spread of the data is narrower that then data between 0500 and 2000. After this time the distribution get narrower again.

If we compare the EDM noise, for an hour of data, with the average magnetic noise over the same period, we can determine if the magnetic noise is limiting the sensitivity of our measurement of the EDM. We find that about 30% of the daytime Blocks are limited by the magnetic field variation. This can be tolerated for now, however it will become more of an issue as the sensitivity of the interferometer improves.

Calculating the weighted mean and standard deviation of all the EShift magnetometer data recorded in between the magnetic shields, from the 16^{th} to the 20^{th} of May 2005, we find the result,

$$B_e^M = (13.6 \pm 15.3)\ fT. \tag{6.4}$$

Using the worst-case inner magnetic shielding factor of 50, this converts to a false EDM of $d_e^M = (5.45 \pm 6.12) \times 10^{-29}$ e.cm. This results takes into account the directions of the electric and magnetic fields to get the correct signs for the EShifts of each Block in the average. Since the magnetometer does not sample exactly the same field as the molecules we hesitate to make a systematic correction on the basis of equation (6.4)), however it is small enough that we can comfortably ignore the effect for now. In the future we will need to build a better magnetometer, ideally one that samples exactly the same field as the molecules. See Chapter (7) for details.

6.2.4 Leakage Currents

The fluxgate magnetometer measurement deal with magnetic fields generated outside the shields, but we have still to consider fields emanating from within. The problematic fields correlated with the electric field switch are most likely to be leakage currents from the electric field system itself. They are most likely to flow at the high voltage vacuum feedthroughs to the plates or around or between the field the plates themselves. These small currents must be controlled to a high level because they can produce troublesome magnetic fields along the z-axis, that are correlated with the electric field switch. These produce false EDM signals which

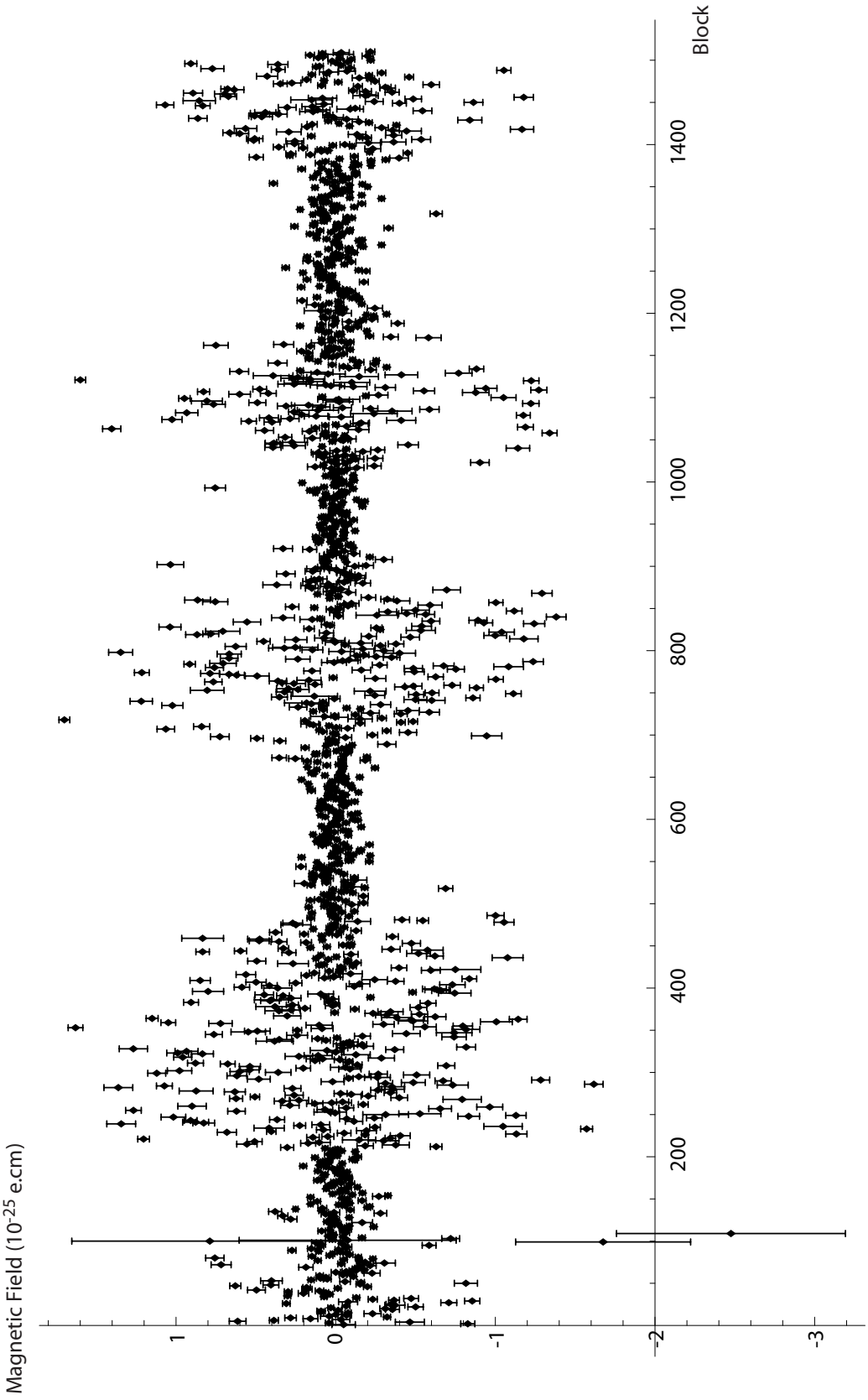

Figure 6.9: The magnetic field correlated with the electric field reversal measured in *e.cm*. For a data-set of 1510 Blocks recorded over several days continuously.

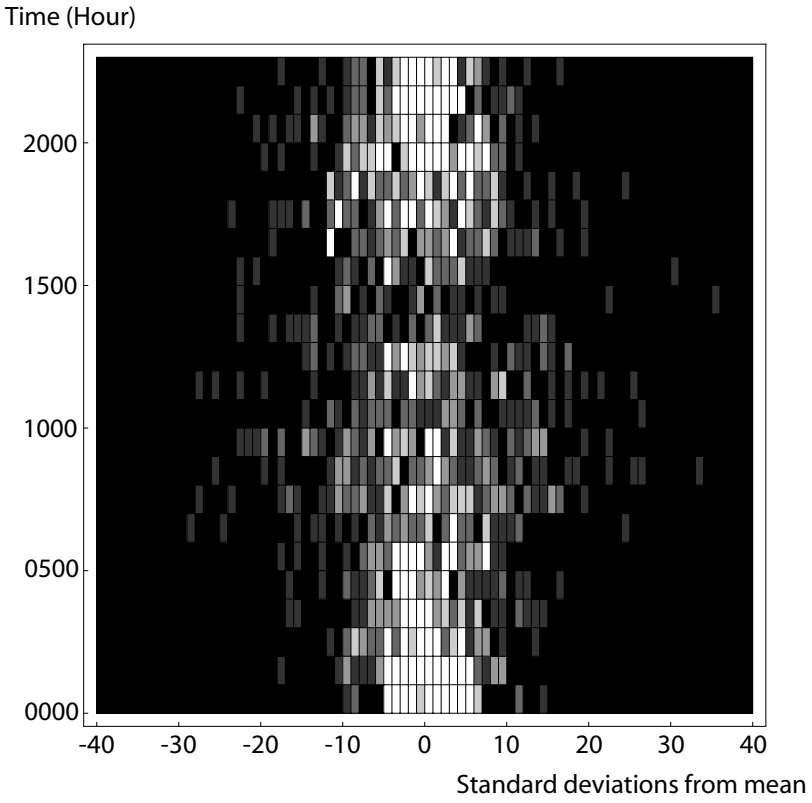

Figure 6.10: The magnetic field correlated with the electric field reversal measured binned according to the data was taken in a 24 hour period. The plot shows the number of Blocks, indicated in white, had a mean value, a certain number of standard deviation from the mean of the entire data-set, for a given time of day.

are distinguishable from the real EDM. In the worst-case, it is simple to show that a leakage current of 10nA flowing around the electric field plates, in the x-y plane, will produce a systematic EDM of $d_e < 4 \times 10^{-28}$ e.cm. Therefore, leakage currents are controlled to be below 1 nA in the experiment.

This is small enough not to affect the experiment, but we can only be sure it remains so by monitoring the current throughout the EDM measurement. For the data in this thesis I measured the leakage currents and manually recorded them periodically. Most recently we have built and implemented leakage current monitors that are read by the computer and recorded for each Block. Figure (6.11) shows the circuit diagram of the leakage current monitors. The main feature of the new monitors is that they are linked to the computer via fibre optic connections, and the current can be read at the 1 nA level. At the input the leakage current flows through the 10 MΩ resistor, and the voltage across this resistor is measured. This voltage is then converted into a square wave with a frequency proportional to the input voltage. The square wave is then converted into a sequence of light pulses send to the computer. The circuit is powered by two rechargeable batteries all contained within a plastic box. The triangles in the diagram indicate local grounds which float up to high voltage.

6.3 Data Analysis

In this section I show the results and further analysis of the whole data-set. The data was taken from the 26^{th} of April until the 24^{th} of June 2005. This data-set was taken using Raman transitions and not the pulsed rf technique.

To ensure the data-set has only valid data in it the Blocks which have some problem in them, such as the laser unlocking, have been excluded from the analysis. In Figure (6.12) a histogram of the EDM results from all the include Blocks, of which there are 3222, are shown with a Gaussian probability distribution. On the x-axis of the plot the EDM results have been normalised to their standard deviations. From the figure we see that the EDM data agrees well with the Gaussian distribution. However, we must recall that in the analysis we remove outlier points 3.5σ from the mean of the sub-Blocks. We did this because the EDM data suffers from occasional rogue points which do not belong to a Gaussian distribution. Apart from these random events, we also must recognise that the magnetic field in the laboratory is not well described by Gaussian statistics and this also has an effect on the EDM results. Although we did find out that this problematic magnetic field background does not lead to a large systematic EDM. In order to take into account the non-

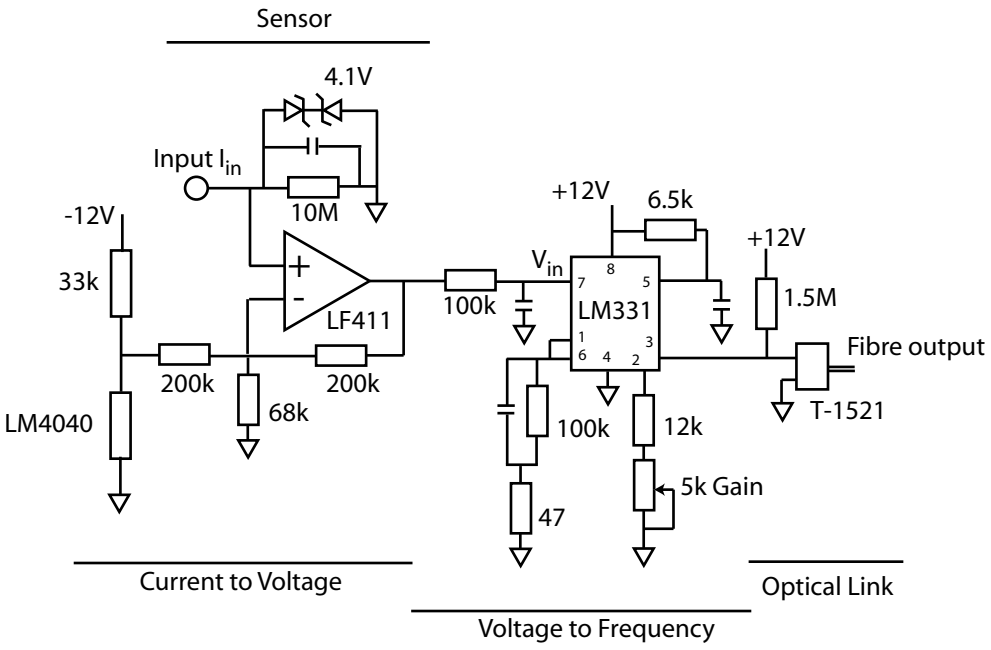

Figure 6.11: Leakage current monitor circuit diagram. The 10 $M\Omega$ is the sensor resistor. This circuit converts the input circuit into a voltage and then into a frequency for a square wave. This wave is transmitted via optical fibre to the control computer which records the leakage current.

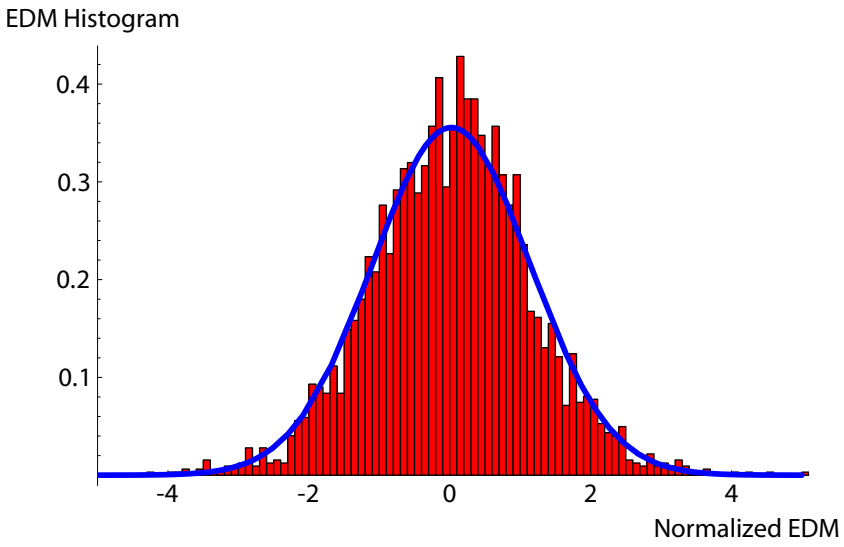

Figure 6.12: Histogram of the EDM results for the Blocks in the data-set. The x-axis shows the Blocks EDM normalized to its standard deviation. The solid line is a Gaussian probability distribution.

Gaussian distribution of EDM data without removing any outlying point we will need to use BootStrap Statistics.

Figure (6.13) shows all of the EDM results, from the included Blocks in the data-set. The colours indicate the four manual electric and magnetic field states of the apparatus. One notes that in Figure (6.13) the errorbars are larger after around 2250 Blocks. This is because we decreased the applied voltage to the C-region field plates to ± 2 kV from ± 8 kV. By reducing the electric field interacting with the molecules the sensitivity to the EDM is decreased, through the polarisation factor in equation (1.5), however, the sensitivity to many systematic effects is not decreased. This is a simple systematic check. The drawback of this method is that it takes more data to reach the same EDM sensitivity.

Table (6.4) shows the results for the whole data-set divided into the four different manual states of the experiment. The data labelled "signCorrEDM" are for the fully corrected EDM results. Taking their weighted mean, we find the value $(12.18 \pm 7.00) \times 10^{-28}$ e.cm. The errorbar in this result is marginally smaller than in [56], and our result has a 34% probability of being consistent with their result. The next channel of interest in the table is the EShift analysis channel. A large non-zero result in this channel would indicate a problem with the electric field system, like a faulty relay or loose connection. In this case we see that it is slightly non-zero in all of the machine states. This is because at the start of most Clusters the YbF signal

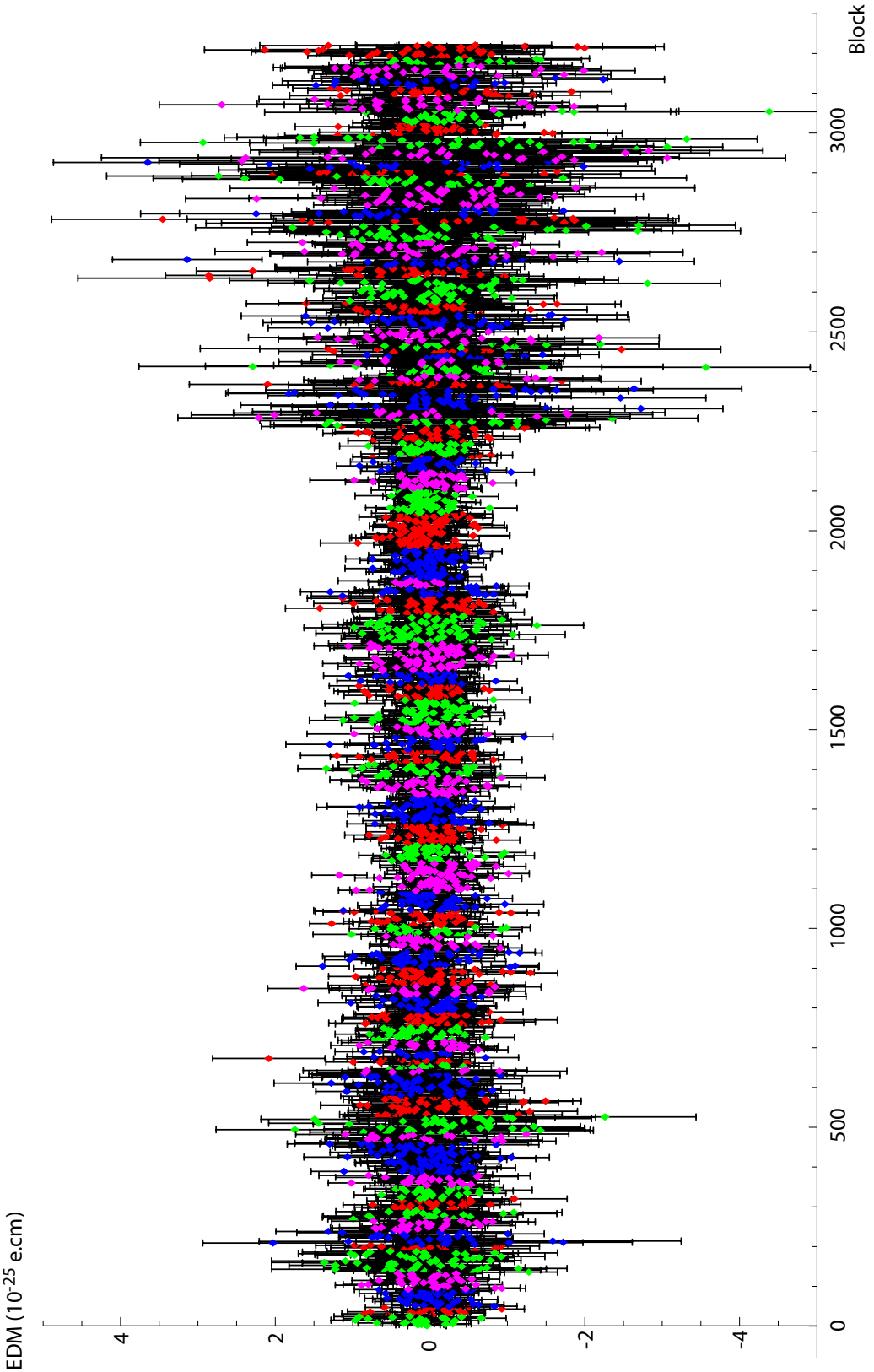

Figure 6.13: The measured EDM in *e.cm*. For a data-set of 3222 Blocks recorded over many days.

	Machine state (electric, magnetic field)			
	(False, False)	(False, True)	(True, False)	(True, True)
signCorrEDM e.cm	$(-5.23 \pm 14.75) \times 10^{-28}$	$(13.02 \pm 13.33) \times 10^{-28}$	$(9.53 \pm 14.27) \times 10^{-28}$	$(28.86 \pm 13.74) \times 10^{-28}$
Raw EDM e.cm	$(-6.43 \pm 14.56) \times 10^{-28}$	$(-11.86 \pm 13.17) \times 10^{-28}$	$(-8.07 \pm 14.11) \times 10^{-28}$	$(25.66 \pm 13.57) \times 10^{-28}$
Signal Vμs	875.9 ± 0.04	869.6 ± 0.04	825.6 ± 0.04	829.7 ± 0.04
EShift Vμs	0.12 ± 0.04	-0.06 ± 0.03	-0.88 ± 0.03	-0.62 ± 0.04
BShift Vμs	-0.82 ± 0.02	0.02 ± 0.02	-0.24 ± 0.02	0.39 ± 0.02
Cal Vμs	-88.85 ± 0.02	-87.14 ± 0.02	-80.36 ± 0.02	-87.37 ± 0.02
ECal Vμs	0.11 ± 0.02	0.09 ± 0.02	0.10 ± 0.02	0.04 ± 0.02
BCal Vμs	0.08 ± 0.03	0.003 ± 0.02	0.099 ± 0.02	-0.05 ± 0.02
EDM Vμs	0.011 ± 0.02	0.004 ± 0.02	-0.019 ± 0.02	0.0396 ± 0.02

Table 6.4: Data analysis channel results averaged over the data-set.

increases, as the target heats up. This means that in the first couple of Block in most Clusters there will be a non-zero EShift. The EShift then hovers about zero. The BShift channel is also slightly non-zero, this is because we magnetic field in the laboratory slowly drifts during the Clusters. However, we do cancel this field so that it is always below 10% of the Cal channel. The BShift, ECal, and BCal results are all small which means that the systematic correction will be also small. As indeed we can see from comparing the Signed Corrected EDM value with the Raw EDM value.

In order to elucidate what this EDM result means, we look at the high voltage EDM data and compare them with the low voltage data. The high field data was collected with the centre plates at ±8 kV and the guard plates at ±1.6 kV, with this configuration we measured $(17.84 \pm 7.268) \times 10^{-28}$ e.cm. For the result to be a correct measurement of electron EDM we would expect the result of the low voltage run to be consistent with the high voltage run. However, the low voltage run measured a value of $(-59.16 \pm 25.8) \times 10^{-28}$ e.cm, which has a larger errorbar than the high field data, but has only a 0.2% probability of being consistent with the high voltage run. This indicates that the result probably has a systematic error in it.

From the magnetometer data, and the leakage current monitoring we know that the systematic is not one of those explained above. Also in the Appendix (A) I calculated another systematic, however its size is also too small to explain the systematic in our data. Currently we do not have a model of the systematic effect which is consistent with the experimental data. However, we know that the size of the systematic is depended on the magnitude of the electric field. This is because the systematic EDM changed size when we changed the applied voltages to the centre field plate from ±8 kV to ±2 kV, and these results were highly unlikely to be consistent with each other. Another important clue to the effect's origin, is that the Raman transition occur very close to the edges of the field plates. Figures (3.5) and (4.5) show this. The reason for this is historical because the holes in the inner shield were not designed for the field plates that are now in use. This means that the Raman transitions are being driven very close to the fringe fields from the plates.

This would suggest that the effect depends upon the gradient of the electric field between the guard plates and the centre plates. In this region the electric field is not homogeneous because of the gap between the guard and centre plates. Also the field produced by the centre plates may not be as homogeneous as we calculate it to be. These gradient fields change depending on the voltages to the

plates. Currently we are continuing to examine the systematic effect using pulsed rf transitions instead of the Raman transitions. With this scheme we can gate the rf pulse to be so short that the molecules are nearly stationary over the time the rf is switched on. This means we can select the molecules in the homogeneous region of the electric field and therefore the measurement should be insensitive to systematic effects depending on electric field gradients. Preliminary data using this technique suggests that the systematic has been eliminated, although this data has not been fully analysed at this stage.

Chapter 7

Conclusion and Future Prospects

7.1 Conclusion

The work presented in this thesis has significantly increased the statistical sensitivity of the YbF measurement of the electron EDM by a factor of approximately 40, with a new uncertainty of $\sigma_{d_e} = 7.00 \times 10^{-28}$ e.cm. The statistical sensitivity of YbF measurement method has been demonstrated to be marginally better than any other previous EDM measurement. Although the current measurement is limited by a systematic effect this has been speculatively attributed to the Raman transitions being driven in the fringes of the electric field. Measurements are now underway which use pulsed rf, synchronised with the molecular beam so that the molecules are not in the fringe fields when the pulses are applied. This is giving promising results. On current evidence a measurement of the electron EDM in the range of 3×10^{-28} e.cm is possible in the very near future using YbF molecules. This will be the most sensitive measurement of the electron EDM ever made and will provide interesting results with respect to the proposed physics beyond the standard model.

7.2 Future Improvements

There are a number of possible ways that the current EDM experiment can be improved. In this section I will outline several possibilities.

One of the most important, indeed essential improvements to the experiment will be to improve the current magnetometery to provide magnetic field measurements from within the inner shields. There are several options for achieving this. In the short term an optical pumping magnetometer could be placed within the inner shields. They are non-magnetic and the light which they require can be delivered through fibre-optics into the vacuum chamber. Preferably several magnetometer

cells would be placed between the electric field plates as close to the YbF beam as possible without obstructing the beam. A prototype is being built.

A longer term options for magnetometery is to build a full co-magnetometer for the experiment. This would be in the style of the Tl EDM experiment [56] which used a Na beam for magnetometry. In that experiment, the $v \times E$ systematic error in the Na was cancelled by using two counter-propagating Na beams. We plan instead to used one CaF beam which is insensitive to the $v \times E$ systematic error for the same reason that YbF is. CaF seems a good choice of molecule because its structure is very similar to that of YbF [32]. Currently, we are testing the feasibility of that.

Another possible scheme for co-magnetometery would be to use a state in YbF which is not sensitive to the EDM of the electron. A possible candidate for this is the (N=1, m_N=0) rotational state which has a turning point in its Stark shift. At the turning point the gradient of the Stark shift with respect to the electric field is zero, and therefore the molecules are not polarized in the electric field direction, but the molecules are still sensitive to a magnetic field B_z.

At the time of writing this thesis an experiment has been started to produce a high intensity supersonic YbF beam that can be used in the experiment. The idea is to ablate Yb at a high frequency in the presences of a high pressure Helium buffer gas containing SF_6 to produce YbF. The hot YbF produced in this way can thermalise with the buffer gas and could make an effusive molecular beam of YbF, pre-cooled using the buffer gas. In this way a lot more cold molecules can be produced. The above technique is currently being investigated and developed. This technique has been successfully demonstrated using PbO molecules [46].

A slightly longer term improvement is to lengthen the EDM apparatus. The advantage gained here is an increase in sensitivity due to the electric field interaction time increasing. The limitation to this, of course, is a signal loss due to the divergence of the molecular beam. To overcome this problem an electrostatic guide might be built to guide the molecules through the experiment. The current technology of Stark decelerators [73] could be adapted for this purpose. This would mean that the divergence of the molecular beam could be altered to produce stable molecular trajectories through the lengthened experiment. However there could be some unwanted additional systematics produced by this method. One of the major ones could arise from the molecules accumulating a geometric phase from the internuclear axis undergoing loops following the electric field.

Another longer term idea is to use BaF molecules aswell. We would perform a similar experiment on BaF as we currently do with YbF, however in the detection

stage we would excite the molecules to a stable Rydberg state and use ionization detection. This is a very efficient detection technique and could significantly improve the sensitivity of the experiment, even though BaF has a smaller enhancement factor than YbF. Previously, stable Rydberg states were searched for in YbF, however this was unsuccessful. BaF would be produced in a similar way to YbF. We have produced a beam of BaF molecules using a thermal source, much the same of the old source of YbF, and a spectrum has been recorded. To implement a BaF EDM experiment would require a significant amount of development time. However, it could provide an increase in sensitivity when we the current YbF experiment reaches its limits.

One short term improvement is to use a 100 Hz YAG laser and operate the experiment at this frequency. This would mean we could integrate down to about $d_e = 3 \times 10^{-28}$ e.cm in ten days instead of one hundred. Therefore, with the above improvements it would be possible to measure the electron EDM below 10^{-28} e.cm. A further improvement could be made by decelerating and trapping the molecules. A prototype decelerator has been designed and build and YbF has been decelerated [73]. Currently a full scale experiment is being designed to decelerate YbF to rest and then to trap the molecules. Performing an EDM experiment with a trapped source of cold molecules seems to offer very large gains in sensitivity because the coherence time could be significantly increased by more than an three orders of magnitude. However, the systematic effects for EDM experiments using trapped molecules have not yet been fully worked out.

Bibliography

[1] A. Alavi-Harati *et-al*, Observation of *CP* violation in $K_L \to \pi^+\pi^-e^+e^-$ decays, Phys. Rev. Lett. **84**, 408 (2000)

[2] J. B. Anderson, and J. B. Fenn, Velocity distributions in molecular beams from nozzle sources, Phys. Fluids. **8**, 780 (1965)

[3] R. J. Barlow, Statistics: A guide to the use of statistical methods in the physical sciences, Wiley (2002)

[4] S. M. Barr, A review of *CP* violation in Atoms, Int. J. Mod. Phys. A. **8**, 209 (1993)

[5] H. L. Bethlem, and G. Meijer, Production and application of translationally cold molecules, Int. Rev. Phys. Chem. **22**, 73 (2003)

[6] M. Blackman, and J. L. Michiels, Efficiency of counting systems, Proc. Phys. Soc. **6**, 549 (1948)

[7] D. B. Chao, D. Chang, and W. Y. Keung, Electron electric dipole moment from *CP* violation in the charged Higgs sector, Phys. Rev. Lett. **79**, 1988 (1997)

[8] J. H. Christenson, J. W. Cronin, V. L. Fitch, and R. Turlay, Evidence for the 2π decay of the K_2^0 meson, Phys. Rev. Lett. **13**, 138 (1957)

[9] E. D. Commins, Electric dipole moments of leptons, Adv. At. Mol. Opt. Phys. **40** 1 (1999)

[10] P. C. Condylis, J. J Hudson, M. R. Tarbutt, B. E. Sauer, and E. A. Hinds, Stark Shift of the $A^2\Pi_{1/2}$ state in ^{174}YbF, J. Chem. Phys. **123**, 231101 (2005)

[11] J. W. Cronin, *CP* symmetry violation – the search for its origin, Rev. Mod. Phys. **53**, 373 (1981)

[12] D. DeMille, F. Bay, S. Bickman, D. Kawall, L. Hunter, D. Krause Jr., S. Maxwell, and K. Ulmer, Search for the electric dipole moment of the electron using metastable PbO, AIP Conf. Proc. 596 (2001), editors. D. Budker, P. H. Bucksbaum, and S. J. Freedman

[13] W. Demtröder, Laser spectroscopy: Basic concepts and instrumentation, Springer (1996)

[14] K. L. Dunfield, C. Linton, T. E. Clarke, J. McBride, A. G. Adam, and J. R. D. Peers, Laser spectroscopy of the lanthanide monofluorides: Analysis of the $A^2\Pi - X^2\Sigma^+$ transition of the ytterbium monofluoride, J. Mol. Spec. **174**, 433 (1995)

[15] A. R. Edmonds, Angular momentum in quantum mechanics, Princeton University Press (1996)

[16] J. Ellis, Theory of the neutron electric dipole moment, Nucl. Instrum. Methods. Phys. Res. Sect A. **284**, 33 (1998)

[17] G. Feinberg, Effects of an electric dipole moment of the electron on the hydrogen energy levels, Phys. Rev. **112**, 1637 (1958)

[18] V. L. Fitch, The discovery of charge-conjugation parity asymmetry, Rev. Mod. Phys. **53**, 367 (1981)

[19] V. L. Fitch, R. F. Roth, J. S. Russ, and W. Vernon, Evidence for constructive interference between coherently regenerate and *CP*-nonconserving amplitudes, Phys. Rev. Lett. **15**, 73 (1965)

[20] C. Foot, Atomic physics, Oxford Master Series in Atomic, Optical, and Laser Physics, Oxford University Press (2005)

[21] R. L. Garwin, L. M. Lederman, and M. Weinrich, Observation of the failure of conservation of parity and charge conjugation in meson decays: the magnetic moment of the free muon, Phys. Rev. **105**, 1415 (1957)

[22] M. B. Gavela, Le Yaouanc, L. Oliver, O. Pene, and J. C. Raynal, *CP* violation induced by penguin diagrams and the neutron electric dipole moment, Phys. Lett. B. **109**, 215 (1982)

[23] J. Goldemberg, and Y. Torizuka, Upper limit of the electric dipole moment of the electron, Phys. Rev. **129**, 2580 (1962)

[24] P. G. Harris, C. A. Baker, K. Green, P. Iaydjiev, S. Ivanov, D. J. R. May, J. M. Pendlebury, D. Shiers, K. F. Smith, and M. van der Grinten, New experimental limit on the electric dipole moment of the neutron, Phys. Rev. Lett. **82**, 904 (1999)

[25] G. E. Harrison, M. A. Player, and P. G. H. Sandars, A multichannel phase-sensitive detection method using orthogonal square waveforms, J. Phys. E. **4**, 750 (1971)

[26] B. J. Heidenreich, O. T. Elliott, N. D. Charney, K. A Virgien, A. W. Bridges, M. A. McKeon, S. K. Peck, D. Krause Jr., J. E. Gordon, L. R. Hunter, and S. K. Lamoreaux, Measurement of the electron electric dipole moment using GdIG, arXiv:physics/0509106 (2005)

[27] E. A. Hinds, Testing time reversal symmetry using molecules, Physica Scripta. T70: **34** (1997)

[28] J. Hisano, and Y. Shimizu, Hadronic electric dipole moments induced by strangeness and constraints on supersymmetric *CP* phases, Phys. Rev. D. **70**, 093001 (2004)

[29] J. J. Hudson, Measuring the electric dipole moment of the electron with YbF molecules, Ph.D. thesis, University of Sussex (2001)

[30] J. J. Hudson, B. E. Sauer, M. R. Tarbutt, and E. A. Hinds, Measurement of the electron electric dipole moment using YbF molecules, Phys. Rev. Lett. **89**, 023003 (2002)

[31] S. Jochim, M. Bartenstein, A. Altmeyer, G. Hendl, S. Riedl, C. Chin, J. H. Denschlag, R. Grimm, Bose-Einstein condensation of molecules, Science. **302**, 2101 (2003)

[32] L. A. Kaledin, J. C. Bloch, M. C. McCarthy, and R. W. Field, Analysis and deperturbation of the $A^2\Pi$ and $B^2\Sigma^+$ states of CaF, J. Mol. Spec. **197**, 289 (1999)

[33] D. Kawall, F. Bay, S. Bickman, Y. Jiang, and D. DeMille, Precision Zeeman-Stark spectroscopy of the metastable $a(1)[^3\Sigma^+]$ state of PbO, Phys. Rev. Lett. **92**, 133007 (2004)

[34] I. B. Khriplovich, and A. R. Zhitnitsky, What is the value of the neutron electric dipole moment in the Kobayashi-Maskawa model?, Phys. Lett. B. **109**, 490 (1982)

[35] I. B. Khriplovich, Parity nonconservation in atomic phenomena, Gordon and Breach Science Publications (1991)

[36] I. B. Khriplovich, and S. K. Lamoreaux, *CP* violation without strangeness, Spinger (1997)

[37] K. Kleinknecht, *CP* violation and K^0 decay, Annu. Rev. Nucl. Sci. **26**, 1 (1976)

[38] M. G. Kozlov, and V. F. Ezhov, Enhancement of the electric dipole moment of the electron in the YbF molecule, Phys. Rev. A. **49**, 4502 (1994)

[39] H. A. Kramers, Proc. Acad. Sci. Amsterdam. **40**, 814 (1937)

[40] S. K. Lamoreaux, Solid-state systems for the electron electric dipole moment and other fundamental measurements, Phys. Rev. A. **66**, 022109 (2002)

[41] L. Landau, On the conservation laws for weak interactions, Nucl. Phys. **3**, 127 (1957)

[42] T. D. Lee, and C. N. Yang, Question of parity conservation in weak interactions, Phys. Rev. **104**, 254 (1956)

[43] T. D. Lee, R. Oehme, and C. N. Yang, Remarks on possible noninvariance under time reversal and charge conjugation, Phys. Rev. **106**, 340 (1957)

[44] R. Loudon, The quantum theory of light, 3rd edition, Oxford Science Publications, Oxford University Press (2000)

[45] D. K. C. MacDonald, Noise and fluctuations: An introduction, Wiley (1962)

[46] S. E. Maxwell, N. Brahms, R. deCarvlho, D. R. Glenn, J. S. Helton, S. V. Nguyen, D. Patterson, J. Perticka, D. DeMille, and J. M. Doyle, High-flux beam source for cold, slow atoms or molecules, Phys. Rev. Lett. **95**, 173201 (2005)

[47] N. S. Mosyagin, M. G. Kozlov, and A. V. Titov, Electric dipole moment of the electron in the YbF molecule, J. Phys. B: At. Mol. Opt. Phys. **31**, L763 (1998)

[48] S. A. Murthy, D. Krause Jr., Z. L. Li, and L. R. Hunter, New limits on the electron electric dipole moment from Cesium, Phys. Rev. Lett. **63**, 965 (1989)

[49] D. F. Nelson, A. A. Schupp, R. W. Pidd, and H. R. Crane, Search for an electric dipole moment of the electron, Phys. Rev. Lett. **2**, 492 (1959)

[50] J. S. Nico, and W. M. Snow, Fundamental neutron physics, Annu. Rev. Nucl. Part. Sci **55**, 27 (2005)

[51] W. Pauli, Neils Bohr and the development of physics, Pergamon press, Oxford (1955)

[52] E. M. Purcell, N. F. Ramsey, On the possibility of electric dipole moments for elementary particles and nuclei, Phys. Rev. **78**, 807 (1950)

[53] N. F. Ramsey, Molecular Beams, Oxford University Press (1956)

[54] G. D. Redgrave, Spin spectroscopy of YbF using molecular beam interferometry, Ph.D. thesis, University of Sussex (1998)

[55] F. Reif, Fundimentals of statistical and thermal physics, McGraw - Hill book company (1965)

[56] B. C. Regan, E. D. Commins, C. J. Schmidt, and D. DeMille, New limit on the electron electric dipole moment, Phys. Rev. Lett. **88**, 071805 (2002)

[57] B. C. Regan, A search for violation of time-reversal symmetry in atomic thallium, Ph.D thesis, University of California at Berkeley (2002)

[58] R. G. Sachs, The physics of time reversal, The University of Chicago Press (1987)

[59] J. M. Sage, S. Sainis, T. Bergeman, and D. DeMille, Optical production of ultracold polar molecules, Phys. Rev. Lett. **94**, 203001 (2005)

[60] E. E. Salpeter, Some atomic effects of an electronic electric dipole moment, Phys. Rev. **112**, 1642 (1958)

[61] P. G. H. Sanders, The electric dipole moment of an atom, Phys. Letters. **14**, 194 (1965)

[62] P. G. H. Sanders, and E. Lipworth, Electric dipole moment of the Cesium atom. A new upper limit to the electric dipole moment of the free electron, Phys. Rev. Lett. **13**, 718 (1964)

[63] B. E. Sauer, Jun Wang, and E. A. Hinds, Anomalous spin-rotation coupling in the $X^2\Sigma^+$ state of YbF, Phys. Rev. Lett. **74**, 1554 (1995)

[64] B. E. Sauer, Jun Wang, and E. A. Hinds, Laser-rf double resonance spectroscopy of ^{174}YbF in the $X^2\Sigma^+$, J. Chem. Phys. **105**, 7412 (1996)

[65] B. E. Sauer, S. B. Cahn, M. G. Kozlov, G. D. Redgrave, and E. A. Hinds, Perturbed hyperfine doubling in the $A^2\Pi^{1/2}$ and [18.6]0.5 states of YbF, J. Chem. Phys. **110**, 8424 (1999)

[66] L. I. Schiff, Quantum mechanics, 3rd edition, McGraw-Hill international book company (1968)

[67] L. I. Schiff, Measurability of nuclear electric dipole moments, Phys. Rev. **132**, 2194 (1963)

[68] (Editor) G. Scoles, (Associated Editors) D. Bassi, U. Buck, Derek Lainé, Atomic and molecular beams methods, Volume 1, Oxford University Press (1988)

[69] B. W. Shore, The theory of coherent atomic excitation, Volume 1 and 2, Wiley (1990)

[70] T. J. Sumner, Progress towards a new experiment to search for the electric dipole moment of the neutron using ultra-cold neutrons, Ph.D. thesis, University of Sussex (1980)

[71] T. S. Stein, J. P. Carrico, E. Lipworth, and M. C. Weisskopf, Electric dipole moment of the Cesium atom. A new upper limit to the electric dipole moment of the free electron, Phys. Rev. Lett. **19**, 741 (1967)

[72] M. R. Tarbutt, J. J. Hudson, B. E. Sauer, E. A. Hinds, V. A. Ryzhov, V. L. Ryabov, and V. F. Ezhov, A jet beam source of cold YbF radicals, J. Phys. B: At. Mol. Opt. Phys. **35**, 5013 (2002)

[73] M. R. Tarbutt, H. L. Bethlem, J. J. Hudson, V. L. Ryabov, V. A. Ryzhov, B. E. Sauer, G. Meijer, and E. A. Hinds, Slowing heavy, ground-state molecules using an alternating gradient decelerator, Phys. Rev. Lett. **92**, 173002 (2004)

[74] A. V. Titov, N. S. Mosyagin, and V. F. Ezhov, P,T-odd spin-rotational Hamiltonian for YbF molecule, Phys. Rev. Lett. **77**, 5346 (1996)

[75] V. Vuletic, and S. Chu, Laser cooling of atoms, ions, or molecules by coherent scattering, Phys. Rev. Lett. **84**, 3787 (2000)

[76] J. Wang, Laser and radiofrequency spectroscopy of the YbF ground state, Ph.D. thesis, Yale University, 1996

[77] J. D. Weinstein, R. deCarvalho, T. Guillet, B. Friedrich, and J. M. Doyle, Magnetic trapping of calcium monohydride molecules at millikelvin temperatures, Nature. **385**, 148 (1998)

[78] M. C. Weisskopf, J. P. Carrico, H. Gould, E. Lipworth, and T. S. Stein, Electric dipole moment of the Cesium atom. A new upper limit to the electric dipole moment of the free electron, Phys. Rev. Lett. **21**, 1645 (1968)

[79] E. P. Wigner, Einige Folgerungen aus der Schrödingerschen Theorie für die Termstrukturen, Z. Phys. **43**, 624 (1927)
Reproduced in Chapter 26 of: E. P. Wigner, Group Theory, Academic Press (1956)

[80] G. K. Woodgate, Elementary atomic structure, 2nd edition, Oxford University Press (2002)

[81] L. Wolfenstein, Present status of *CP* violation, Annu. Rev. Nucl. Sci. **36**, 137 (1986)

[82] (editor) L. Wolfenstein, *CP* violation, Vol.5 Current physics – sources and comments (1989), Elsevier Science Publishers B. V

[83] L. Wolfenstein, Violation of time reversal invariance in K^0 decay, Phys. Rev. Lett. **83**, 91 (1999)

[84] C. S. Wu, R. W. Hayward, D. D. Hoppes, and R. P. Hudson, Experimental test of partiy conservation in beta decay, Phys. Rev. **105**, 1413 (1957)

Appendix A

In this appendix I consider another systematic effect that I have recently investigated, which occurs when there is an electric field dependent BShift.

If the electric field does not reverse symmetrically, and there is a Raman/rf detuning and a small BShift, there could be an additional BShift produced in the different states of the electric field. The reason for this is due to the fact that the Raman/rf transitions are driven in an applied magnetic field, which Zeeman splits the magnetic sublevels. If the Raman/rf transitions are tuned equidistant from the magnetic sublevels in one state of the electric field, but slightly closer to one of the magnetic sublevels in the other state, this would generate a BShift that depends on the electric field state. This would happen if the electric field did not reverse perfectly. See Figure (A.1).

To estimate the size of such a systematic error let us consider a simple model of the interferometer. In this model the first rf transition will be detuned towards the $m_F = +1$ statem, producing a population different between the m_F sublevels. The recombining rf transition will be modelled as an ideal transition. If we assume perfect pumping from the F=1 state, the molecules of interest will be in state $\mid 0,0\rangle$, labelled $\mid 0\rangle$ here. These molecules then interact with the first rf magnetic field producing the superposition,

$$\mid \psi\rangle = \frac{1}{(1+n^2)\sqrt{2}}\left[(1+n) \mid +\rangle + (1-n) \mid -\rangle\right]. \tag{A.1}$$

I have assumed that the population difference, after the transition, between the $\mid +\rangle = \mid 1,1\rangle$ and $\mid -\rangle = \mid 1,-1\rangle$ states is small. Here n represents the small difference in rf coupling efficiency due to a small difference of the rf intensity from the π pulse condition. This simplified equation can be calculated from a detailed model of the rf transitions. The simplified model is only for small values of the parameter n.

The next stage of the interferometer is to evolve a phase ϕ between the m_F

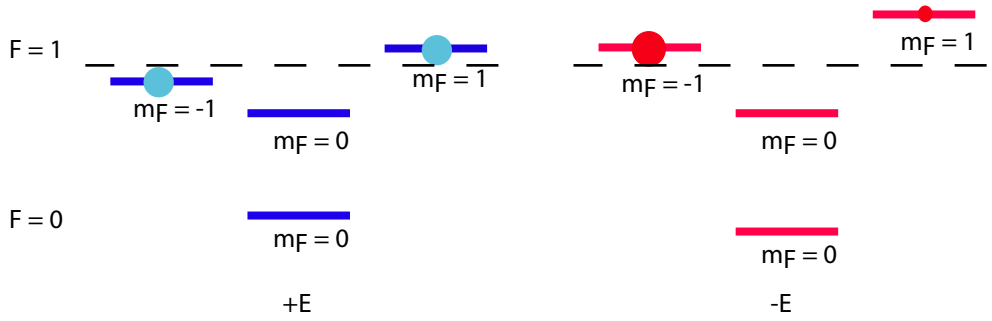

Figure A.1: In this ground state level diagram, the dashed line indicates the tuning of the rf or Raman transitions to the F=1 levels. Left is drawn the +E state and right the -E state where the tuning is closer to $m_F = -1$ level. This causes a systematic change of the EDM results. The size of the spot indicates the population of the level after the transition.

levels,

$$\mid \psi\rangle = \frac{1}{(1+n^2)\sqrt{2}}\left[(1+n)e^{i\phi} \mid +\rangle + (1-n)e^{-i\phi} \mid -\rangle\right]. \tag{A.2}$$

The wavefunction is then recombined back into the $\mid 0\rangle$ state with a second rf transition, which is assumed to be perfect. The state is now,

$$\mid \psi\rangle = C_0 \mid 0\rangle + C_+ \mid +\rangle + C_- \mid -\rangle \tag{A.3}$$

where the coefficients are,

$$C_0 = \frac{1}{1+n^2}(\cos\phi + in\sin\phi) \tag{A.4}$$

$$C_+ = \frac{1}{(1+n^2)\sqrt{2}}(n\cos\phi + i\sin\phi) \tag{A.5}$$

$$C_- = -\frac{1}{(1+n^2)\sqrt{2}}(n\cos\phi + i\sin\phi). \tag{A.6}$$

Now we take the modulus squared and find the population for each state. Then combine the $\mid +\rangle$ and $\mid -\rangle$ states to form the population measured in F=1. Thus the populations in F=0 and F=1 are,

$$P_0 = \frac{1}{(1+n^2)^2}(\cos^2\phi + n^2\sin^2\phi) \tag{A.7}$$

and,

$$P_1 = \frac{1}{(1+n^2)^2}(\sin^2\phi + n^2\cos^2\phi). \tag{A.8}$$

In Figure (A.2) the populations of the F=0 (red) and F=1 (green) states are shown with the n parameter slightly non-zero. We see that it has the effect of

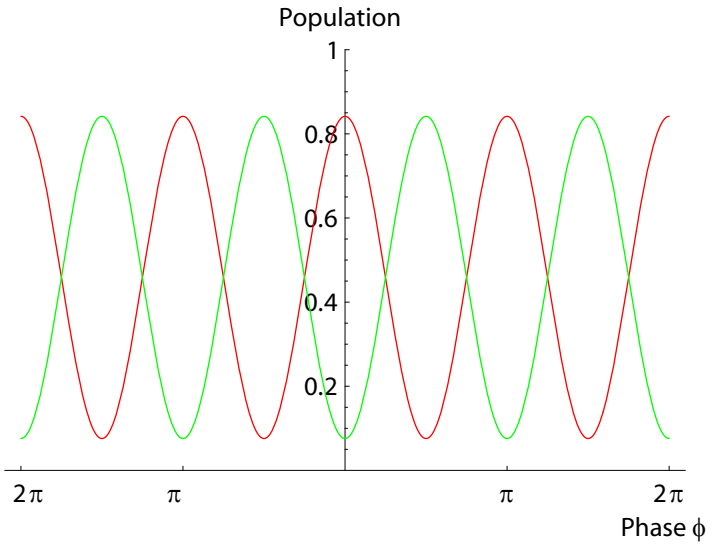

Figure A.2: Population of F=0 (red) and F=1 (green) states with the n parameter slightly non-zero. The x-axis is in terms of the phase shift π. This ignores the velocity distribution of the molecules for simplicity.

reducing the fringe contrast as one might expect if one of the rf transitions is not optimally setup. However, we do not find a false BShift that one might expect. However, if there already exists a BShift in the data then this BShift is altered when the detuning is varied. Figure (A.3) shows that if there is already a BShift, of around 0.1 nT in this case, then varying the detuning and changing the relative populations in the m_F states has the effect of changing the BShift calculated in the data analysis. As the n parameter is increased to one from zero the model becomes less valid because I have not taken into account a full treatment of the rf. However, it shows us that indeed this sort of detuning dependent on the electric field causes a problem. In the EDM channel there is a systematic effect produced either when there already exists an EDM in the data, or if the BShift is non-zero, which is the case in most circumstances. Figure (A.4) shows the systematic effect on the EDM analysis channel. From the Figure we see that the false EDM is entirely due to the BShift and a non-zero n, which could be produced by imperfect reversals of the electric field. Also as n increases so to does the amplitude of the false EDM, providing there is an initial BShift.

The question now presented is how well do we need to control the symmetry of the electric field reversal such that the effect is well below our sensitivity. To preform this calculation I drastically overestimate the initial BShift to be 10 nT and find the n value which generates an EDM of 10^{-28} $e.cm$. I then multiply this

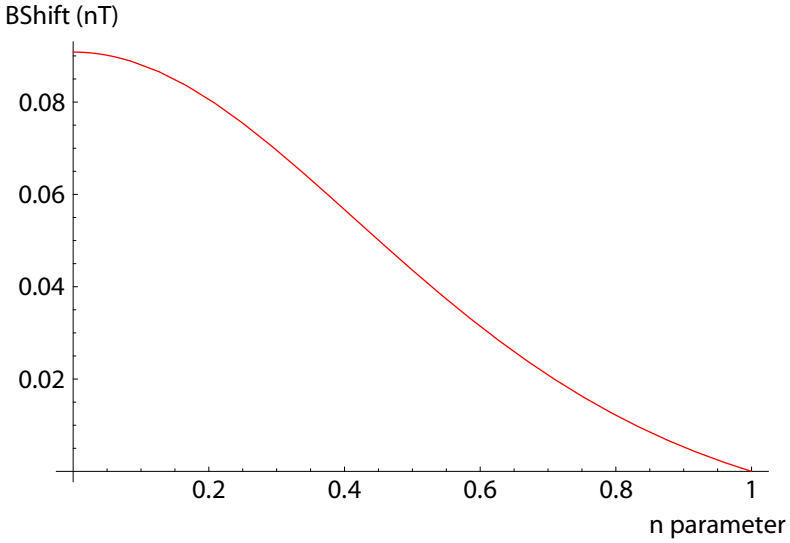

Figure A.3: Shows that if there is already a BShift, of around 0.1 nT in this case, then varying the detuning and changing the relative populations in the m_F states has the effect of changing the BShift calculated in the data analysis.

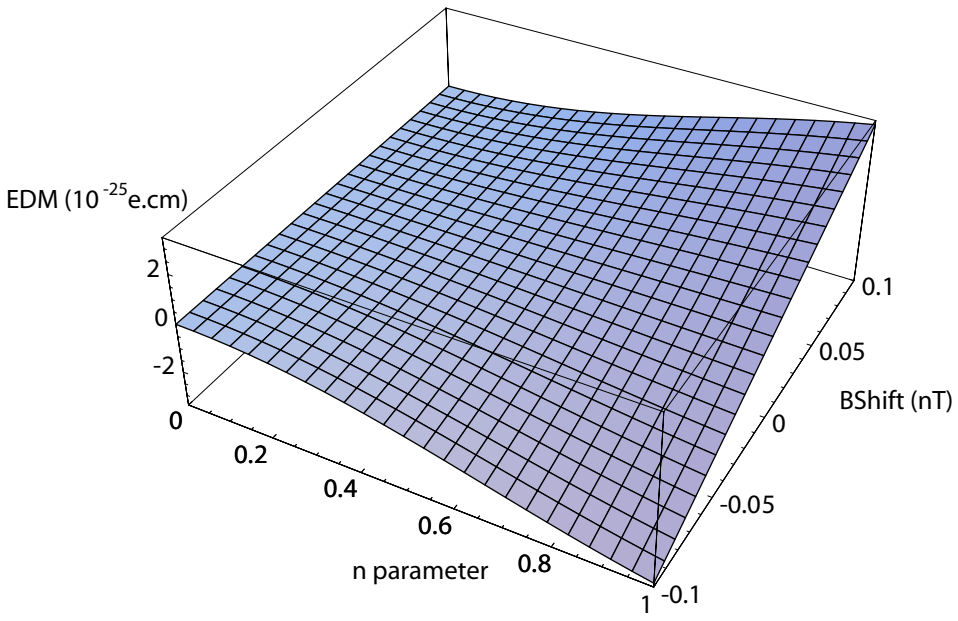

Figure A.4: Shows the effect of the systematic on the EDM analysis channel. The vertical axis showing the EDM is scaled to show $10^{-25} e.cm$, the other two axes show the n parameter, and the BShift in nT. In this example the initial EDM was taken to be exactly zero.

value of n by 2π turning it into a phase difference ϕ_n. It can be shown that this phase difference scales as,

$$\phi_n = \frac{BShift\ \delta}{2}. \tag{A.9}$$

Where the BShift is in units of phase angle, and δ is the rf detuning. Using this equation I relate the phase difference ϕ_n into an rf detuning δ in Hz. In normal operation we have the guard plates at approximately 4 kV/cm, which Stark shifts the hyperfine splitting to 171.25 MHz. Using this I can find the electric field which Stark shifts the splitting by the detuning δ, and using the plate spacing I find the difference in the voltage between the two states of the electric field. Our current sensitivity requires that the effect must be below 1×10^{-28} $e.cm$. The means we must control the voltage applied to the field plates to better than 2 Volts.

The guard plates normally reverse symmetrically to within 0.5 V. This asymmetry could produce a systematic effect of about a factor of 10 below the measured systematic result. However, this voltage difference is measured at the vacuum feedthrough which connect to the plates. We have not measured how well the electric field reverses between the plates. The plate surfaces, for example, could affect how well the field reverses. We are currently investigating ways in which we could measure the electric field using the molecules themselves. Also in the above calculation I have used a very simplistic model of the experiment, a more detailed calculation is necessary to be certain whether this is the systematic effect that is causing the problem.